Combined Transport, Magnetization and Neutron Scattering Study of Correlated Iridates and Iron Pnictide Superconductors

Author: Chetan Dhital

Boston College Electronic Thesis or Dissertation, 2014

Boston College

The Graduate School of Arts and Sciences

Department of Physics

COMBINED TRANSPORT, MAGNETIZATION AND NEUTRON SCATTERING STUDY OF CORRELATED IRIDATES AND IRON PNICTIDE SUPERCONDUCTORS

a dissertation

by

CHETAN DHITAL

submitted in partial fulfillment of the requirements

for the degree of

Doctor of Philosophy

May 2014

COMBINED TRANSPORT, MAGNETIZATION AND NEUTRON SCATTERING STUDY OF CORRELATED IRIDATES AND IRON PNICTIDE SUPERCONDUCTORS

Author: Chetan Dhital

Advisor: Stephen D. Wilson

Abstract

The work performed within this thesis is divided into two parts, each focusing primarily on the study of magnetic phase behavior using neutron scattering techniques. In first part, I present transport, magnetization, and neutron scattering studies of materials within the iridium oxide-based Ruddelsden-Popper series [$Sr_{n+1}Ir_nO_{3n+1}$] compounds $Sr_3Ir_2O_7$ (n=2) and Sr_2IrO_4 (n=1). This includes a comprehensive study of the doped bilayer system $Sr_3(Ir_{1-x}Ru_x)_2O_7$. In second part, I present my studies of the effect of uniaxial pressure on magnetic and structural phase behavior of the iron-based high temperature superconductor $Ba(Fe_{1-x}Co_x)_2As_2$.

Iridium-based 5d transition metal oxides host rather unusual electronic/magnetic ground states due to strong interplay between electronic correlation, lattice structure and spin-orbit effects. Out of the many oxides containing iridium, the Ruddelsden-Popper series [$Sr_{n+1}Ir_nO_{3n+1}$] oxides are some of the most interesting systems to study both from the point of view of physics as well as from potential applications. My work is focused on two members of this series $Sr_3Ir_2O_7$ (n=2) and Sr_2IrO_4 (n=1). In particular, our combined transport, magnetization and neutron scattering studies of $Sr_3Ir_2O_7$ (n=2) showed that this system exhibits a complex coupling between charge transport and magnetism. The spin magnetic moments form a G-type antiferromagnetic structure with moments oriented along the c-axis, with an ordered moment of 0.35 ± 0.06 $\mu B/Ir$. I also performed experiments doping holes in this bilayer $Sr_3(Ir_{1-x}Ru_x)_2O_7$ system in order to study the role of electronic correlation in these materials. Our results show that the ruthenium-doped holes remain localized within the $J_{eff}=1/2$ Mott insulating background of $Sr_3Ir_2O_7$, suggestive of 'Mott blocking' and the presence of strong electronic correlation in these materials. Antiferromagnetic order however survives deep into the metallic

regime with the same ordering q-vector, suggesting an intricate interplay between residual AF correlations in the $J_{eff}=1/2$ state and metallic nanoscale hole regions. Our results lead us to propose an electronic/magnetic phase diagram for $Sr_3(Ir_{1-x}Ru_x)_2O_7$ system showing how the system moves from $J_{eff}=1/2$ antiferromagnetic Mott insulator ($Sr_3Ir_2O_7$) to paramagnetic Fermi liquid metal ($Sr_3Ru_2O_7$). On the other hand, our neutron scattering measurements on Sr_2IrO_4 (n=1), a prototypical $J_{eff}=1/2$ Mott insulator, showed that the spins arranged antiferromagnetically in ab-plane with an ordered moment comparable to that of $Sr_3Ir_2O_7$.

The second part of my work is comprised of a neutron scattering-based study of the $Ba(Fe_{1-x}Co_x)_2As_2$ system, a bilayer family of iron-based high temperature superconductors. Undoped, this system exhibits either simultaneous or nearly simultaneous magnetic and structural phase transitions from a high temperature paramagnetic tetragonal phase to low temperature orthorhombic antiferromagnetic phase. With the gradual suppression of these two temperatures, the superconducting phase appears with the highest T_C obtained just beyond their complete suppression. It has been proposed that these coupled magnetostructural transitions are secondary manifestations which arise as a consequence of electronic nematic ordering that occurs at a temperature higher than either of them. My work is mainly focused on probing the spin behaviors coupling to this electronic nematic phase. I devised a small device to apply uniaxial pressure along an in-plane high symmetry axis and studied the magnetic and structural behavior in series of $Ba(Fe_{1-x}Co_x)_2As_2$ compounds via neutron scattering in presence of uniaxial pressure. There is an upward thermal shift in the onset of structural and magnetic transition temperature caused by this uniaxial pressure which is surprisingly insensitive to cobalt concentration in the absolute scale. Furthermore, on the first order side of the phase diagram (below the tricritical point), the structural and magnetic transitions are decoupled with magnetic transition following structural distortion. This study suggests the importance of both spin-lattice and orbital-lattice interactions in these families of compounds.

This dissertation is dedicated to my family.

Acknowledgements

First and foremost: I want to express my sincere thanks to my advisor Stephen D. Wilson for providing me the opportunity to work in his research group. He not only gave me a chance to work on many interesting projects but also taught me magnetic neutron scattering from the beginning. His strong interest and expertise in correlated magnetism and his curiosity toward condensed matter phenomena in general are the key inspiring factors for this work. I am one of the lucky few who can easily access his advisor to discuss any scientific or personal matter. I would also like to express my special thanks to Dr. Wilson for nominating me for the GMAG Outstanding Dissertation in Magnetism Award. The work presented herein was awarded this honor at the 2014 APS March Meeting.

I next thank to Professor Cyril Opeil and my graduate committee members Professor Vidya Madhavan, Professor Michael Graf and Professor Ziqiang Wang for their efforts in our collaborations, as well as constant support and valuable suggestions throughout this work. I also thank their group members for their cooperation.

I cannot continue without thanking Jeffry Lynn (NIST), Clarina Dela Cruz (ORNL), Zahra Yamani (CNBC), Wei Tian (ORNL), Masa Matsuda (ORNL) and many others for their support in performing neutron scattering experiments. I would like to especially thank Zahra who also taught me much of the instrumentation techniques for neutron scattering.

I would also like to extend the acknowledgements to my colleagues Sovit Khadka, Tom Hogan, Zhensong Ren, Xiang Chen, Rebacca Dally, Mani Pokharel, Binod Rizal and the whole physics department for their direct and indirect support throughout this work.

I must finally thank my first teachers and caregivers, my parents Homnath and Bedmaya, for their endless unconditional support from the day I was born. I also want to express my thanks to my wonderful loving wife Suchita for her constant support and inspiration, who always encouraged me to focus on research, despite this keeping me away from household business. I also thank my kids Hridum and Ridhima whose innocent smiles and activities always refreshed me as well as encouraged me to become a responsible father. Finally I like to thank my whole family and the Nepali community in Boston for their help and inspiration.

Table of Contents

Chapter 1: Introduction

I want to start with high school definition of condensed matter physics that it is a branch of physics which deals with the properties of matter when the matter is in some sort of "condensed" form like liquid or solid. After my undergraduate and master degree from Nepal, where I took most of the physics courses, I came to realize that physics is not just the collection of assumptions, hypothetical problems and their solutions in terms of unknown constants, particularly within condensed matter physics. I also noticed that many great scientists have spent their whole life in this field and most of the modern technologies we used today are the outcome of their endless efforts in condensed matter research.

The facts mentioned above give the importance of the condensed matter research. Now the real question to ask is: what is so special about being 'condensed' and why this condensed phase hosts so many different phenomena?. There is a very short answer by P.W Anderson: "more is different". When a large number of particles having either charge or mass or spins or all of them together "condense" to form solids or liquids they may lose their individual identity due to various types of classical and quantum interactions between them. Thus, a condensed phase of matter is in fact an assembly of a large number of microscopic constituents like charges, masses, spins, interactions and excitations (phonons, magnons,polarons, holons, polaritons, plasmons, solitons etc). The various interactions between these microscopic constituents result in the emergent new macroscopic quantum states like superconductivity, magnetism, metals, insulators, topological insulators, spin liquids, spin ices etc. In some cases two phenomena may look different at first sight but may still be governed by the same fundamental interactions. Condensed matter physics takes the responsibility of connecting microscopic and macroscopic behaviors and tries to organize/classify phenomena according to the mechanisms behind them.

This thesis deals with macroscopic properties of two classes of materials within current condensed matter research: correlated iridates and iron pnictides. There are some broad similarities between these two seemingly different families of compounds where they lay close to the intermediate correlation regime with iridates on the strong correlation side and iron pnictides on the weak correlation side.

Out of many different types of oxides of iridium, this thesis deals with the Ruddlesden-Popper series oxides ($Sr_{n+1}Ir_nO_{3n+1}$) where I have used 3 main probes: namely electrical transport, bulk magnetization and neutron scattering to explore the electronic/magnetic ground states and we have also shown that the electronic correlations are important along with the strong spin-orbit interactions.

Regarding the iron-based superconductors (iron pnictides), this work is focused on the study of structural and spin behavior of the parent and underdoped system $Ba(Fe_{1-x}Co_x)_2As_2$.In this study, I have shown that even a relatively small symmetry breaking field, when applied in the high temperature, electronically anisotropic phase,the so-called “nematic phase”, gives a dramatic response in the lattice and spin behavior of the system. The evolution of the spin and lattice susceptibility to strain with doping in presence of symmetry breaking uniaxial pressure hints toward the importance of combined effect of spin-lattice and orbital-lattice interactions in these systems.

Outline of this Work

The reminder of this work is divided into following chapters

Chapter 2: Introduction to Iridates and Neutron Scattering

This chapter provides a brief introduction to iridates, various terminologies like crystal field splitting, spin orbit coupling, metal insulator transitions, magnetism and neutron scattering along with key mathematical relations.

Chapter 3: Experimental Methods

This chapter provides a brief overview of the different experimental methods used throughout the thesis including crystal growth, X-ray diffraction, energy dispersive analysis, magnetization measurement, resistivity measurement, thermo-gravimetric analysis and neutron scattering.

Chapter 5: Structural/magnetic Behavior of Sr_2IrO_4

This chapter provides the result of neutron scattering study on single layer parent compound Sr_2IrO_4 which reveals the spin structure, ordered moment and the lattice distortions.

Chapter 5: Electronic/spin Behavior of $Sr_3Ir_2O_7$

This chapter provides the results of combined magnetotransport and neutron scattering study on bilayer parent compound $Sr_3Ir_2O_7$ revealing its electronic/magnetic ground state along with previously unreported structural distortions.

Chapter 6: Electronic/magnetic Phase Diagram of $Sr_3(Ir_{1-x}Ru_x)_2O_7$

This chapter is about the comprehensive study of doped bilayer system $Sr_3(Ir_{1-x}Ru_x)_2O_7$, which establishes an electronic/magnetic phase diagram with coexisting multiple phases. This study also stresses the role of electronic correlations in this bilayer system.

Chapter 7: Effect of Uniaxial Pressure on Magnetic and Structural Phase Behavior of $Ba(Fe_{1-x}Co_x)_2As_2$.

This chapter gives a very brief introduction to iron-based superconductors and discusses the effect of uniaxial pressure on the structural and magnetic phase behavior of concentrations in the underdoped regime.

Chapter 8: Conclusions and Future Works

In this chapter I summarize the results on both systems and suggest some future works that should be pursued.

Appendix

List of Publications

Chapter 2: Introduction to Iridates and Neutron Scattering

2.1 Introduction

Recently, the 5d transition metal ‘iridium’ perovskites (Ir) (Z=77) and, more specifically, Ir^{4+} ions in a cubic crystal field are subjects of considerable interest. They not only have the usual technological advantage of being oxides with high chemical and thermal stability, they are also proposed to host to many exotic quantum phases like topological Mott insulator [1], Weyl semimetal [2], quantum spin liquid [3], spin ice [4], Kitaev-Heisenberg spin liquid [5], anomalous Hall states [6], $J_{eff}=1/2$ Mott insulators [7--9] and potentially high temperature superconductivity [10] etc. These quantum phases are the result of strong interplay between spin-orbit interaction, electronic correlations, and the lattice structure. This interplay alters or rearranges the conventional energy hierarchy thus resulting in rather unusual quantum states. Out of many families of oxides of iridium, this thesis is focused on members of Ruddelsden-Popper (RP) series [$Sr_{n+1}Ir_nO_{3n+1}$], especially (Sr_2IrO_4) (n=1) and ($Sr_3Ir_2O_7$) (n=2) and the doped compound $Sr_3(Ir_{1-x}Ru_x)_2O_7$. These were studied using neutron scattering, transport and magnetization techniques. Both of these parent compounds are suggested to host $J_{eff}=1/2$ Mott insulating states where the crystal field (CF) splitting (2 eV-5 eV) and spin-orbit (SO) coupling (~1eV) cooperate to distribute all the valence electrons (5 electrons/Ir^{4+} ion) to all fully occupied $J_{eff}=3/2$ and half-filled $J_{eff}=1/2$ band [9]. Thus the effective bandwidth of the material is determined by the bandwidth of the $J_{eff}=1/2$ band which is small and hence relatively weak electronic correlation (U~0.5eV) can open up a charge gap, resulting in Mott insulating state [7,9].

Some of the outstanding issues in the field are: (1) the crystal structures of both $Sr_3Ir_2O_7$ and Sr_2IrO_4 were not fully understood; (2) although J_{eff}=1/2 Mott-insulating behavior was proposed, there remains alternative theories regarding the microscopic origin of the insulating phase. (3) The exact information about the magnitude and direction of the ordered spin moment was still lacking, especially with no neutron studies on the single crystals of these compounds (4) There was ongoing debate about the nature of the insulating state: whether they are spin-orbit driven J_{eff}=1/2 Mott-insulator or they are magnetic ordering driven Slater insulators [11]. With these situations in hand we moved forward, successfully grew single crystals and performed neutron scattering experiments. By now, along with our studies, there are numerous other studies involving transport, magnetization, crystal structure, electronic structure and spin structure of Sr_2IrO_4 [7,12--18] and $Sr_3Ir_2O_7$ [19--26]. The results, significance and uniqueness of our work will be discussed in the following chapters 4, 5 and 6. In the following sections, I will define some of the relevant physics along with mathematical formalism of phenomena that are relevant to this work. A curious reader can refer to the references given in each section.

2.2 Spin-Orbit Interaction

Spin-Orbit coupling is a relativistic effect in solids with heavier elements that prevents the orbital angular momentum from being quenched. Each electron in a solid has 3 degrees of freedom: Spin, Orbital and Charge. The interplay between these determines the properties of a solid. The spin and orbital motion have angular momentum associated with them, which produce magnetic moments. In the electrons' rest frame, it seems as if the nucleus is orbiting around it producing relativistic magnetic field which is given by [27].

$$\mathbf{B} = \frac{\boldsymbol{\varepsilon} \times \mathbf{v}}{c^2} \qquad (2.2.1)$$

Where $\boldsymbol{\varepsilon}$ is the electric field at the electron due to nucleus and $V(\boldsymbol{r})$ is the corresponding potential energy and is given by expression [27]

$$\boldsymbol{\varepsilon} = -\nabla V\left(\mathbf{r}\right) = -\frac{\mathbf{r}dV(\mathbf{r})}{rdr} \qquad (2.\ 2.2)$$

The magnetic field (***B***) interacts with the spin angular momentum of the electron giving spin orbit Hamiltonian H_{SO} given by [27]

$$H_{SO} = -\frac{(\mathbf{m}\times\mathbf{B})}{2} = -\frac{(e\hbar}{\quad} \quad \underset{2m_e c^2 r}{} \quad \bullet \qquad (2.2.3)$$

where $\boldsymbol{L}$ is the orbital angular momentum and the magnetic moment $\boldsymbol{m}$ associated with spin $\boldsymbol{S}$ is given by $\boldsymbol{m=(ge\hbar/2m_e)S}$ with g as Lande's g factor. For the Coulomb field in a hydrogen-like atom one can write the derivative term as [27]

$$\frac{dV(r)}{rdr} = \frac{Ze}{4\pi \in_o r^3} \qquad (2.2.4)$$

Using

$$\frac{1}{r^3} = \frac{Z^3}{a_0^3\, n^3 l(l+\frac{1}{2})(l+1)} \qquad (2.2.5)$$

The spin orbit splitting energy can be written as [27]

$$E_{SO} = \frac{Z^4 e^2 \hbar\ \boldsymbol{S}\ \boldsymbol{L}}{4\pi\varepsilon_0 a_0^3 n^3 l(l+\frac{1}{2})(l+1)} \qquad (2.2.6)$$

This expression shows that the spin-orbit coupling varies as the fourth power of atomic number *Z*. Iridium (5d elements in general) have relatively large atomic number (Z=77) which is the reason why oxides containing iridium are an ideal candidate for exploring spin-orbit driven physics. The spin-orbit splitting energy in these oxides (Sr_2IrO_4 and $Sr_3Ir_2O_7$) is of the order of (0.1eV – 1eV). This energy is comparable to coulomb energy of about (0.4eV – 2eV).

2.3 Crystal Field Splitting, Energy Hierarchy and Ground State Wave function

For a free transition metal ion (M^+), the outermost d orbitals are fivefold degenerate. However, in a real solid this positive metal ion is surrounded by negative ions (O^{2-} in metal oxides) which occupy fixed positions relative to metal ion. This surrounding environment of negative ions creates an inhomogeneous electric field at the position of positive metal ion. This electric field is called the *crystal field* [28] which partially lifts the degeneracy of the d orbitals. This is called *crystal field splitting*. The energy splitting depends upon how the negative ions are located relative to positive ions. If the negative ions are located near the point of maximum charge density of the positive ion, the two electron clouds experience repulsion resulting in the increase in energy relative to other ions.

In Ruddelsden-Popper series iridates [$Sr_{n+1}Ir_nO_{3n+1}$], the Ir^{4+} ion is at the center of octahedral formed by 6 surrounding oxygen ions (O^{2-}). This arrangement separates the 5 degenerate d levels into two groups t_{2g} (d_{xy}, d_{yz},d_{xz}) and e_g ($d_{x^2-y^2}$,d_{z^2}) with $E(e_g) > E(t_{2g})$ as shown in Figure 2.3.1.

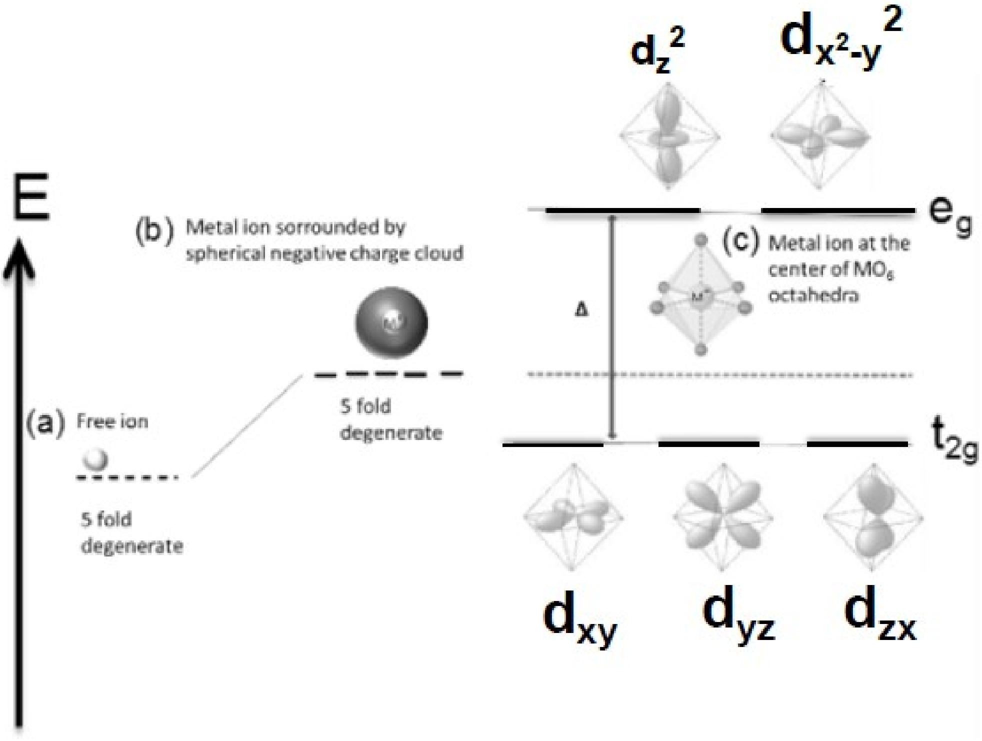

Figure 2.3.1 Energy level scheme (a) for free metal ion (b) ion surrounded by spherical negative cloud of electron (c) ion at the center of oxygen octahedral. The fivefold degeneracy is partially lifted and is divided into two groups t_{2g} (3 fold degenerate) and e_g (two fold degenerate) (M^+=Ir^{4+}). Figure reproduced from [53]

Since these iridates are magnetic insulators despite the presence of extended 5d orbitals, a new quantum state J_{eff}=1/2, rather than the S=1/2 state (as in cuprates), is suggested, caused mainly by strong spin orbit coupling [9]. In this scenario, the spin orbit coupling further splits the t_{2g} level into J_{eff}=3/2 and J_{eff}=1/2 levels with E (J_{eff}=1/2) > E (J_{eff}=3/2). Out of 5 valence electrons in Ir^{4+} ion, the four electrons occupy J_{eff}=3/2 orbitals whereas the J_{eff}=1/2 level is occupied with one electron and one hole. The band width of the half-filled J_{eff}=1/2 band is narrow. Thus even moderate correlation strength (U) can open up a Mott gap. The energy level scheme in presence of crystal field splitting, spin orbit coupling and the electronic correlation is summarized in Figure 2.3.2

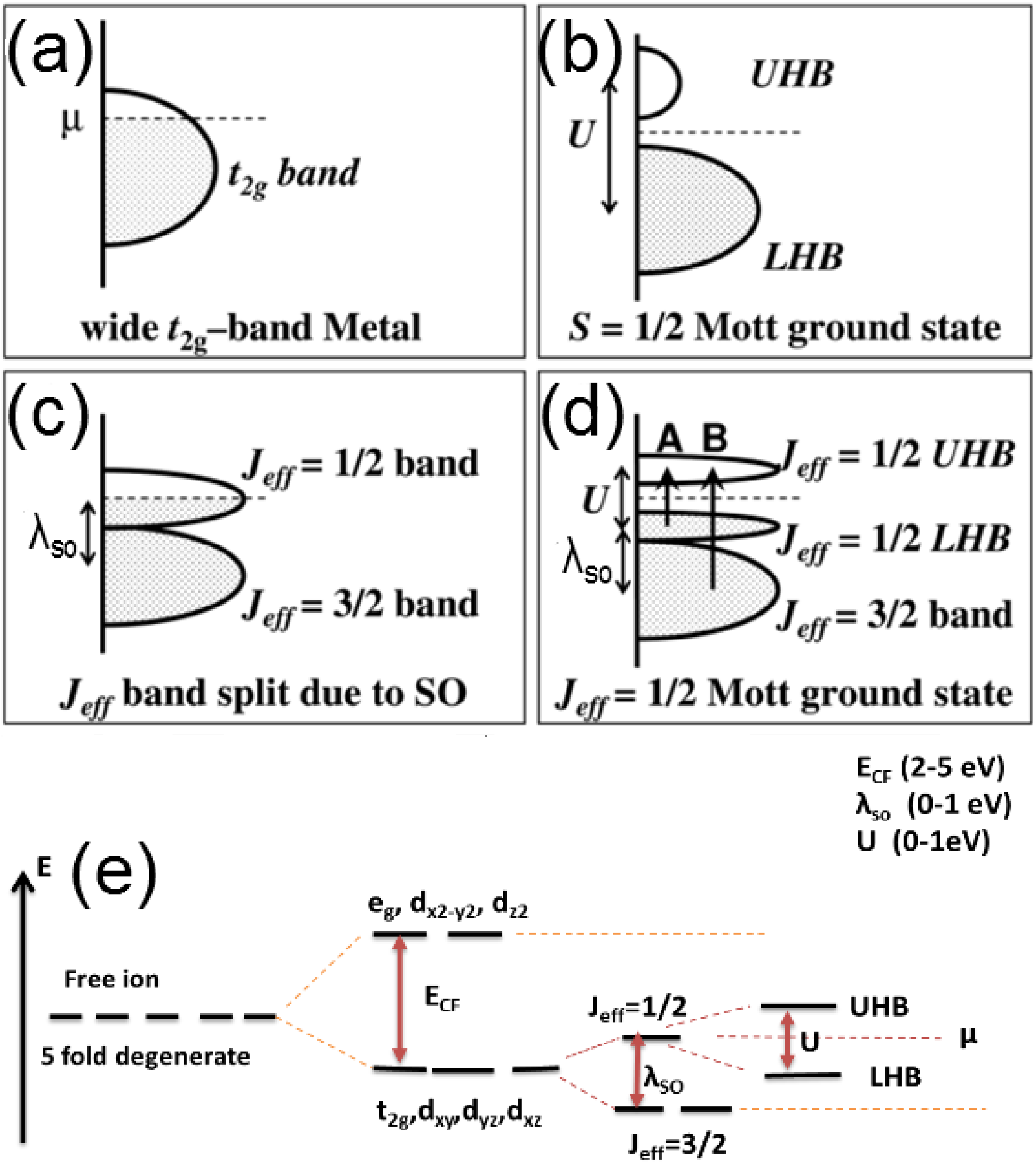

Figure 2.3.2 Schematic energy diagrams for the $5d^5$ (t_{2g}) configuration (a) without SO and U, (b) with an unrealistically large U but no SO, (c) with SO but no U, and (d) with SO and Possible optical transitions A and B are indicated by arrows.(e) 5d level splitting by the crystal field and SO coupling [9].

Due to presence of spin orbit coupling, the wave function of the J_{eff}=1/2 state is given by complex admixture of all 3 degenerate t_{2g} states where both spin and orbital components are mixed. The wave function of the Kramer's doublet can be expressed as [7]

$\left|J_{eff}=\frac{1}{2},+\right\rangle = \frac{1}{\sqrt{3}}(|yz,+\rangle - |xy,-\rangle - i|xz,+\rangle)$ and

$\left|J_{eff}=\frac{1}{2},-\right\rangle = \frac{1}{\sqrt{3}}(|xy,+\rangle + |yz,-\rangle + i|xz,-\rangle)$. These expressions are valid strictly when there is perfect octahedral crystal field splitting or in other words when the Ir^{4+} ion is in perfect cubic crystal field environment with the wave function as shown in Figure 2.3.3.

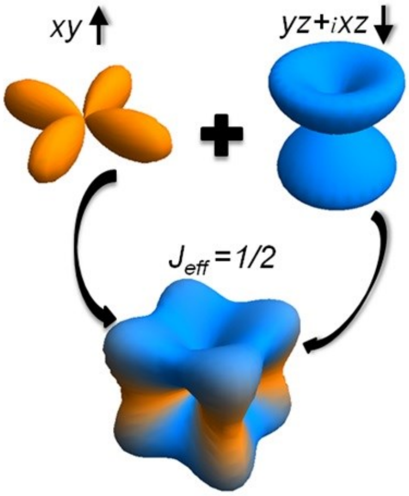

Figure 2.3.3 Shape of ideal cubic $J_{eff}=1/2$ wave function which contains equal mixture from all 3 t_{2g} states [8].

It has also been suggested that any deviation from this cubic crystal environment, for example by a tetragonal distortion, alters the system from true $J_{eff}=1/2$ state and may allow the hybridization between $J_{eff}=3/2$ and $J_{eff}=1/2$ states, thus providing a larger effective bandwidth. In this picture Sr_2IrO_4 (n=1) system is supposed to be close to the ideal case than $Sr_3Ir_2O_7$ (n=2). One metric for determining the validity of $J_{eff}=1/2$ picture is the estimation of intensity ratio of L_3 and L_2 edges, which looks similar for both Sr_2IrO_4 and $Sr_3Ir_2O_7$, validating the $J_{eff}=1/2$ picture for both these compounds. However, this method of assigning $J_{eff}=1/2$ state is put into question by other studies where they can produce same type of ratio even without considering the $J_{eff}=1/2$ states provided the moments are in the basal plane [29].

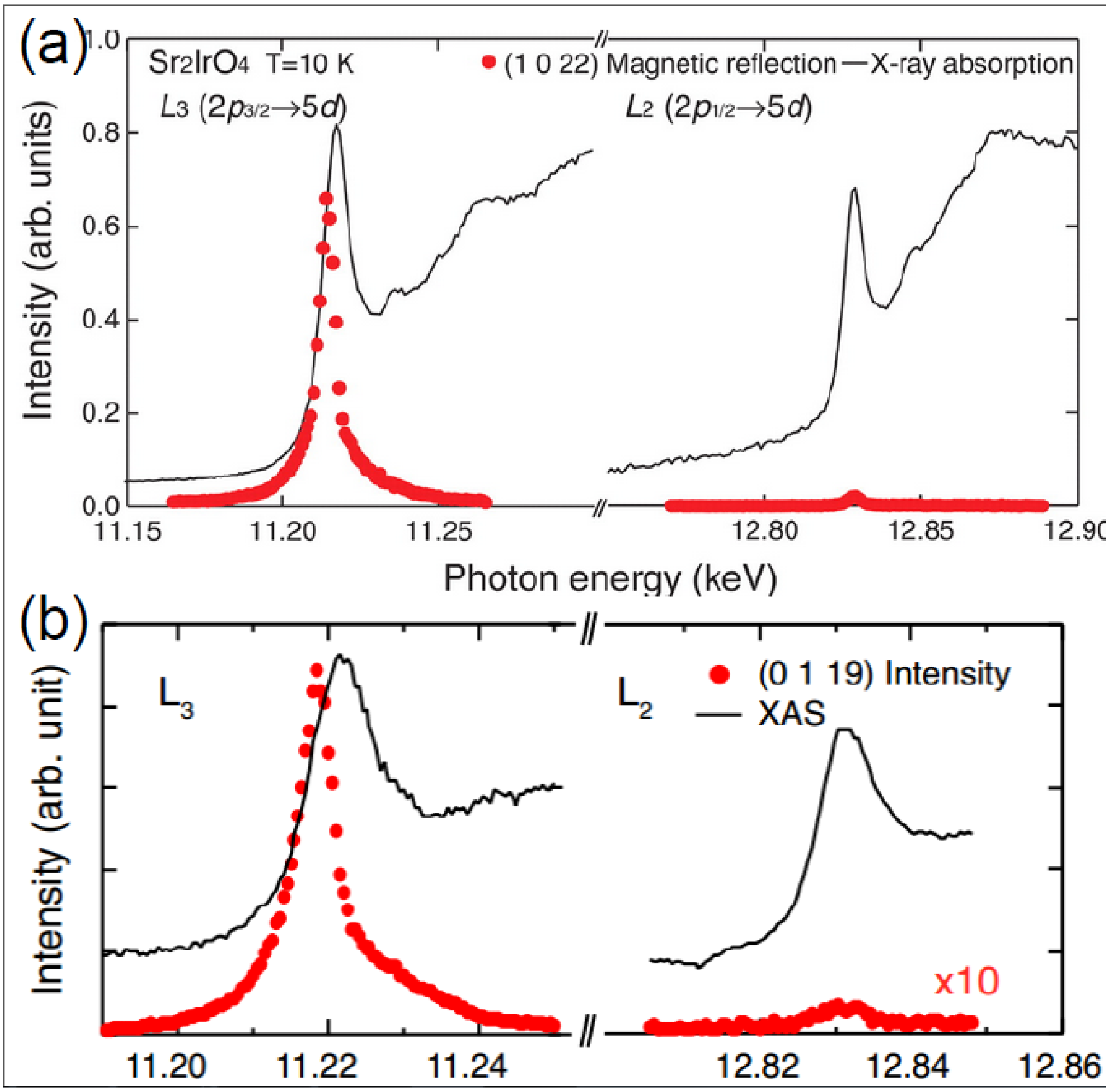

Figure 2.3.4 Intensity ratio of L_3 and L_2 edges for (a) Sr_2IrO_4 [7]and (b) $Sr_3Ir_2O_7$ [21]

2.4 Ruddelsden-Popper Series

The Ruddelsden-Popper series [30,31] is a particular family of crystalline structures represented by general chemical formula $A_{n+1}B_nO_{3n+1}$ or $(AO)(ABO_3)n$, where A is alkaline earth metal or rare earth metal cation, B is usually a transition metal cation, O is oxygen or some other anion and n is the number of layers of octahedral in the perovskite-like stakes [31]. In other words, they consist of n consecutive perovskite blocks $(ABO_3)_n$, which are separated by rock salt layers (AO) where the perovskite structure is the n = end member as shown in Figure. 2.3.5.

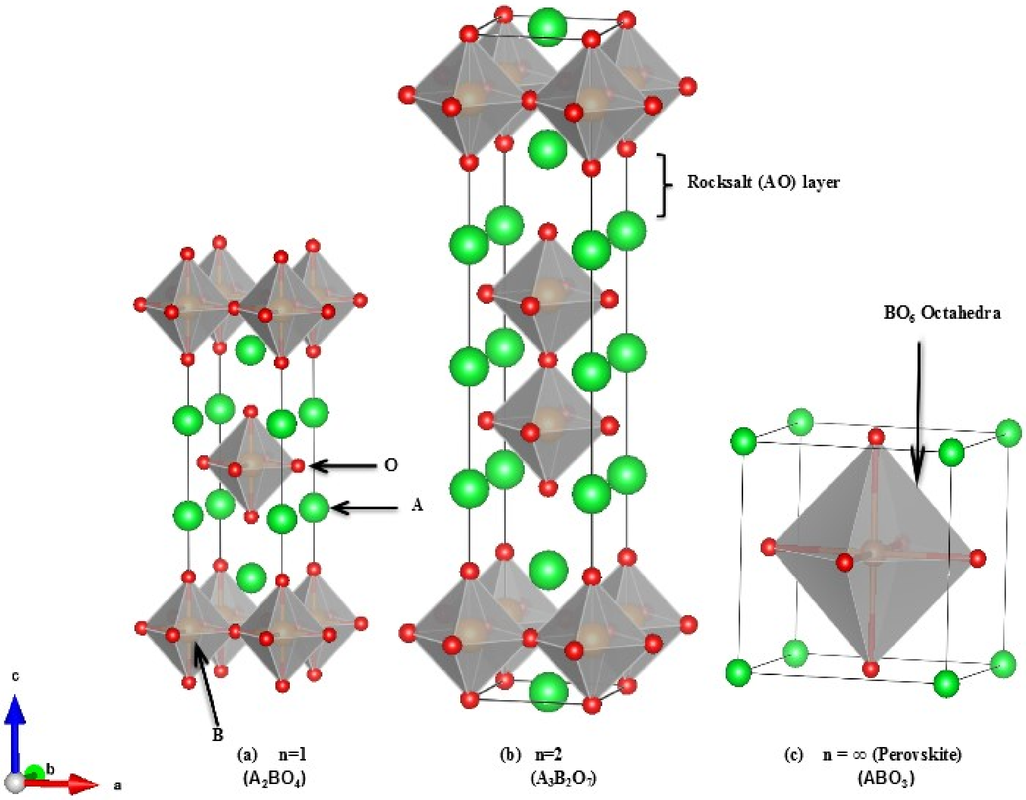

(a) n=1 (A_2BO_4)

(b) n=2 ($A_3B_2O_7$)

(c) n = ∞ (Perovskite) (ABO_3)

Figure 2.3.5 Ruddelsden-Popper series crystal structure for (a) A_2BO_4 (n=1) (b) $A_3B_2O_7$ (n=2) and (c) ABO_3 (n=∞). Figure reproduced using VESTA 3 software [32].

If the octahedra are perfect (meaning Ir^{4+} is in perfect cubic environment), then n=1 and n=2 compounds tend to have tetragonal symmetry but when there is a rotation or tilting of octahedral away from the perfect condition, the symmetry of the crystal is reduced. We observe this in our samples of Sr_2IrO_4 and $Sr_3(Ir_{1-x}Ru_x)\ _2O_7$. In Sr_2IrO_4 the neighboring octahedra rotate about the c-axis by about 11° and this staggered rotation propagates along both in-plane and c axes [14]. This increases the unit cell dimension as well as reduces the symmetry of the crystal (breaks inversion symmetry). The unit cell dimension becomes $(\sqrt{2}a\times\sqrt{2}a\times 2c)$ with space group

I41/acd (no.142) instead of *$(a\times a\times c)$* with space group I4/mmm (no.139) where *a* is *a*-axis lattice parameter of undistorted unit cell and *c* is the *c*-axis lattice parameter of undistorted unit cell. For $Sr_3Ir_2O_7$, a similar rotation of octahedral about *c* axis (~11^o) increases the unit cell volume from *$(a\times a\times c)$* (space group *I4/mmm* (139)) to *$(\surd 2a\times\surd 2a\times c)$* (space group *Bbcb* (68)) [20] (since the rotations are not correlated the *c* axis does not change). The new structures for Sr_2IrO_4 and $Sr_3Ir_2O_7$ are shown in Figure 2.3.6.

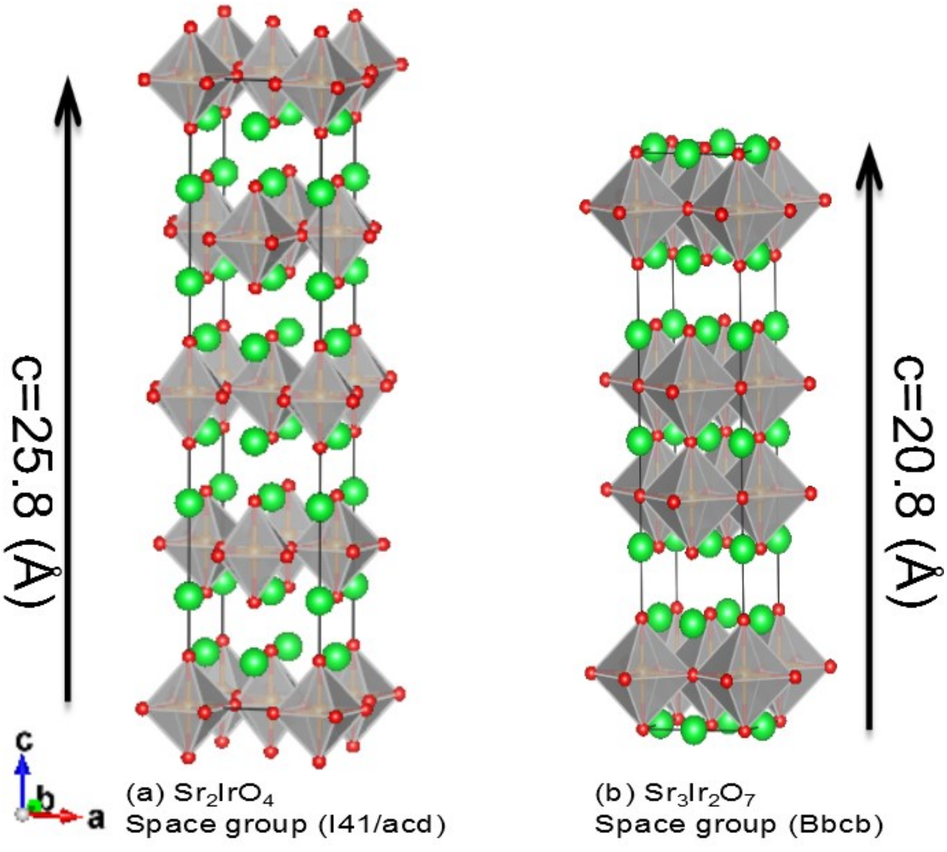

Figure 2.3.6 (a) reduced tetragonal structure of Sr_2IrO_4 (space group I41/acd, 142) [14] and (b) orthorhombic structure (Space group Bbcb, 68) of $Sr_3Ir_2O_7$ [20].

2.5 Metal Insulator Transition and Resistivity

A true distinction between metal and insulator can be made only at T=0 K where an insulator will have vanishingly small charge conductivity and is characterized by a gap in the charge excitation spectrum. At finite temperature one can only speak of how good or how bad an insulator or metal is. The electron transport in a solid can be affected by electron-ion interaction, electron-electron interaction and external fields [33]. Generally the electron-ion interaction leads to band insulators [28], Peierls insulators [33] (due to interaction with static lattice deformation) or an Anderson insulator [34] (due to interactions with disorder or lattice imperfections). The insulators resulting from electron-electron interactions can be classified as Slater insulators [35] (magnetic ordering primary, electron-electron interaction secondary), Mott-Hubbard [36] insulators (electron-electron interaction, no magnetic ordering) and Mott-Heisenberg [37] insulators (electron-electron interaction followed by magnetic ordering). The Slater insulating states can be realized in an antiferromagnetically ordered lattice which can be taken as combination of two interpenetrating half-filled sub lattices (one electron per site). In such arrangement, the nearest neighbors always have opposite spin. These opposite spins occupy two different sublattices to minimize their interaction. Hence a spin density wave is formed with some commensurate wave vector Q where the density of up spin or down spin varies periodically. This is in fact the result of tendency of electrons to avoid each other which generally results in increase in potential energy at the expense of the kinetic energy. Due to opposite spins on neighboring sublattices, the unit cell in real space is doubled- meaning the reciprocal space unit cell is halved. At the boundary of this new magnetic Brillouin zone, the bands split and hence the energy of the occupied level is lowered. At half band filling the band splitting produces a charge excitation gap [33]. The Slater and Mott-Heisenberg insulators differ from each other because in a Slater insulator the occurrence of an insulating state is simultaneous to formation of long-range antiferromagnetic order, though this is not the case in Mott-Heisenberg insulator. Again, in a real solid all types of interactions are present; it is only the strength of interaction that varies. Whatever the origin of the transition and the nature of insulating/metallic state is, the metal insulator transitions can be broadly classified into two types: quantum phase transition and thermodynamic phase transition. The quantum phase transition results from the continious competition between electrons' kinetic and potential energy whereas the thermodynamic phase transition results from the competition between internal energy and entropy [33]. A good discussion of metal-insulator transition can also be found in the following review paper by Imada et al [38].

The metal insulator transition can also be caused by *percolation* [39].This type of transition mostly occurs in a doped system, where for lower concentration of dopants, they form independent metallic clusters. However, after certain critical concentration, these clusters start to connect throughout the whole sample providing an 'electrical short' for the conduction. The value of critical concentration x_c depends upon the dimensionality of the system. The conductivity variation in percolation transition can be expressed as [40]:

$$\sigma(T=0)=\sigma_o\left(\frac{x'}{x'_c}-1\right)^t \qquad (2.5.1)$$

Where x' is the metallic volume fraction, x'_c is the percolation threshold and t is a critical exponent. Both x'_c and t depend upon dimensionality. The system, $Sr_3(Ir_{1-x}Ru_x)_2O_7$ used in our study also shows a near-percolative (as it does not strictly obey equation 2.5.1) metal insulator transition. The ruthenium holes form independent metallic clusters at low Ru concentration however after critical concentration $x_c=0.35$, the system becomes truly metallic which is close to 2D percolation threshold $x_c=0.41$. I will discuss in further detail about this metal-insulator transition in chapter 6.

Now I turn to the temperature dependence of resistivity in different systems. From the temperature dependence of resistivity, one can obtain crucial information such as: gap size (activated gap in insulating/semiconducting system), nature of metallic state (Fermi/non-Fermi liquid), conduction mechanism in insulating state and the effective dimensionality of the system. For example: in a metallic system the temperature dependence of the electronic part of resistivity can be expressed as [41]

$$\rho(T)=\rho_o+AT^n \qquad (2.5.2)$$

Where ρ_o is the residual resistivity, A is a temperature independent coefficient. For a Fermi liquid metal, the exponent n is nearly 2, however in a highly correlated metal n is less than 2. The system with n ~1 is supposed to have quantum critical behavior with a quantum phase transition occurring at T=0 K. In an insulating (semiconducting) system with an activated gap, the resistivity can be expressed as [28]

$$\rho(T)=\rho(T=0)\exp(\frac{E_g}{K_BT}) \qquad (2.5.3)$$

Where E_g is the activated gap.

Similarly, in an insulator with variable range hoping mechanism the resistivity is expressed as [42]

$$\rho(T)=\rho(T=0)\exp\left(\frac{T_0}{T}\right)^{\frac{1}{d+1}} \qquad (2.5.4)$$

Where T_0 *is* some characteristic temperature of system and d is the effective dimensionality for the charge conduction.

2.6 Magnetism

The fundamental quantity in magnetism is the magnetic moment which is defined in terms of an infinitesimal current loop and, given by [27]

$$\boldsymbol{\mu} = \int_s I ds \mathbf{n} \tag{2.6.1}$$

Where **n** is the unit vector normal to the closed loop where the current I is flowing. dS is the area element and integration is taken over the area of the loop. The magnetic moment of an orbiting electron is called the Bohr magneton and is given by [27]

$$\mu_B = \frac{e\hbar}{2m_e} \tag{2.6.2}$$

Instead of just orbital motion, the electron also has the spin about its own axis. This motion also has an associated angular momentum and hence associated magnetic moment. In a real atom, the orbital angular momentum of the electron depends upon the electronic state occupied by the electron. The total magnetic moment of an atom or ion comes from vector sum of orbital and spin magnetic moment of all the constituent electrons. The summation scheme (L-S or J-J) depends upon the spin-orbit coupling. An atom without unpaired electrons cannot have a magnetic moment because the vector sum cancels out completely but an atom with unpaired electrons possess magnetic moment because the result of the summation is non-zero. A real solid contains a large number of atoms or ions each having either zero or some net magnetic moment in the absence of an external magnetic field. If there is no interaction between atomic moments then they can be classified into two groups [28]: diamagnetic and paramagnetic. When an assembly of atoms each with zero magnetic moment is placed in an external magnetic field, each individual atom acquire a magnetic moment opposite to the direction of magnetic field, a consequence of Lenz's law. This induced magnetic moment persists as long as the field is applied and is largely independent of temperature. These materials, which have negative susceptibility, are classified as diamagnetic. In fact every material has an atomic diamagnetic component. But in atoms with non-zero and non-interacting magnetic moments subject to an external field, they tend to align in the direction of magnetic field giving positive and temperature dependent susceptibility. These materials having non interacting atomic magnets of positive temperature dependent susceptibility are called paramagnetic. However, the paramagnetic susceptibility of a non-interacting electron gas is independent of temperature and depends only upon the density of electronic states at the Fermi level. This susceptibility is called Pauli susceptibility and is given by [28]

$$\chi_{Pauli} = \mu_B^2 g\left(E_f\right) \qquad (2.6.3)$$

Where $g\left(E_f\right)$ is the density of electronic states at the Fermi level. The free electrons also have intrinsic diamagnetic reponse called Landau diamagnetism. This diamagnetism is also independent of temperature and is given by $\chi_{Landau} = -\frac{1}{3}\chi_{Pauli}$.

However, in a real solid, there is, in general, some interaction between individual magnetic moments, causing the loss of their individuality. This interaction between atoms or ions or molecules may extend up to several unit cells in the solid causing long range magnetic order. Such ordering results from two classes of interactions, discussed next.

2.6.1 Dipolar Interaction

This interaction depends upon strength, relative orientation and the separation between two magnetic dipoles. The interaction energy is given by [27]

$$E = \frac{\mu_0}{4\pi r^3}\left[\boldsymbol{\mu}_1 \bullet \qquad \hat{} \; , \qquad \bullet \qquad \bullet \qquad\right] \tag{2.6.4}$$

For μ_1, μ_2=1μ_B, r =1Å, E~1K. Thus, this interaction may not be responsible for high temperature ordering.

2.6.2 Exchange Interaction

This quantum mechanical interaction is responsible for most of the conventional and unconventional forms of magnetic ordering. The exchange Hamiltonian can be expressed as [27]

$$H = -\sum_{i,j} J_{ij}\mathbf{S}_\mathbf{i} \bullet \tag{2.6.5}$$

Where J_{ij} is the exchange constant between the ith and jth spins.

The exchange interactions can be further subclassified as: (a) Direct exchange (b) Superexchange (Indirect exchange) (c) RKKY interaction (d) Double exchange (e) Dzyaloshinsky-Moria (anisotropic) exchange. (f) Kondo exchange

(a) Direct Exchange

This type of interaction occurs between magnetic atoms whose orbital wave functions overlap directly [28]. If the neighboring atomic magnets are very close then the interaction favors antiferromagnetic ordering whereas if they are far then that favors weak ferromagnetic ordering.

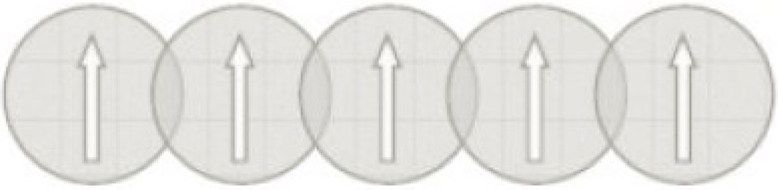

Figure 2.6.1 direct exchange between neighboring spins.

(b) Superexchange

This is the exchange interaction between non-neighboring magnetic ions which is mediated by a nonmagnetic intermediate ion [27]. In general, superexchange interaction leads to antiferromagnetic ordering; however for a particular situation it may produce weak ferromagnetism.

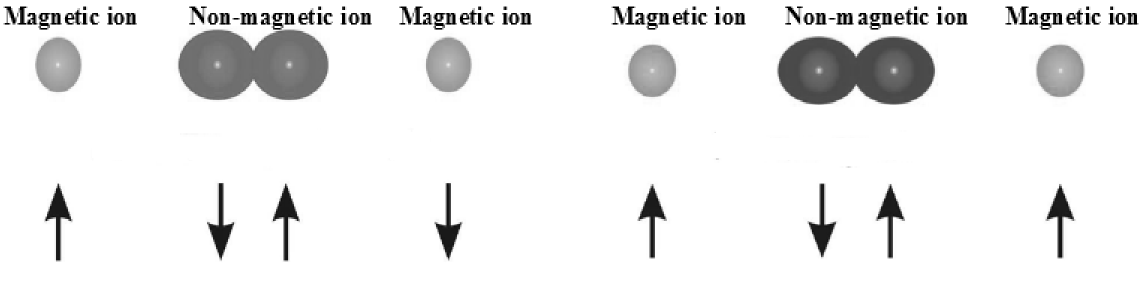

(a) Antiferromagnetic superexchange

(b) Ferromagnetic superexchange

Figure 2.6.2 Superexchange interaction between isovalent magnetic ions mediated by non-magnetic ions.

(c) RKKY Exchange

This is a weak exchange interaction between magnetic ions in metals or diluted semiconductors where the exchange is mediated by conduction electrons. A localized magnetic moment spin polarizes an electron which in turn interacts with other localized magnetic moments far from the previous one. The exchange interaction is oscillatory (changes from ferro to antiferro with distance) and varies inversely with cube of the distance between the magnetic ions. The exchange interaction can be written as [27]

$$J_{RKKY} = \frac{\cos\left(2k_f r\right)}{r^3} \qquad (2.6.6)$$

(d) Double Exchange

This is also similar to indirect ferromagnetic super exchange interaction. This type of interaction generally occurs between two non-neighboring magnetic ions of mixed valency mediated by nonmagnetic intermediate ion as shown in Figure 2.6.3. This leads to ferromagnetic interaction [27]. Furthermore, there is actual hopping of an electron from e_g level of one ion M_1 to that of another ion M_2. This means there is exchange of spin as well as charge which explains the name Double exchange.

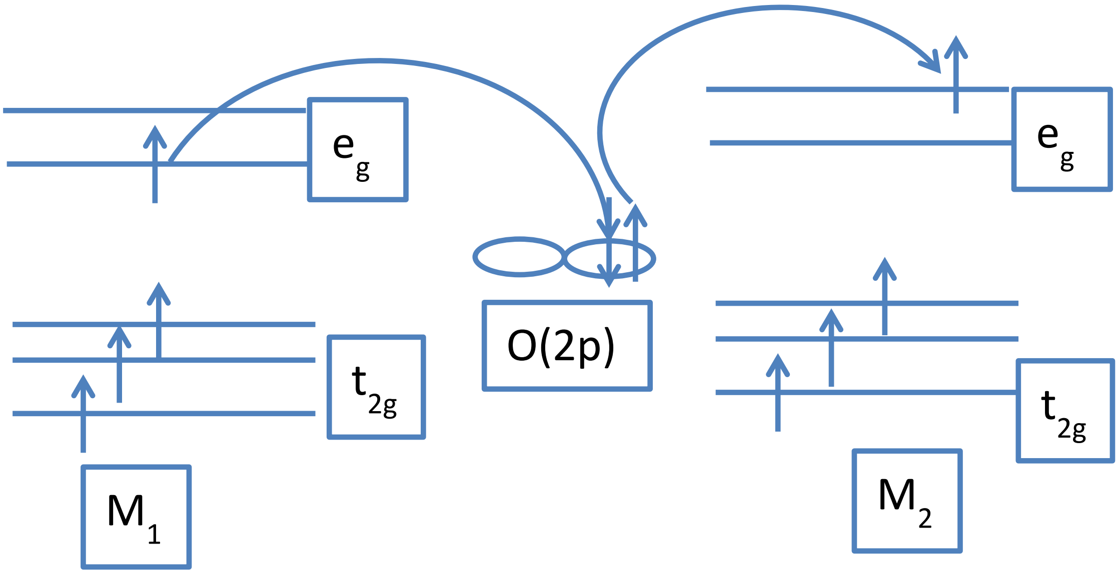

Figure 2.6.3 Double exchange between M_1 and M_2 magnetic ions. Note: the oxidation state of M_1 and M_2 are different.M_2 has initially one less electron.

(e) Dzyaloshinsky-Moria interaction

Dzyaloshinsky-Moria effects are in fact a combination of the superexchange interaction and spin orbit coupling, and it is anisotropic in nature. This interaction adds an anisotropic term in the Hamiltonian and is given by [43]

$$H = \mathbf{D}\bullet \qquad \textit{with } \boldsymbol{D} \propto (\boldsymbol{X} \times \boldsymbol{r}_{12}) \qquad (2.6.7)$$

Where $\boldsymbol{D}$ is Dzyaloshinsky-Moria [44] vector, and $\boldsymbol{S_1}$ and $\boldsymbol{S_2}$ are spins. The vector $\boldsymbol{D}$ vanishes when the crystal has inversion symmetry with respect to the center between the two magnetic ions. However, in general $\boldsymbol{D}$ may not vanish and will lie parallel or perpendicular to line connecting two spins. This interaction tries to force the spins to be at right angles to each other in a plane perpendicular to the vector $\boldsymbol{D}$ in such an orientation as to ensure that the energy is negative. The net effect is therefore canting of spins by small angle. The canting of spins in Sr_2IrO_4 and possibly on $Sr_3Ir_2O_7$ is explained on the basis of a non-trivial DM interaction.

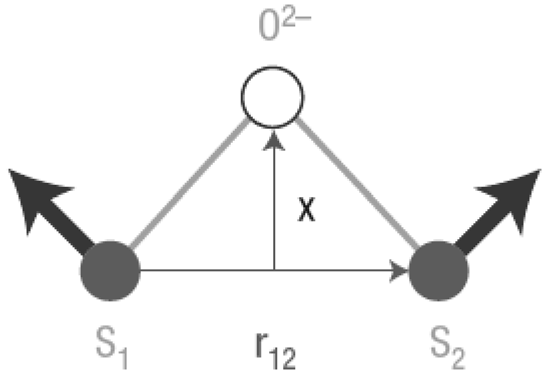

Figure 2.6 .4 DM interactions between two spins S_1 and S_2 [43]

(f) Kondo Exchange

This is the exchange interaction between localized magnetic impurity and delocalized electrons near this impurity that are present in the metallic host. At low temperature the spins of delocalized electrons start to align themselves to screen the spin on the local moment. This screening process creates a many body singlet state without any moment on Kondo site [54].

2.6.3 Magnetic Ordering

The exchange interaction between the atomic or ionic magnets can force them to arrange themselves into a particular configuration so as to minimize the free energy. This kind of arrangement of moments can extend up to several unit cells in the lattice, in which case the system is said to have long range ordering [28]. The chief categories of long range magnetic ordering found in materials are the following:

(a) Ferromagnetic Ordering

A positive exchange interaction J in eq. 2.6.5 gives spontaneous magnetization within certain regions in the solid where all the moments point to the same direction. This region is called a magnetic *domain* which can extend across several unit cells. However, magnetization of different domains may be in different directions. In presence of an external magnetic field, all the net moments of the domains point parallel to the field, causing a large magnetization signal. For fields above a given threshold, the alignment is complete and this is called *saturated magnetization*. The susceptibility of a ferromagnetic material depends upon temperature. The temperature below which the spontaneous alignment of moments within each domain begins is called the critical temperature $T_{C.}$ In the limit of zero magnetic fields the susceptibility of a ferromagnetic material at $T \geq T_C$ is given by Curie-Weiss law as [27]

$$\chi \propto \frac{1}{T - T_C} \qquad (2.6.8)$$

(b) Antiferromagnetic Ordering

If the exchange interaction J is negative then it is energetically favorable for nearest neighbor moments to align antiparallel to each other. This kind of ordering is called *antiferromagnetic* ordering. A perfect antiferromagnet can be decomposed into two interpenetrating sublattices, on one of which all the moments point up and on the other all the moments point down. The moments on two sublattices completely cancel each other giving zero magnetization in the absence of external magnetic field. If the moments on two neighboring sublattices do not cancel each other completely then the system is called *ferrimagnetic*. Similar to the ferromagnet, the spontaneous ordering within each sublattice begin below a critical temperature called Neel temperature T_N. In the limit of zero magnetic fields the susceptibility for $T \geq T_N$ is given by Curie-Weiss law as [27]

$$\chi \propto \frac{1}{T+T_N} \tag{2.6.9}$$

The susceptibility of paramagnetic, ferromagnetic and antiferromagnetic systems can be expressed in terms of a generalized Curie-Weiss law as [27]

$$\chi = \frac{C}{T-\theta} \tag{2.6.10}$$

Where C is called Curie constant and is given by

$$C = \frac{n\mu^2}{3K_B} \tag{2.6.11}$$

With n is the number density of magnetic moments, K_B is Boltzmann's constant, μ is the effective localized moment and θ is Weiss temperature. If $\theta = 0$,then there is no interaction between moments (paramagnetic). If $\theta > 0$,then the interactions are ferromagnetic and if $\theta < 0$, then the interactions are antiferromagnetic. The ratio between θ and T_C,T_N gives the measure of frustration.

In solids, the exchange interactions can stabilize an unusual non-collinear magnetic arrangement like a spin ice [45], a spin glass [46], helical order [47], a spin density waves [28] etc. Even collinear antiferromagnetic ordering can be of different types like G-type, C-type, A-type [48] etc. It is beyond the scope of this thesis to discuss them individually, but the interested reader can find a more detailed introduction to these magnetic structures elsewhere [48].

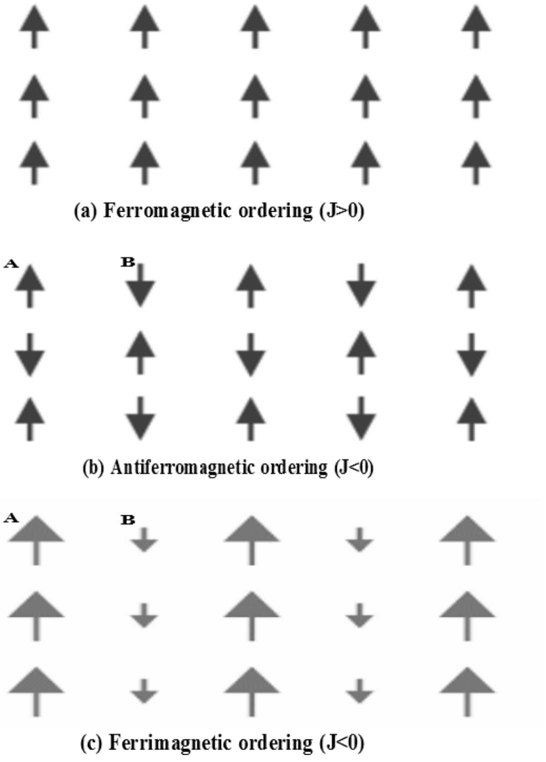

Figure 2.6.5 Different types of magnetic ordering. A and B refer to two sub lattices with opposite moments.

2.7 Magnetism in Iridates

In the strong spin orbit coupled system like RP iridates, the magnetic interactions cannot be determined by SU (2) symmetry of the spin alone (like in cuprates). There are two unique features of magnetism in a strong spin-orbit coupled systems [21] (1) orbitals of different symmetries are mixed which produce multidirectional exchange interactions. (2) The isotropic Heisenberg interactions can be suppressed by the anisotropic interactions like Pseudo-dipolar and Dzyaloshinsky-Moria interactions which may arise due to destructive interference among different superexchange pathways between different quantum phases of $J_{eff}=1/2$ states. Since orbitals of different symmetries are involved, a change in the lattice and bonding geometry can produce changes in the magnetic interactions. For the geometry relevant for RP iridates, the exchange Hamiltonian can be expressed as [8]: $H_{ij} = J_1 \mathbf{S}_i \bullet \qquad \bullet \qquad \bullet$, where the first term (J_1) represents isotropic AF Heisenberg exchange between $J_{eff}=1/2$ states (here $S_{i,j}$ represents $J_{eff}=1/2$ state), r_{ij} is the unit vector along ij bond. The second term represents anisotropic interlayer or intralayer coupling which is governed by the ratio of Hund coupling (J_H) to the Coulomb repulsion within the same orbital (U).

For Sr_2IrO_4, even in presence of strong spin-orbit coupling, the magnon dispersion can be described well with the phenomenological [49] J, J', J" model where J, J' and J'' correspond to first second and third nearest neighbor interactions respectively. Thus even with presence of $J_{eff}=1/2$ states, the low energy spin excitations can be described by an isotropic Hamiltonian, as in the cuprates with localized S=1/2 states. The spin structure is governed solely by the crystal structure and bonding geometry where the spins nearly follow the staggered rotation of octahedra. The moments lie in the ab plane with small canting relative to a unique axis.

On the other hand, in the bilayer compound $Sr_3Ir_2O_7$, the magnetic excitation spectra show significant deviations from isotropic Heisenberg interactions and has a giant magnon gap of 90 meV, even greater than magnon bandwidth of this system, 70 meV (90-160 meV) [22]. There is a spin flop transition from Sr_2IrO_4 (ab plane) to $Sr_3Ir_2O_7$ (G type with moment along c axis). Proposals have been put forward to explain this in terms of reduced coulomb interaction (U), increased Hund coupling and hence increased pseudo-dipolar interactions [22].

2.8 Neutron Scattering

Neutron scattering is a versatile technique that is well suited to study correlated electron systems. The neutron is a charge zero; spin one-half fermion having an intrinsic spin magnetic moment. This charge neutrality is helpful in studying the bulk properties of a sample without strongly interacting with the sample, and its non-zero magnetic moment make it useful for determining spin. Furthermore, the wavelength and energy of thermal neutrons match the order of atomic distances and the energy excitations of many interesting condensed matter systems. In a neutron scattering experiment, a monochromatic/polychromatic beam of neutrons hits the sample, interacts with it and is scattered from the sample. The energy-momentum spectrum of the scattered neutrons is measured along a particular direction or a range of directions. When a neutron with incident energy E_i $[E_i = (1/2)m_n v^2 = p^2/2m_n = h^2/2m_n\lambda^2]$ and wave vector $\boldsymbol{k_i}$ $(k_i=2\pi/\lambda_i)$ interacts with the sample then it is scattered with final energy E_f and wave vector $\mathbf{k_f}$ $(k_f=2\pi/\lambda_f)$ such that following energy momentum relations are satisfied [50]

$$\hbar \qquad \hbar \qquad\qquad (2.8.1)$$

$$\hbar \quad \hbar \quad \frac{\quad {}^{2})}{2m_n} \qquad (2.8.2)$$

Where **Q=q+ τ_{hkl}**, is the momentum transfer. **τ_{hkl}** is called reciprocal lattice vector and **q** is called the wave vector for elementary excitations. For **q=0, Q**= **τ_{hkl}** , we have elastic neutron scattering. The scattering process can be represented as shown in Figure 2.8.1

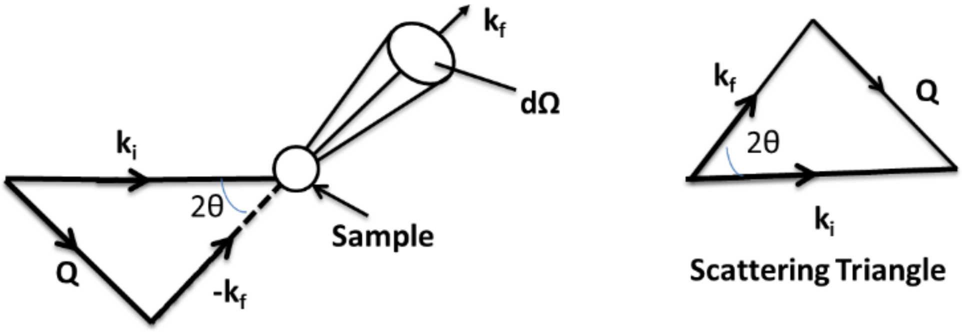

Figure 2.8.1 Schematic representation of scattering process

In a neutron scattering experiment, the quantity measured is the double differential cross section, defined as the number of neutrons scattered per second into a solid angle dΩ with energy transfers between ħω and ħ(ω+dω), divided by the incident neutron flux. The expression for the scattering cross section is governed by Fermi's golden rule and is given by [50]

$$\frac{d^2\sigma}{d\Omega d\omega} = \left(\frac{m}{2\pi\hbar}\right)^2 k_f \sum_{\lambda_f} \sum_{k_i,\lambda_i} p_{\lambda_i} p_{\lambda_f} \left(k_f,\sigma_f,\lambda_f|U|k_f,\sigma_f,\lambda_f\right)^2 \delta\left(\hbar \qquad -E_{\lambda_i}\right) \quad (2.8.3)$$

where λ_i, λ_f denote the initial and final state of the sample (scatterer) and $E_{\lambda i}$ and $E_{\lambda f}$ are initial and final energy of energy of the scatterer (sample) σ_i,σ_f are initial and final states of the neutron,p_λ is the thermal population factor, and p_σ is the polarization probability of neutron. The delta function describes the law of conservation of energy and U is the interaction operator that depends upon the specific scattering process.

Equation 2.8.3 is the master equation describing the interaction of thermal/cold neutrons with the sample.

2.8.1 Elastic Nuclear Scattering

Elastic nuclear scattering via neutrons is a versatile technique used for determination of crystal structure, atomic displacements, strains etc. The main advantage of this method is that the atomic scattering factor and hence the scattered intensity can be large even for the low atomic number element like oxygen. Thus crystal structure analysis of oxides is more efficient using this technique. For the neutrons scattering from fixed nuclei at position $\mathbf{R_j}$, the interaction potential is weak and can be approximated by Fermi pseudo potential as [50]

$$U(\mathbf{r})=\frac{2\pi\hbar}{m_n}\sum_j b_j\delta(\mathbf{r}-\mathbf{R_j}) \qquad (2.8.4)$$

Where b_j is the scattering length which depends upon which isotope is at the site R_j and on the spin states associated with that isotope. The magnitude of b_j is of the order 10^{-12} cm and hence the nuclear scattering cross section is of the order of 10^{-24} cm^2. For pure nuclear scattering, we can neglect spin states and represent state $|k_i\rangle$ and $|k_f\rangle$ by the plane waves $e^{i\mathbf{k}\bullet}$ and using these relations one can finally arrive at the nuclear scattering cross section as [50]

$$\frac{d^2\sigma}{d\Omega d\omega}=(\frac{1}{2\pi\hbar})(k_f)\sum\int_{-\infty}^{\infty}\left\langle e^{-i\mathbf{Q}\bullet\mathbf{R_{jf}}}(0)e^{-i\mathbf{Q}\bullet\mathbf{R_{ji}}}(t)\right\rangle e^{-i\omega t}dt \qquad (2.8.5)$$

Equation 2.8.5 can be written as [50]

$$\frac{d^2\sigma}{d\Omega d\omega}=(N)(\frac{k_f}{k_i})\sum_{j_i,j_f}b_{j_i}b_{j_f}S(\mathbf{Q},\omega) \qquad (2.8.6)$$

Where the quantity S(**Q**,ω) is called the scattering function of the system and is given by [50]

$$S(\mathbf{Q},\omega)=(\frac{1}{2\pi\hbar})\int^{\infty} I(\mathbf{Q},t)e^{-i\omega t}dt \qquad (2.8.7)$$

With

$$I(\mathbf{Q},t)=(\frac{1}{N})\sum_{j_i,j_f}\langle e-i\mathbf{Q}\bullet \qquad \bullet \qquad (2.8.8)$$

The Fourier transform of I(**Q**,t) is called the correlation function and is given by [50]

$$G(\mathbf{r},t)=(\frac{1}{2\pi^3})\int_{-\infty}^{\infty} I(\mathbf{Q},t)e^{-i\mathbf{Q}\cdot}\,d\mathbf{Q} \qquad (2.8.9)$$

Assuming that the isotopes and the spin states of the nuclei are distributed at random amongst all available sites and are uncorrelated between the sites, the quantity $b_{ji}b_{jf}$ can be replaced by ensemble average $\langle b_{j_i}b_{j_f}\rangle$. For $j_f \neq j_i$ and no correlation between two sites one can write $b_{j_i}b_{j_f}=\langle b_{j_i}b_{j_f}\rangle=\langle b_{j_f}\rangle\langle b_{j_i}\rangle=(\langle b\rangle)^2$ and for $j_f = j_i$, $b_{j_i}b_{j_f}=\langle b_{j_i}b_{j_f}\rangle=\langle b_{j_i}^2\rangle=(\langle b^2\rangle)$. Using these relations and rearranging the terms, the differential cross section can be written as sum of two components: coherent and incoherent scattering. In coherent scattering, the scattered intensity from different nuclei interfere each other whereas in incoherent scattering they are independent of each other. For coherent scattering the coherent diffraction peaks from Bragg scattering are determined by magnitude of $\langle b\rangle^2$ and the incoherent scattering gives a flat background determined by magnitude of$\left(\langle b^2\rangle-\langle b\rangle^2\right)$. Therefore, equation 2.8.6 can be split into two equations [50]

$$\left(\frac{d^2\sigma}{d\Omega d\omega}\right)_{coh} = (N)(\frac{k_f}{k_i})\langle b\rangle^2 S_{coh}(\mathbf{Q},\omega) \qquad (2.8.10)$$

And

$$\left(\frac{d^2\sigma}{d\Omega d\omega}\right)_{incoh} = (N)(\frac{k_f}{k_i})\left(\langle b^2\rangle - \langle b\rangle^2\right)S_{incoh}(\mathbf{Q},\omega) \qquad (2.8.11)$$

For the coherent scattering the total cross-section is given by the squared average of sum of scattering lengths

$$\sigma_{coh} = 4\pi\langle b\rangle^2 \qquad (2.8.12)$$

Whereas for the incoherent scattering the total cross-section is given by [50]

$$\sigma_{incoh} = 4\pi\left[\langle b^2\rangle - \langle b\rangle^2\right] \qquad (2.8.13)$$

The difference between coherent and incoherent scattering is large in hydrogen ($\sigma_{incoh} = 80.3, \sigma_{coh} = 1.76$) whereas it is small in deuterium ($\sigma_{incoh} = 2.05, \sigma_{coh} = 5.59$).The units of$\sigma's$ are in *barns*.This fact is very helpful in distinguishing hydrogen and deuterium. For elastic coherent scattering from a real lattice with more than one atom per unit cell, one can write the differential cross-section by integrating double differential cross section with respect to energy as [50]

$$\left(\frac{d\sigma}{d\Omega}\right)_{coh} = (N_0)(\frac{2\pi^3}{V_0})e^{-2W(Q)}\sum_{\tau}|S_\tau|^2\delta(\mathbf{Q}-\tau) \qquad (2.8.14)$$

Here N_0 is the number of unit cells, V_0 is the unit cell volume, $e^{-2W(Q)}$ is called Debye-Waller factor and the delta function implies Q=τ, the reciprocal lattice vector. S_τ is called structure factor and is given by [50]

$$S_\tau = \sum_{d_j} b_{d_j} e^{i\boldsymbol{\tau}\bullet} \qquad (2.8.15)$$

Here d_j represents the position of j^{th} atom in the unit cell w.r.t origin of that unit cell.

In inelastic scattering, the neutron either losses or gains energy by interacting with lattice excitations or magnetic excitations. Thus this method is helpful to study the lattice and spin dynamics of the system. I will not give details of inelastic scattering here but the details can be found elsewhere [51]

2.8.2 Elastic Magnetic Scattering

One of the core reasons for using neutron scattering is that it is an ideal probe for solving magnetic structures and determining the ordered magnetic moment. This benefit comes from the fact that the neutron has its own non-zero magnetic moment which interacts with the magnetic field generated by the moments of unpaired electrons in the sample. For magnetic scattering the interaction potential U in equation 2.8.3 is given by [50]

$$U = \mu \bullet \qquad\qquad \bullet \tag{2.8.16}$$

Where μ is the magnetic moment operator of the neutron, γ = -1.91 is the gyromagnetic ratio, $\mu_N = 5.05079 \times 10^{-27}$ J/T is the nuclear magnetron, and $\boldsymbol{\sigma}$ is the Pauli spin operator. For most of the magnetic compounds the field H is generated by unpaired electrons. The magnetic field due to a single electron moving with velocity v_e is given by [50]

$$\mathbf{H} = \nabla \times \left(\frac{\mu_e \times \mathbf{R}}{R^3} \right) - \frac{e}{c} \left(\frac{\mathbf{v_e} \times \mathbf{R}}{R^3} \right) \tag{2.8.17}$$

Where R is the distance from the electron to the point where the field is measured, e is the electron charge; c is the speed of light in vacuum. The magnetic moment of an electron is given by

$$\boldsymbol{\mu}_e = -2\mu_B \mathbf{S} \qquad (2.8.18)$$

Where μ_B =9.27402 × 10^{-24} J/T is the Bohr magnetron and S is the spin operator of the electron. The first term in field equation comes from spin of electron whereas the second term comes from the orbital motion. Using U in equation 2.8.3 and considering an assembly of identical magnetic ions with localized electrons, the differential cross-section for spin only scattering of unpolarized neutrons can be expressed as [50]

$$\frac{d^2\sigma}{d\Omega d\omega} = (\gamma a_o)^2 \frac{k_f}{k_i} F^2(\mathbf{Q}) e^{-2W(Q)} \sum_{\alpha,\beta} \left(\delta_{\alpha\beta} - \frac{Q_\alpha Q_\beta}{Q^2} \right) S^{\alpha\beta}(\mathbf{Q},\omega) \qquad (2.8.19)$$

Where $S_{\alpha\beta}$ ($\mathbf{Q}$,ω) is called the magnetic scattering function and is given by [50]

$$S^{\alpha\beta}(\mathbf{Q},\omega) = \sum_{j_i, j_f} e^{i\mathbf{Q}\cdot} \quad) \sum_{\lambda_i,\lambda_f} p_\lambda \left\langle \lambda_i \middle| S_{j_f}^{\alpha} \middle| \lambda_f \right\rangle \left\langle \lambda_f \middle| S_{j_i}^{\beta} \middle| \lambda_i \right\rangle \delta\left(\hbar \quad - E_{\lambda_f}\right) \qquad (2.8.20)$$

F($\mathbf{Q}$) is the dimensionless magnetic form factor defined as the Fourier transform of the normalized spin density associated with the magnetic ions, $e^{-2W(Q)}$ is the Debye-Waller factor, and $S_j^{\alpha} (\alpha = x, y, z)$ is the spin operator of the jth atom at position $\mathbf{R}_j$. From the size of Bohr radius a_o, the magnetic cross-section is also of the order of 10^{-24} cm^2 similar to that of nuclear scattering cross-section. This fact makes neutron scattering a unique probe for magnetism. There are two important facts about magnetic neutron scattering in equation 2.8.19: (a) as the magnetic form factor falls off with increasing modulus of Q so does the differential cross section. (b) The factor $\left(\delta_{\alpha\beta} - \frac{Q_\alpha Q_\beta}{Q^2} \right)$,also called polarization/Orientation factor shows that neutrons can only interact with moments that are perpendicular to the scattering vector Q. This gives neutron a unique ability to predict direction of spins as well as spin fluctuations.

Equation 2.8.19 holds strictly for the spin only system where orbital motion is quenched. However, for the spin orbit coupled system an approximate result can be obtained for intermediate Q by replacing spin operator S as [50]

$$S_j^{\alpha} = \frac{1}{2} g J_j^{\alpha} \tag{2.8.21}$$

With

$$\mathrm{g} = 1 + \frac{\mathrm{J}(\mathrm{J}+1) - \mathrm{L}(\mathrm{L}+1) + \mathrm{S}(\mathrm{S}+1)}{2J(J+1)} \tag{2.8.22}$$

g is called Lande's splitting factor and J_j^{α} is the effective angular momentum operator.

Using the integral form of delta function in equation 2.8.20 as [50]

$$\delta\left(\hbar \qquad - E_{\lambda_f}\right) = \frac{1}{2\pi\hbar} \int^{\infty} \frac{i(E_{\lambda_f} - E_{\lambda_i})t}{\hbar} \qquad {}^{-i\omega t} dt \tag{2.8.23}$$

The expression for magnetic scattering function can be written as [50]

$$S^{\alpha\beta}(\mathbf{Q},\omega) = \frac{1}{2\pi\hbar} \sum {}^{i\mathbf{Q}\cdot} \qquad) \left\langle S_{j_i}^{\alpha}(0) S_{j_f}^{\beta}(t) \right\rangle e^{-i\omega t} dt \tag{2.8.24}$$

Thus the magnetic scattering function is a Fourier transform of the spin pair correlation function $\left\langle S_{j_i}^{\alpha}(0) S_{j_f}^{\beta}(t) \right\rangle$. The cross-section for elastic magnetic scattering ($\hbar \qquad \rangle = \left| k_f \right\rangle$) is obtained by integrating equation 2.8.19 and using equation 2.8.24 as [50]

$$\frac{\mathrm{d}\sigma}{\mathrm{d}\Omega} = \left(\gamma a_o\right)^2 F^2(\mathbf{Q}) e^{-2W(Q)} \sum_{\alpha,\beta} \left(\delta_{\alpha\beta} - \frac{Q_\alpha Q_\beta}{Q^2} \right) \sum_{l} \left\langle S_0^{\alpha} \right\rangle \left\langle S_l^{\beta} \right\rangle \tag{2.8.25}$$

Where $\mathbf{l} = \mathbf{R}_{ji} - \mathbf{R}_{jf}$.

The expression for the cross-section of inelastic magnetic scattering involves additional steps and will not be presented here, though it can be found elsewhere [50,52].

2.8.3 Polarized Neutron Scattering

Polarized neutron scattering is the confirmatory experiment to distinguish between either a magnetic or structural origin of some superlattice peak. This technique takes the advantage of the fact that neutron can only be scattered by the moments that are perpendicular to scattering vector Q. A neutron is a spin ½ fermion having two possible spin states (i) up or $|+\rangle$ or $|\uparrow\rangle$ (ii) down or $|-\rangle$ or $|\downarrow\rangle$ These states are the Eigen states of the Pauli spin operator σ_z (taking z axis as the polarization direction) with eigenvalues +1 and -1 respectively. During the scattering process the neutron scattering cross-section can be split into four parts [50].

1. $|+\rangle \rightarrow |+\rangle$
2. $|-\rangle \rightarrow |-\rangle$
3. $|+\rangle \rightarrow |-\rangle$
4. $|-\rangle \rightarrow |+\rangle$

The first two are Non Spin Flip (NSF) scattering and the last two are Spin Flip (SF) scattering. Considering the spin states during the scattering process the interaction operator U in equation 2.8.3 can be written as [50]

$$U = \hat{} \qquad \bullet \qquad \bullet \tag{2.8.26}$$

Where *I* is the nuclear spin and *m* is the magnetic moment of the sample (unpaired electron). Using the orthogonality of spin and momentum states of the neutron, the matrix element of U in equation 1.8.3 can be expressed as [50]

$$\begin{aligned} \langle + | U | + \rangle &= b + AI_z + BM_z, \\ \langle - | U | - \rangle &= b - AI_z - BM_z, \\ \langle - | U | + \rangle &= A(I_x + iI_y) + B(M_x + iM_y), \\ \langle + | U | - \rangle &= A(I_x - iI_y) + B(M_x - iM_y) \end{aligned} \tag{2.8.27}$$

Assuming neutron polarization is along z direction and neglecting nuclear spin scattering, the following conclusions can be made (i) if the neutron polarization is along scattering vector Q, then all the spin flip scattering is magnetic and all the non-spin flip scattering is nuclear. (ii) if the neutron polarization is perpendicular to scattering vector Q,then non-spin flip scattering consists of nuclear plus the magnetic scattering arising from the moment parallel to neutron polarization whereas the spin flip scattering consists of magnetic scattering from moments which are perpendicular to both Q and the neutron polarization. Thus polarized neutron scattering is a confirmatory experiment for finding the origin of any superlattice peak (nuclear or magnetic) as well as the determination of systems magnetic moment orientations.

Chapter 2 References

[1] D. Pesin and L. Balents, Nature Physics **6**, 376 (2010).

[2] X. Wan, A. M. Turner, A. Vishwanath, and S. Y. Savrasov, Physical Review B **83** (2011).

[3] Y. Okamoto, M. Nohara, H. Aruga-Katori, and H. Takagi, Phys. Rev. Lett. **99** (2007).

[4] S. M. Disseler, S. R. Giblin, C. Dhital, K. C. Lukas, S. D. Wilson, and M. J. Graf, Physical Review B **87** (2013).

[5] J. Chaloupka, G. Jackeli, and G. Khaliullin, Phys. Rev. Lett. **105**, 027204 (2010).

[6] Y. Machida, S. Nakatsuji, Y. Maeno, T. Tayama, and T. Sakakibara, J Magn Magn Mater **310**, 1079 (2007).

[7] B. J. Kim, H. Ohsumi, T. Komesu, S. Sakai, T. Morita, H. Takagi, and T. Arima, Science **323**, 1329 (2009).

[8] G. Jackeli and G. Khaliullin, Phys. Rev. Lett. **102** (2009).

[9] B. J. Kim, H. Jin, S. J. Moon*, et al*, Phys. Rev. Lett. **101** (2008).

[10] F. Wang and T. Senthil, Phys. Rev. Lett. **106** (2011).

[11] R. Arita, J. Kunes, A. V. Kozhevnikov, A. G. Eguiluz, and M. Imada, Phys. Rev. Lett. **108** (2012).

[12] Q. Huang, J. L. Soubeyroux, O. Chmaissem, I. Natalisora, A. Santoro, R. J. Cava, J. J. Krajewski, and W. F. Peck, Journal of Solid State Chemistry **112**, 355 (1994).

[13] N. S. Kini, A. M. Strydom, H. S. Jeevan, C. Geibel, and S. Ramakrishnan, Journal of Physics-Condensed Matter **18**, 8205 (2006).

[14] M. K. Crawford, M. A. Subramanian, R. L. Harlow, J. A. Fernandezbaca, Z. R. Wang, and D. C. Johnston, Physical Review B **49**, 9198 (1994).

[15] G. Cao, J. Bolivar, S. McCall, J. E. Crow, and R. P. Guertin, Physical Review B **57**, 11039 (1998).

[16] J. P. Clancy, N. Chen, C. Y. Kim, W. F. Chen, K. W. Plumb, B. C. Jeon, T. W. Noh, and Y. Kim, Physical Review B **86** (2012).

[17] D. Hsieh, F. Mahmood, D. H. Torchinsky, G. Cao, and N. Gedik, Physical Review B **86** (2012).

[18] F. Ye, S. Chi, B. C. Chakoumakos, J. A. Fernandez-Baca, T. Qi, and G. Cao, Physical Review B **87** (2013).

[19] S. Boseggia, R. Springell, H. C. Walker, A. T. Boothroyd, D. Prabhakaran, S. P. Collins, and D. F. McMorrow, Journal of Physics-Condensed Matter **24** (2012).

[20] G. Cao, Y. Xin, C. S. Alexander, J. E. Crow, P. Schlottmann, M. K. Crawford, R. L. Harlow, and W. Marshall, Physical Review B **66** (2002).

[21] J. W. Kim, Y. Choi, J. Kim, J. F. Mitchell, G. Jackeli, M. Daghofer, J. van den Brink, G. Khaliullin, and B. J. Kim, Phys. Rev. Lett. **109** (2012).

[22] J. Kim, A. H. Said, D. Casa, M. H. Upton, T. Gog, M. Daghofer, G. Jackeli, J. van den Brink, G. Khaliullin, and B. J. Kim, Phys. Rev. Lett. **109** (2012).

[23] P. D. C. King, T. Takayama, A. Tamai*, et al*, Physical Review B **87** (2013).

[24] I. Nagai, Y. Yoshida, S. I. Ikeda, H. Matsuhata, H. Kito, and M. Kosaka, Journal of Physics-Condensed Matter **19** (2007).

[25] M. A. Subramanian, M. K. Crawford, and R. L. Harlow, Mater. Res. Bull. **29**, 645 (1994).

[26] Q. Wang, Y. Cao, J. A. Waugh, S. R. Park, T. F. Qi, O. B. Korneta, G. Cao, and D. S. Dessau, Physical Review B **87** (2013).

[27] S. Blundell and D. Thouless, *Magnetism in condensed matter* (Oxford University Press New York, 2001), 1.

[28] N. Ashcroft and N. Mermin, Holt-Saunders, Philadelphia **16** (1976).

[29] M. M. Sala, S. Boseggia, D. McMorrow, and G. Monaco, Phys. Rev. Lett. **112**, 026403 (2014).

[30] S. Ruddlesden and P. Popper, Acta Crystallogr. **10**, 538 (1957).

[31] S. Ruddlesden and P. Popper, Acta Crystallogr. **11**, 54 (1958).

[32] K. Momma and F. Izumi, Journal of Applied Crystallography **44**, 1272 (2011).

[33] F. Gebhard, *Metal—Insulator Transitions* (Springer, 1997).

[34] P. W. Anderson, Science **235**, 1196 (1987).

[35] J. Slater, Physical Review **82**, 538 (1951).

[36] J. Hubbard, Proceedings of the Royal Society of London.Series A.Mathematical and Physical Sciences **276**, 238 (1963).

[37] N. Mott, Journal of Solid State Chemistry **88**, 5 (1990).

[38] M. Imada, A. Fujimori, and Y. Tokura, Reviews of Modern Physics **70**, 1039 (1998).

[39] V. K. Shante and S. Kirkpatrick, Adv. Phys. **20**, 325 (1971).

[40] J. Wu and C. Leighton, Physical Review B **67**, 174408 (2003).

[41] J. Bass, W. P. Pratt Jr, and P. A. Schroeder, Reviews of modern physics **62**, 645 (1990).

[42] U. Mizutani, *Introduction to the electron theory of metals* (Cambridge University Press, 2001).

[43] S. Cheong and M. Mostovoy, Nature materials **6**, 13 (2007).

[44] T. Moriya, Physical Review **120**, 91 (1960).

[45] H. Diep, *Frustrated spin systems* (World Scientific, 2005).

[46] K. H. Fischer and J. A. Hertz, *Spin glasses* (Cambridge University Press, 1993), 1.

[47] F. Nori and A. Tonomura, Science **311**, 344 (2006).

[48] E. Dagotto, *Nanoscale phase separation and colossal magnetoresistance: the physics of manganites and related compounds* (Springer, 2003).

[49] J. Kim, D. Casa, M. Upton, T. Gog, Y. Kim, J. Mitchell, M. Van Veenendaal, M. Daghofer, J. van Den Brink, and G. Khaliullin, Phys. Rev. Lett. **108**, 177003 (2012).

[50] A. Furrer, J. Mesot, T. Strässle, and J. Mesot, *Neutron scattering in condensed matter physics* (World Scientific Singapore, 2009).

[51] S. W. Lovesey and S. Lovesey, *Theory of neutron scattering from condensed matter* (Clarendon Press Oxford, 1984), 1.

[52] S. W. Lovesey and S. Lovesey, *Theory of neutron scattering from condensed matter* (Clarendon Press Oxford, 1984), 1.

[53] http://2012books.lardbucket.org/books/principles-of-general-chemistry-v1.0m/s27-05-crystal-field-theory.html

[54] N. Ashcroft and N. Mermin, Holt-Saunders, Philadelphia **16** (1976).

Chapter 3: Experimental Techniques

3.1 Crystal Growth

A single crystal is defined as a periodic spatial arrangement of atoms, ions or groups of ions in 3 dimensions [1]. The repeating periodic distance along certain direction is called the *lattice parameter* and the smallest repeating unit is called *unit cell*. For inorganic crystals, the lattice parameter may extend up to 30 nm while for organic crystals it can extend even up to hundreds of nanometers. In an ideal single crystal, the long range periodic order should extend to infinity. However, in a real crystal, due to presence of finite surfaces and defects, the long range periodic order is finite. Therefore, truly speaking a single crystal is defined as such by comparison to polycrystalline and amorphous materials. For a scientific study and technological applications, a single crystal is usually preferred over a polycrystalline sample due to the following reasons: (i) Single crystals carry information about anisotropy of physical properties which otherwise average out to zero in polycrystals (ii) They are relatively free from grain boundary scatterings which is often the case in polycrystalline samples (iii) In polycrystals, typically, there exist large internal stresses.(iv) single crystals are relatively free of impurities compared to polycrystals. There are four main categories of crystal growth techniques (i) Solid growth (ii) Vapor growth (iii) Melt growth (iv) Solution growth. Figure 3.1.1 shows the summary of crystal growth techniques [2].

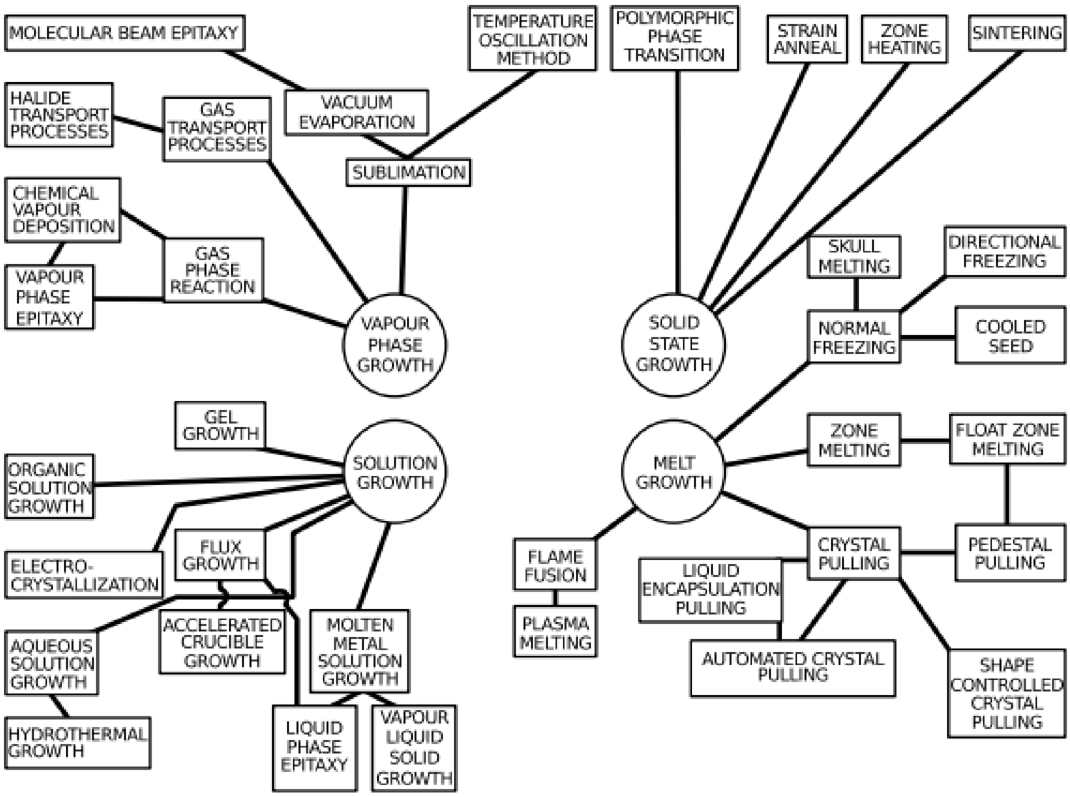

Figure 3.1.1 Crystal growth techniques [2].

For our present study we mostly use Flux growth (a kind of solution growth).

3.1.1 Flux Growth Method

This is a kind of solution growth method where the solvent allows solutes to form crystals well below their melting point. Generally the solvent helps the solute to crystalize but does not itself enter into the crystal. This method is particularly useful if the materials forming crystals have high a melting point, decompose before melting, have high vapor pressure or have different volatilities. A typical sequence consists of heating the mixture up to a temperature where a supersaturated solution is formed and then slowly cooling down to a temperature below the melting point of the solvent. The following factors should be taken into account while choosing a solvent [2]

(i) High solubility for the solutes

(ii) Low viscosity

(iii) Low melting point

(iv) Low toxicity

(v) High purity at low cost

(vi) Easy to remove by dissolving

In the present work I studied Sr_2IrO_4, $Sr_3Ir_2O_7$ and $Sr_3(Ir_{1-x}Ru_x)_2O_7$ single crystals. For all crystals, we used $SrCl_2$ as solvent and stoichiometric ratios of IrO_2, $SrCO_3$ and RuO_2 as solute. The materials were put layer by layer (in the increasing order of melting point from the top) with the solvent at the top layer in a platinum crucible. The mixture was heated up to 1300^0C-1400^0C using Sentrotech high temperature (1600^0C max.) furnaces and then slowly cooled down to melting point of $SrCl_2$ (850^0C). The details of the crystal preparation methods are given in [3].

3.2 X-ray Diffraction

X-rays have wavelengths comparable to the typical interatomic distance (10^{-10} m) in a crystal so they can be used to study the crystal structures. When a monochromatic/polychromatic beam of X-rays hits the sample, it interacts with the sample (actually the outer electron clouds) and gets scattered. In diffraction, we are concerned only with the elastic interaction. The scattered X-rays from different planes can interfere constructively to give maximum intensity if their path difference is integer multiple of incident wavelength. This is called Bragg's law and can be written as [4]

$$2\mathrm{dSin}\theta = \mathrm{n}\lambda \qquad \mathrm{n} = 1,\ 2,\ 3\ldots. \qquad (3.2.1)$$

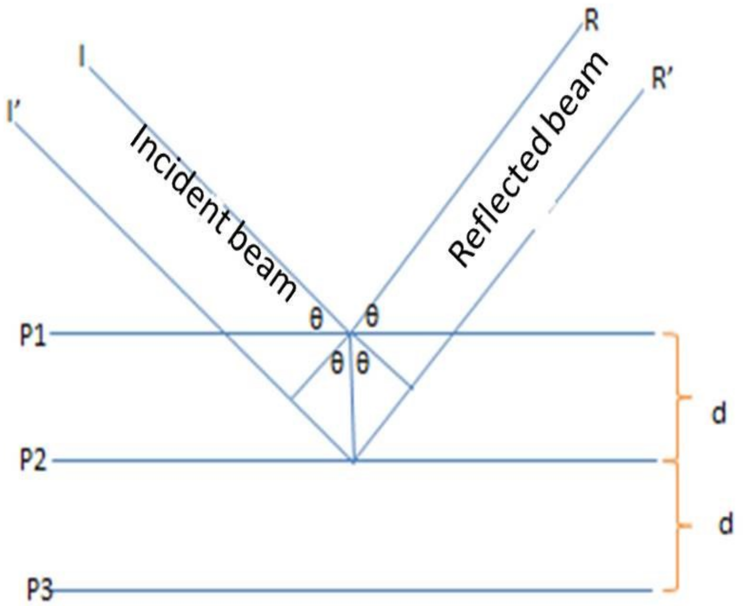

Figure 3.2.1 Bragg's reflection from a particular family of lattice planes separated by distance *d*

The most important point about X-ray diffraction is that each material has its own unique diffraction pattern. At a fixed wavelength, the position of intensity maxima is determined by the interplanar spacing (*d*) or, in other words, the symmetry group of the crystal and the lattice parameters of the crystal. The intensity of scattering maxima is determined by the actual scattering elements, their positions within the unit cell, the absorption coefficient of the material and the sample temperature. For X-rays the scattering power of elements depends directly upon their atomic numbers. Even a slight change in crystal structure or change in atomic position gives different scattering pattern. Generally X-ray diffraction is used to identify structural/chemical phase, to determine lattice parameters, to determine the residual stress and occasionally the crystallites' size. For our present study, we used a D2 Phaser X-ray diffractometer from the Bruker Company. Figure 3.2.2 shows the diffractometer that is used for these studies at Boston College. A number of crystals from same batch were ground and then powder diffraction patterns were taken. The powder pattern thus obtained was matched with the standard powder pattern to check for the phase purity. The lattice parameters of the samples were determined by refining the powder data using software such as FullProf.

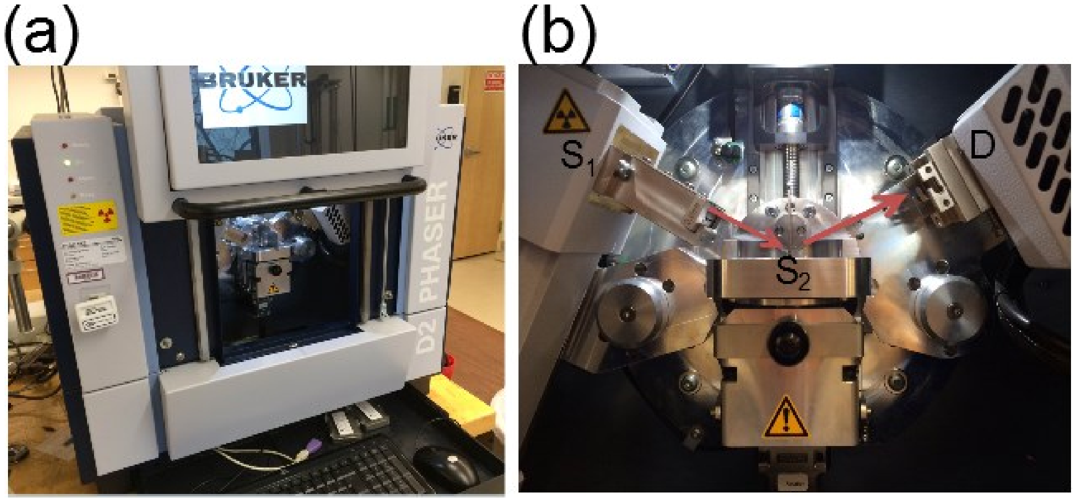

Figure 3.2.2 (a) Bruker X-ray diffractometer in Wilson lab at Boston College (b) Inner part of diffractometer S_1=source, S_2=sample, D=detector and red arrows represent incident and scattered X-rays.

3.3 Energy Dispersive Spectroscopy (EDS)

This technique takes advantage of the fact that when an energetic electron beam hits the sample surface, X-rays are emitted. The frequency of these X-rays is characteristics of the elements present in the sample. The energy spectra of emitted x-rays help to identify the elemental makeup whereas the intensity of the peak in the characteristic spectrum gives the compositional concentration of that element. The energy of the emitted x-ray is given by Mosley's law [5]: $E = C_1(Z - C_2)^2$, where E is the energy of emitted X-rays, Z is the atomic number of emitter and C_1 and C_2 are constants. Similarly, the peak to background ratio (P/B) of the characteristic X-ray is given by [5]

$$\frac{P}{B} = \frac{1}{Z}\left[\frac{E_0 - E_C}{E_C}\right]^{n-1} \tag{3.3.1}$$

Where E_C is critical ionization energy, Eo is the accelerating voltage, Z the atomic number and N is a constant. For the elemental analysis of our samples, we used an EDS system connected to a JEOL scanning electron microscope at Boston College. Further details concerning scanning electron microscopy can be found in Joseph et.al [5]

3.4 Resistivity Measurement

All the resistivity measurements were carried out using a standard four probe technique. The resistivity measurements in presence of magnetic field were carried out using Quantum Design Physical Property Measurement System (PPMS) in up to 9T (located in the laboratory of Professor Opeil at Boston College). The zero field measurements were carried out using Keithley 6220 and 6221 current sources and Keithley 2182 nanovoltmeter and Lakeshore Model 370 AC Resistance Bridge inside an Advanced Research Systems cryostat down to 4K (Wilson Lab, Boston College). The temperature was controlled using Lakeshore Model 335 temperature controller and DT670 thermometers. Figure 3.4.1 shows the ARS cryostat setup in the Wilson lab during this work.

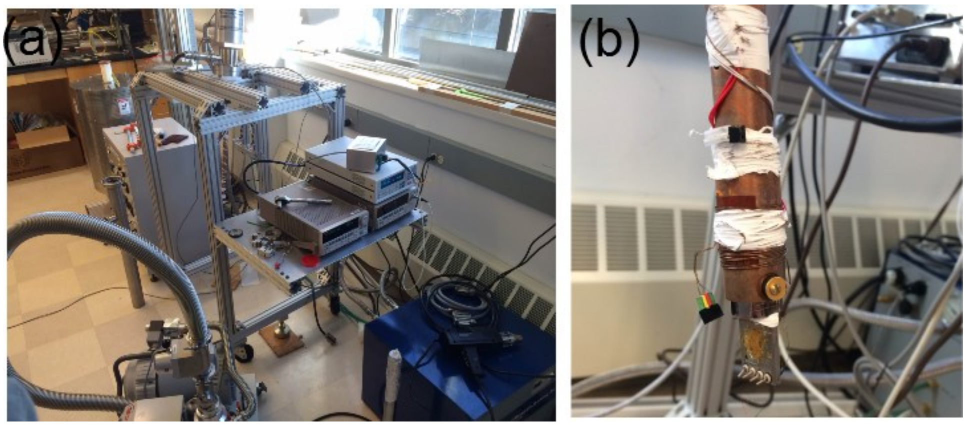

Figure 3.4.1(a) ARS cryostat and associated electronics in Wilson lab (b) sample mount in cryostat.

3.5 Magnetization Measurement

Magnetization measurements can be done using different devices such as a SQUID magnetometer, VSM (vibrating sample magnetometer), torque magnetometer etc. Generally, a small magnetic field is applied to give some net moment even for paramagnetic or diamagnetic materials. If the sample is cooled in zero fields and then small field is applied this data is labeled as a zero field cooled (ZFC) measurement. If the field is applied during cooling then it is called a field cooled (FC) measurement. In the present work the DC magnetization measurements were carried out using Superconducting Quantum Interference Device (SQUID) within a MPMS (Magnetic Property Measurement System) at the Massachusetts Institute of Technology (MIT). A SQUID is a superconducting loop interrupted by thin non-superconducting (insulating) junction(s) called Josephson junctions. It works on the principle of Josephson tunneling and flux quantization which utilizes the fact that the magnetic flux passing through a superconducting loop must be quantized in units of h/2e or 2.064×10^{-15} Wb [1,4]. The current through this junction depends upon the phase difference between the superconducting wave functions on either side of the junctions and the voltage drop across this junction depends upon the time derivative of this phase difference [9]. The magnetic moment on the sample produces a change in magnetic flux on the squid via the combination of pick-up coil and signal to flux converter. This change in flux in turn changes the phase difference between the superconducting wave functions on either side of junction. The time derivative of this phase change is in turn converted to voltage signal. The details of a SQUID and its working principles can be found in Clark et.al [6].

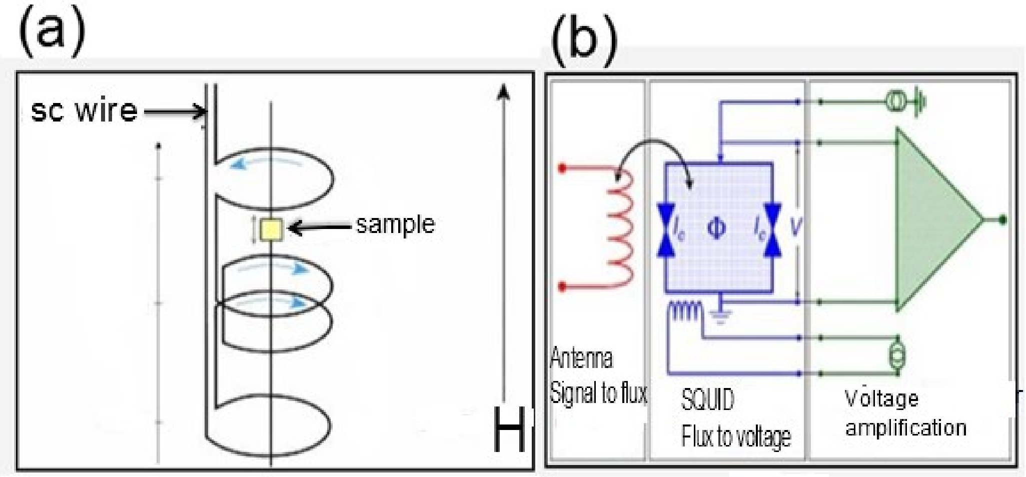

Figure 3.5.1 (a) Squid pick up coil (b) Squid loop (blue), primary coil (red) attached to pick up coil on one side and squid on other side along with other electronics to change flux to voltage [9].

3.6 Thermogravimetric Analysis

Thermogravimetric analysis is a technique in which the weight of a substance is monitored as function of temperature and/or time as the substance is subjected to some controlled temperature program in presence of controlled atmosphere. This technique can be used to determine mass changes, phase transitions etc. [7] .We use TGA/DSC-1 from Mettler Toledo to determine the mass change as function of temperature as well as effect of annealing in different gas atmospheres.

3.7 Neutron Scattering

A neutron scattering experiment can only be performed in certain big facilities around the world because the neutrons are located deep inside the atom (nucleus) which costs a huge amount of energy to make them escape. Ironically, one has to travel around the world to get the neutrons that are inside a very small nucleus. There are two types of sources of neutrons (i) reactor source (ii) spallation source. A reactor source produces neutron by nuclear fission process where a fission of heavy nucleus (e.g ^{235}Uor ^{239}Pu) by a slow neutron produces on the average of 2.7 fast neutrons and the simultaneous disintegration of the heavy nucleus into two fission fragments of unequal mass [8]. The neutrons thus produced cause further fission and hence a self-sustained chain reaction is initiated. This chain reaction produces huge amount of highly energetic neutrons. The energy of neutrons produced in the fission process is around 2 MeV. A reactor based source produces a continuous flux of neutrons.

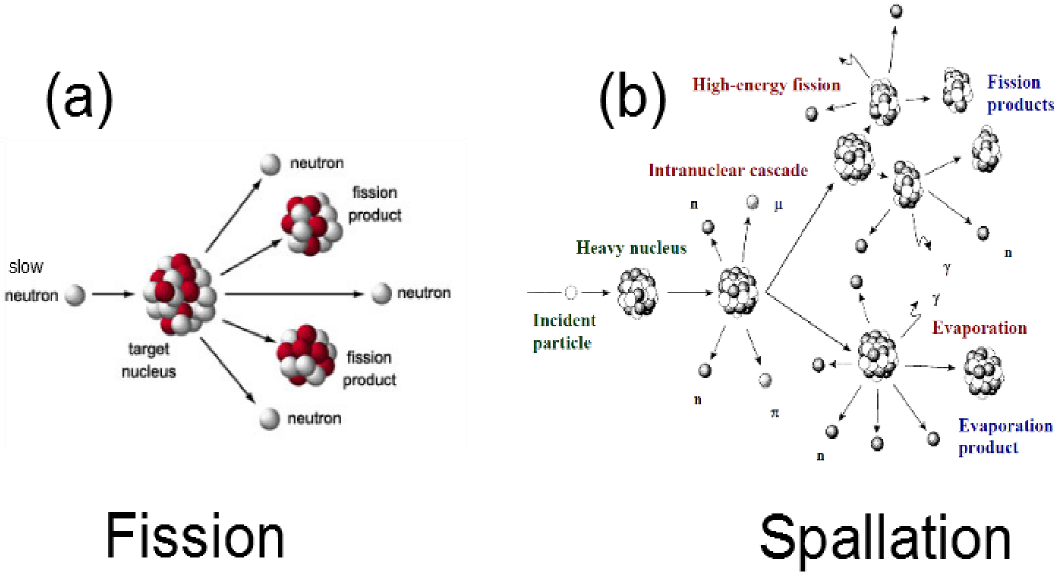

Figure 3.7.1 (a) A nuclear fission process (b) spallation process [9].

In the spallation source, the target nuclei are bombarded with highly energetic beam (GeV range) of protons. For highly energetic particle, the de Broglie wavelength $\lambda = \frac{h}{\sqrt{2mE}}$, becomes shorter than the linear dimension of the nucleus [8]. Thus the energetic particle can directly interact with the nuclides inside the nucleus of target. This makes target nuclei highly unstable ultimately causing a cascade process with release of neutrons as shown in Figure 3.7.1 (b). The release of spallation neutrons takes place within less than 10^{-15} s after the nucleus was hit, so that the time distribution of spallation neutrons is determined exclusively from the time distribution of driving particle pulse [8]. The energy of neutrons released from both sources is in the order of MeV whereas the interatomic distances and elementary excitations fall in the meV range. Thus the fast neutrons should be moderated using moderator substance. The moderator should be such that it gives highest possible flux of required energy in the shortest possible time (in pulsed sources) or in the largest possible volume (in continuous sources) [8].The moderation can be achieved by using moderators made of light atoms such as H_2O or D_2O. The time for slowing down the neutrons is of the order of 10^{-6} s after which the neutrons are in thermal equilibrium with the moderator. For a moderator at temperature T, the flux of neutrons is given by the Maxwellian distribution [8] $\Phi(\lambda) = \frac{1}{\lambda^3}\exp(-\frac{h}{2k_BTm\lambda^2})$. At room temperature the flux is maximum for neutrons with wavelength of about 1 Å. For other wavelengths the flux is maximized either by heating or cooling the moderator.

All the unpolarized neutron scattering experiments included in this work were performed using constant wavelength triple axis spectrometers either at Oakridge National Laboratory (HB1-A and HB1) or at Canadian Neutron Beam Center (CNBC) (N-5 and C-5). Figure 3.6.7 shows a schematic for typical triple-axis spectrometer.

The triple-axis refers to 3 independent axis of rotation of monochromator, sample and the analyzer. A polychromatic beam of neutrons from the reactor source is incident on a monochromator crystal. The choice of monochromator crystal depends upon the energy and wavelength that we want to use in the experiment. For energies below 35meV, generally (002) reflection (*d=3.35A*) of highly oriented pyrolytic graphite (HOPG) is used, because, for this energy range, the flux is maximized with this crystal. But at higher energies, the energy resolution of *PG002* crystal becomes worse and different crystals like *Be002, Be110, Cu220* are used. Even after reflection from monochromator crystal, the neutron beam is not truly monochromatic but contains higher harmonics with wavelengths λ/2, λ/4 ……,depending on the spacegroup symmetry of the monochromating crystal.To get rid of these higher harmonics, filters are used which allow neutrons with wavelength $\lambda \pm d\lambda$ (with $d\lambda < \lambda/2$) to transmit easily while the higher harmonic neutrons are scattered out of the beam by Bragg reflection. Generally a *PG002* filter is used with its *c* axis along the direction of neutron beam. After the neutrons are filtered out, they are collimated before they hit the sample to make sure that they hit the sample with same energy/angle. The sample itself can be rotated independently so that its different scattering planes satisfy Bragg condition with the same incident wavelength. The scattered beam from the sample is further filtered and collimated before it hits the analyzer crystal. The analyzer crystal can be rotated independently so that it scatters neutrons of some fixed energy and momentum toward the detector. Finally, the detector counts the number of neutrons within a given solid angle as function of energy and momentum transfer.

The polarized neutron experiment included in this thesis was carried out on the BT-7 triple axis spectrometer at NIST. There are different ways of polarizing neutrons like use of polarizing crystals or polarizing mirror or polarizing filters. Out of them, we used He^3 polarizing filter to define the polarization of both the incoming and outgoing neutrons. First He^3 gas is spin polarized by pumping with the Rubidium vapor and kept in a cell in the path of the unpolarized neutron beam. This spin polarized He^3 gas has very large capture cross section for neutrons with opposite spin but almost zero capture cross section for neutrons with parallel spin. Thus the neutron coming out of the He^3 cell is spin polarized with its spin parallel to spins of He^3 molecules. These polarized neutrons are then oriented along certain direction by using an adiabatically varying magnetic field. In our experiments, we applied the guide magnetic field such that the neutron spin is either along the scattering vector or perpendicular to the scattering vector.

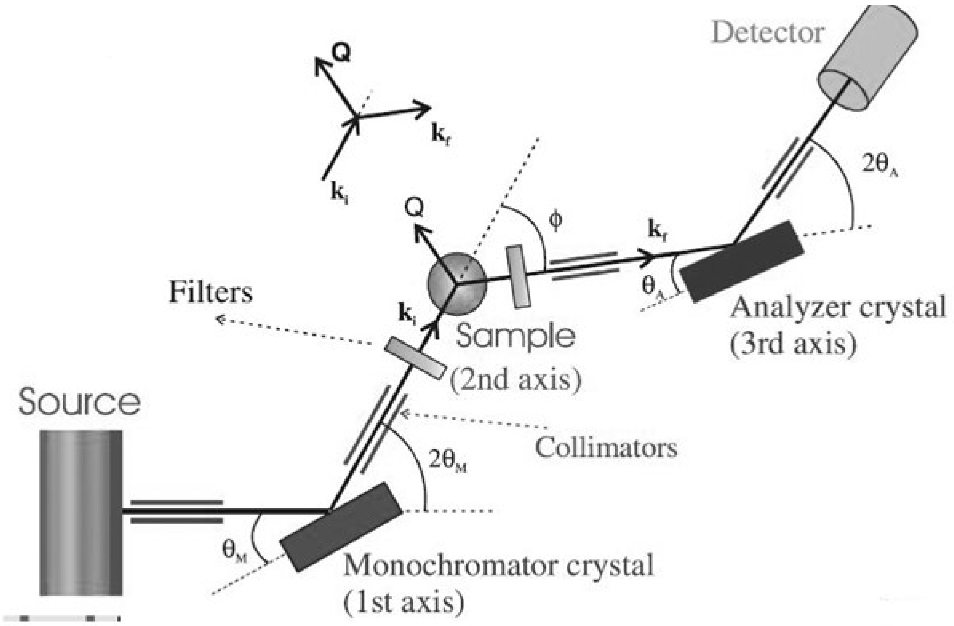

Fig. 3.6.1 Schematic of triple axis spectrometer [10]

Chapter 3 References

[1] C. Kittel and P. McEuen, *Introduction to solid state physics* (Wiley New York, 1996), 7.

[2] B. R. Pamplin, *Crystal growth* (Pergamon Press, 1980), 16.

[3] C. Dhital, S. Khadka, Z. Yamani, C. de la Cruz, T. Hogan, S. Disseler, M. Pokharel, K. Lukas, W. Tian, and C. Opeil, Physical Review B **86**, 100401 (2012).

[4] N. Ashcroft and N. Mermin, Holt-Saunders, Philadelphia **16** (1976).

[5] J. Goldstein, D. E. Newbury, D. C. Joy, C. E. Lyman, P. Echlin, E. Lifshin, L. Sawyer, and J. R. Michael, *Scanning electron microscopy and X-ray microanalysis* (Springer, 2003).

[6] J. Clarke and A. I. Braginski, (2004).

[7] C. Duval, *Inorganic thermogravimetric analysis* (Houston, Elsevier Pub. Co, Amsterdam, 1953).

[8] A. Furrer, J. Mesot, T. Strässle, and J. Mesot, *Neutron scattering in condensed matter physics* (World Scientific Singapore, 2009).

[9] A. Krása, .

[10] Z. Yamani, Z. Tun, and D. Ryan, Can. J. Phys. **88**, 771 (2010).

[11] http://squid.iitd.ernet.in/Basic_Literature.htm

Chapter 4: Correlated Phase Behavior of Sr_2IrO_4

(In this chapter I am going to present magnetic and crystal structure analysis of single layer compound Sr_2IrO_4 using neutron diffraction. Most of the work described in this chapter is published in an article by Dhital et.al "Neutron scattering study of correlated phase behavior in Sr_2IrO_4" Phys. Rev. B 87, 144405 (2013). After or in parallel to this study there are similar/different studies exploring the crystal and magnetic structure of this compound which I already discussed in Chapter 2 (Introduction)).

4.1 Motivation

Within the Ruddelsden-Popper series, a picture of a $J_{\mathrm{eff}} = ½$ Mott insulating phase has been proposed to explain the antiferromagnetically ordered, insulating ground states of its two members $n = 1$ (Sr_2IrO_4) and $n = 2$ ($Sr_3Ir_2O_7$) [1--3]. Within this picture, a cooperative interplay of spin-orbit-induced band-width narrowing and on-site Coulomb interactions generates the necessary Mott insulating ground state. An alternate interpretation, however, has also been proposed that, instead, models the insulating ground states of these systems as arising from a weakly correlated band insulator in which the formation of magnetic order continuously builds the band gap and where the effects of electron-electron correlations are secondary [4,5]. The insulating ground state in the $Sr_{2n+1}Ir_nO_{3n+1}$ series is destabilized as the dimensionality is increased with increasing n [6] however, the relative changes in the electronic and magnetic properties as the materials transition from the $n = 1$ single-layer Sr_2IrO_4 (Sr-214) to the $n = 2$ bilayer $Sr_3Ir_2O_7$ (Sr-327) remain poorly understood. The room-temperature resistivity of Sr-214 and Sr-327 reflect the notion of a reduced electronic band gap with increased dimensionality [7,8] however, their low-temperature properties differ substantially [7,9]. While charge transport in Sr-214 does not directly couple to the onset of magnetic order, Arrhenius-activated transport appears below 230 K, which then transitions to a variable range-hopping regime at low temperatures

[10]. In contrast to this, no simple model for the low-temperature transport applies [9,11] to transport of Sr-327. However, the resistivity couples to the onset of antiferromagnetic (AF) order below 280 K via an enhanced spin-charge coupling mechanism, and a proposed second phase transition appears below T^* =70 K [9,11].

While both systems are canted G-type antiferromagnets [3,9,12] the moments in Sr-214 orient within the basal plane, whereas those for Sr-327 orient predominantly along the *c* axis. The driving force behind this reorientation stems from the enhanced inter plane coupling of the bilayer compound; however, the evolution of the effective ordered moment and magnetism as a function of increasing dimensionality remains largely unexplored. Historical comparisons in the literature rely on saturated net moments as observed via bulk magnetization [7,11,13,14]. This is very imprecise given that these materials are canted antiferromagnets with entirely different moment orientations and hence vastly different pictures of ferromagnetic moments generated via in-plane canting. Given that the relative ordered moment size constitutes one traditional metric for ascertaining the relative strength of correlations between two materials in similar electronic environments, a precise determination of the relative values of their ordered moments is particularly germane.

4.2 Crystal Growth and Preliminary Characterization

For our experiments, we grew single crystals of Sr_2IrO_4 using established $SrCl_2$-flux techniques [3]. The stoichiometry of the resulting Sr-214 crystals was confirmed via energy dispersive spectroscopy measurements, and a number of Sr-214 crystals were also ground into a powder and checked via x-ray diffraction in a Bruker D2 phaser system. Within resolution, all x-ray peaks were indexed to the reported tetragonal structure (space group *I*41*/acd*, $a = b = 5.48$ A°, and $c = 25.8$ A°). For this sample we focused our study only on the determination of spin structure and the ordered moment using neutron scattering.

4.3 Neutron Scattering of Sr_2IrO_4 Single Crystal

Neutron diffraction experiments were performed on a 5-mg crystal with a resolution-limited mosaic of 0.40° at the C-5 triple-axis spectrometer at the Canadian Neutron Beam Center at Chalk River Laboratories. A fixed final energy E_F =14.5 meV setup was used with a vertically focusing pyrolytic graphite (PG) crystal (PG-002) as the monochromator and a flat PG-002 analyzer. Collimations were 33’, 48’, 51’, and 144’ before the monochromator, sample, analyzer, and detector, respectively, along with two PG filters after the sample. The single crystal was mounted within the [H, 0, L] scattering plane within a closed-cycle refrigerator**.**

Figure 4.3.1 shows the results of neutron scattering measurements through the magnetic wave vectors of Sr-214. Specifically, radial scans through the **Q** = (1*,* 0, L) positions show that for L = even, magnetic reflections appear below 230 K; consistent with the known T_N of this system [7,15]. The correlated order is three-dimensional, with a minimum in-plane spin-spin correlation length of ξ_L= 130 ± 8 °A calculated using the relation $\xi_L = \sqrt{2ln(2)}w^{-1}$ (w is the Gaussian width of the peak in $Å^{-1}$).

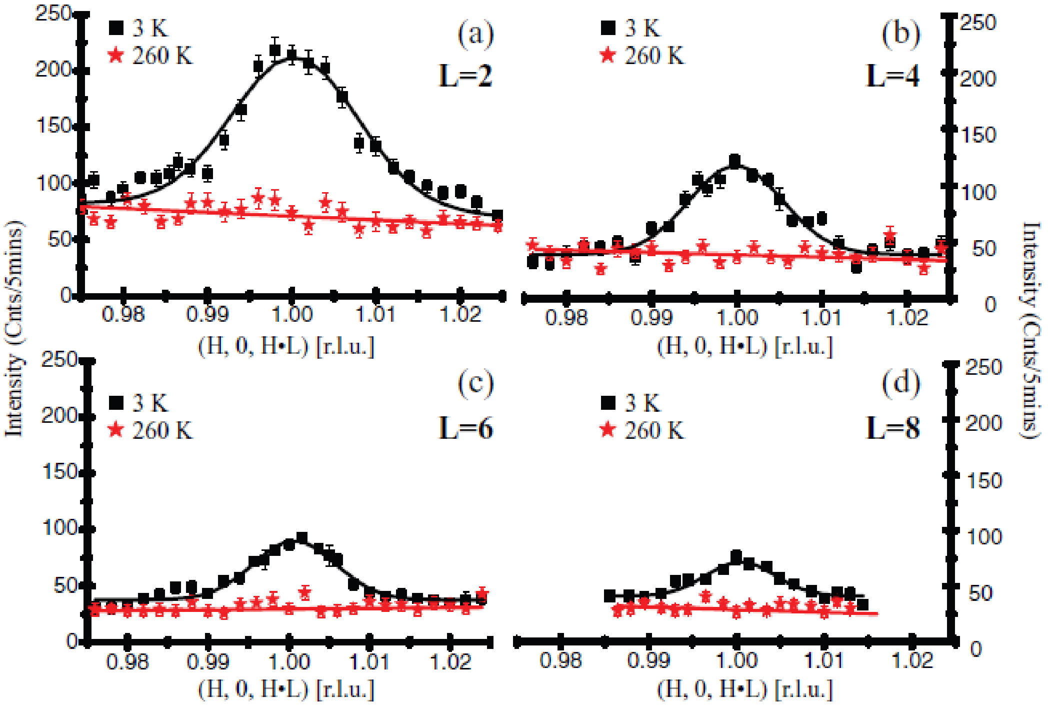

Figure 4.3.1 Radial *Q* scans both above and below T_N through magnetic Bragg peaks at (a) **Q** = (1,0,2), (b) **Q** = (1,0,4),(c) **Q** = (1,0,6), and (d) **Q** = (1,0,8) positions. Solid black lines are Gaussian fits to the data.

Given the magnetic structure determined via previous x-ray measurements [3] the appearance of both $L = 4N$ and $L = 4N + 2$ reflections in the same [*H, 0, L*] scattering plane implies the presence of two magnetic domains. As we argue later, the explanation for these domains is an inherent crystallographic twinning where both the [*1, 0, L*] and the [*0, 1, L*] structural domains are present within the same experimental scattering plane with moments pointed along a unique in-plane axis. Now turning to the radially integrated intensities of the (*1, 0, L*) magnetic peaks, the result of a simple model assuming the previously proposed spin structure of Sr-214 [3] [illustrated in Figure 4.3.2(c)] with two crystallographically twinned magnetic domains is overplotted with the experimentally observed intensities in Figure 4.3.2(a). This twin-domain model with equal domain populations agrees remarkably well with the observed neutron intensities, lending support to the assumption of an inherent orthorhombicity/twinning to the spin structure. The scale factor generated by using this model and normalizing to (00L)-type nuclear reflections gives an ordered moment of $\mu_{214} = 0.36 \pm 0.06\ \mu B$. As a direct comparison, if we normalize the moment of Sr-327 (chapter 4) from our earlier measurements [9] using the same procedure (i.e., the same Q positions) as the current Sr-214 study, the ordered moment for Sr-327 is a nearly identical $\mu_{327} = 0.35 \pm 0.06\ \mu B$.

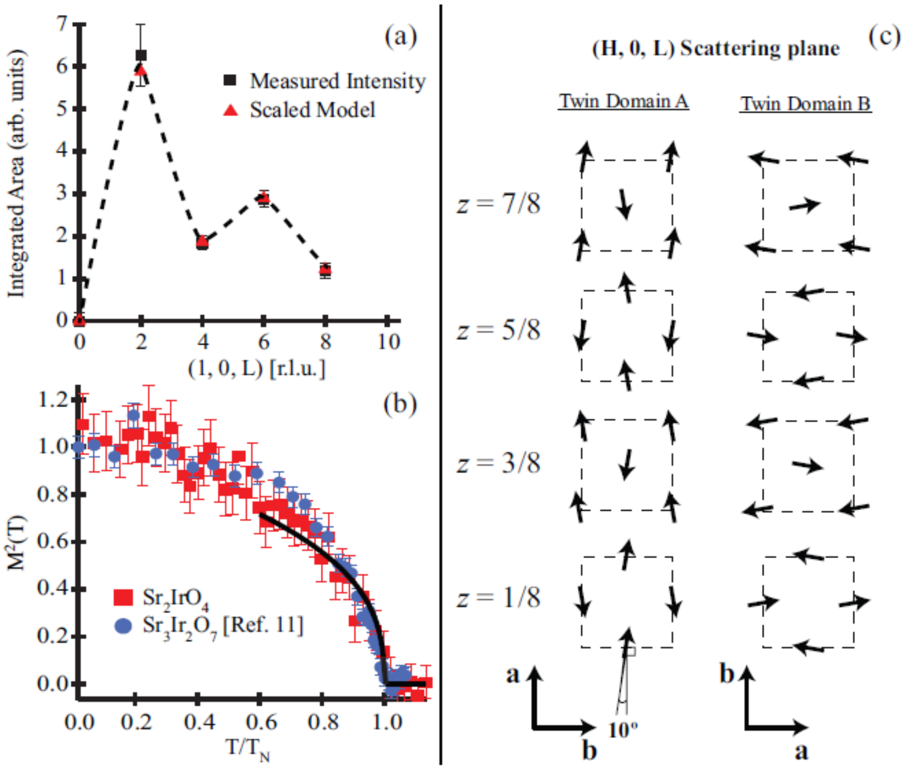

Figure 4.3.2 (a) radially integrated intensities [filled (black) squares] of magnetic Bragg peaks are plotted as a function of (1, 0, L). Expected intensities from the two-domain magnetic model discussed in the text are over plotted as filled (red) triangles. (b) Magnetic order parameters squared plotted as a function of reduced temperature for Sr-214 (squares) and Sr-327 (circles). (c) In plane projections of the model of canted AF order utilized in the calculation of the Sr-214 moment. Relative c-axis locations of each plane within the unit cell are denoted to the left of each corresponding plane.

Figure 4.3.2 (b) shows the magnetic order parameter squared M^2 (T/T_N) of Sr-214 is over plotted on the known M^2 (T/T_N) of Sr-327. Both order parameters track one another and power law fits of the form $M^2\ (T) = (1 - T/T_N)^{2\beta}$ over the range $0.6<$

$T/T_N < 1$ in each system yield an identical (within error) $\beta = 0.18 \pm 0.02$ for Sr-214 and $\beta = 0.20 \pm 0.02$ for Sr-327. This fact combined with the comparable moment sizes of each material suggests that each magnetic phase arises from similar interaction symmetries and correlation strengths, and more importantly, this reinforces that the bulk magnetization data showing a near-vanishing moment in Sr-327 [9,11] are simply a reflection of the *c*-axis orientation of the moments in this system (i.e., an orientation-based near-quenching of its net canted moment).

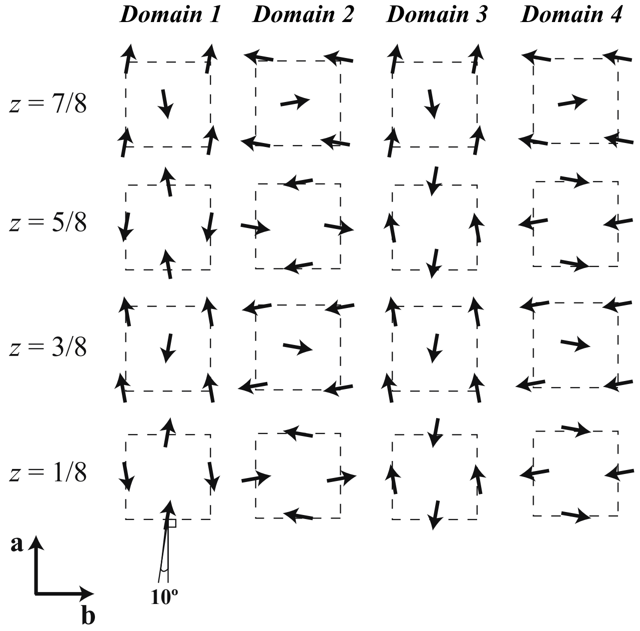
Four domains with "stacking fault" model of magnetic twinning

Figure 4.3.3 Two k-vector scenario showing possible magnetic domains in a twinning model assuming the tetragonal symmetry of the nuclear lattice and moments canted away from the in-plane lattice vectors. The difference between the two k-vectors is the relative stacking orientation of the z=1/8 and z=5/8 layer spins. Due to tetragonal symmetry, there are also necessarily domains with a-axis and b-axis oriented moments, leading to four domains model.

The model of twin magnetic domains (domains A and B) in Sr-214 generates magnetic reflections at $\mathbf{Q}_A = (1, 0, 4N)$ and $\mathbf{Q}_B = (0, 1, 4N + 2)$—apparent as $(1, 0, 4N + 2)$ in our data. Its agreement with the data can be seen via the double-peak structure in the intensities plotted in Figure 4.3.2 (a). Here the neutron's sensitivity to the moment direction via the $\boldsymbol{Q} \times \boldsymbol{\mu} \times \boldsymbol{Q}$ orientation factor in the scattering cross section generates an enhancement in the $(0,1,4N+2)$-type peaks in domain B due to the moments in that domain pointing out of the scattering plane. This suggests that the domain averaging one would expect from a four-domain picture [Figure 4.3.3], where moments can point along both *a* and *b* axes is not present and that, instead, moments lock to a unique, in-plane axis in a lower crystallographic setting than *I*41/*acd*. Figure 4.3.4 shows the comparison of two domain and four domain model. It is clear that two domain model best match with the experimental result [Figure 4.3.2 (a)].

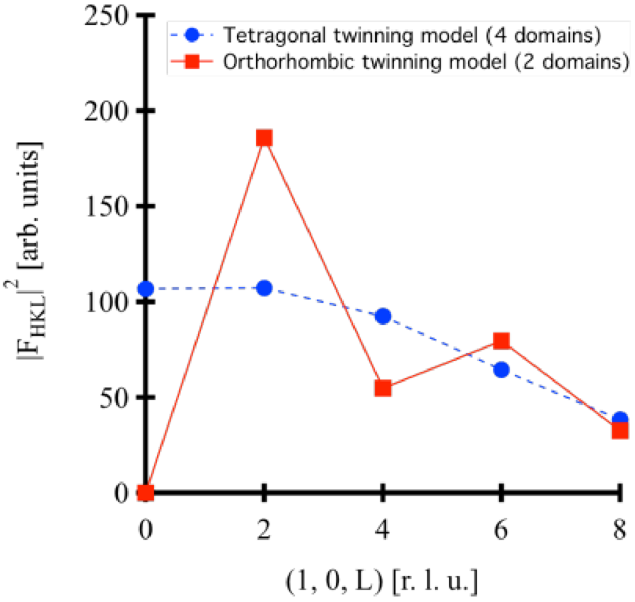

Figure 4.3.4 Comparison between the two domain orthorhombic twinning model [Figure 4.3.2] and the four domain two-vector model [Figure 4.3.3]. While the orthorhombic twinning model matches the data extremely well [Figure 4.3.2], the two-vector model qualitatively fails to match the data's intensity variation with increasing L. This demonstrates the inherent orthorhombicity of the lattice.

In order to further verify our twin magnetic domain picture, we performed polarized neutron scattering experiment in HB1 triple axis spectrometer in high flux isotope reactor. A Heusler monochromator ($CuMn_2Al$) was used to achieve the polarization and guide fields of 16 Gauss and 18 Gauss were applied along Horizontal and vertical directions respectively. The crystal was aligned in HOL scattering plane and cooled inside a cryostat. For this measurement we focused only on (102) magnetic peak. We measured four cross sections (i) Horizontal field (field along Q) non spin flip (HF-NSF) (ii) Horizontal field spin flip (HF-SF) (iii) Vertical field (field perpendicular to Q) non spin flip (VF-NSF) (ii) vertical field spin flip (VF-SF).

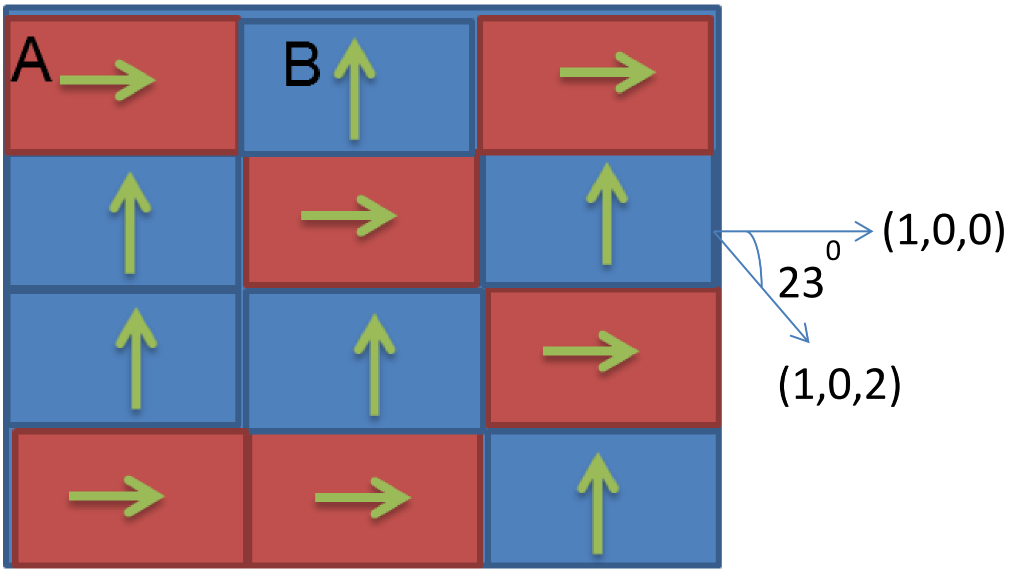

Figure 4.3.5 Simplified picture of two domain (A and B) models where the arrows represent the direction of moment as well as *a* axis for that domain. Here vector (1, 0, 2) is out of the plane making angle 23 degree with *a* axis

Now if the crystal having all these domains is aligned in the HOL scattering plane with horizontal scattering geometry then only one domain (domain A) lies in the scattering plane. With unpolarized neutrons, the magnetic scattering from domain A gives peak at (1, 0,4L) positions whereas that from domain B gives peak at (0,1,4L+2) position which we see as (1,0,4L+2). Thus the peak coming at position (1, 0 4L+2) is coming only from domain B. Note here that Q=(1,0,2) makes an angle of 23 degree with *a* axis i.e with direction of moment in domain A. However the domain giving intensity at (1,0,2) position (domain B) is always perpendicular to (1,0,2) direction. Now if a beam of neutron with its spin polarized along horizontal direction (i.e along Q= (1, 0, 2)) hits the sample then one should get the intensity only in the spin flip channel which comes from the domain B. If the neutron with vertical polarization i.e along the direction of B (at angle of 230 with B but perpendicular to Q=(1,02). Since neutron spin is already perpendicular to Q, one should get non-spin flip scattering from domain B. The result of our polarized experiment is shown in Figure 4.3.6.

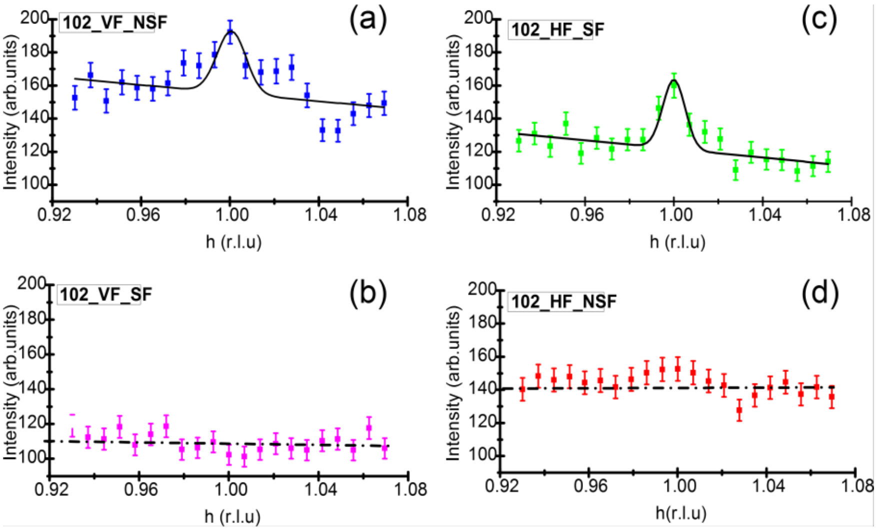

Figure 4.3.6 Four different cross sections for polarized experiment with at (1, 0, 2) magnetic Bragg peak. (a) Vertical field non spin flip (b) vertical field spin flip (c) horizontal field spin flip (d) horizontal field non spin flip.

The almost equal intensities of 102_VF_NSF and 102_HF_SF scattering indicate that our assumption of twin magnetic domain is correct.

Supporting the notion of lower structural symmetry, our neutron scattering measurements also reveal the presence of weak superlattice reflections which violate the nominally tetragonal *I*41*/acd* space group [15]. Figure 4.3.7 shows the results of radial scans through a series of (1, 0, L = odd) positions forbidden by the *I*41*/acd* space group. The intensity of these superlattice peaks continues to decrease with increasing temperature, indicating the presence of a higher temperature lattice distortion similar to the case of Sr-327 [9]. While the precise onset temperature of this distortion is unclear, at a minimum, the presence of these forbidden peaks implies a structural symmetry lower than that commonly reported and suggests the notion of magnetic domains arising via crystallographic twinning. A simple survey of likely orthorhombic subgroups of $I41/acd$ suggests the candidate space groups of $I2_12_12_1$ or $Pnn2$; however, several tetragonal subgroups are also consistent with these reflections. Further experiments are clearly required to fully understand the final lattice symmetry and to ultimately discern the role of potential oxygen vacancy/defects in the resulting structure and symmetry breaking. Same superlattice peaks were also seen in parallel study by Feng Ye et.al [16]

As a further check of magnetic order in Sr-214, we searched for the presence of (0, 0, L) peaks arising from the correlated in-plane canting sequence modulated along the *c* axis. *Q* scans in Figure 4.3.8 through the magnetic peak position **Q** = (0, 0, 3) show the presence of two components of scattering along *L*. The first is a weak magnetic peak centered at (0, 0, 3) due to the *c*-axis modulated in-plane canting orientations in Sr-214. The second component, however, is a broad short-range scattering signal that is uncorrelated along *L* and short-range along *H*. The in-plane correlation length of this underlying broad line shape is only $\xi_L = 4 \pm 1$ A° , reflective of in-plane correlations spanning the length of one unit cell and completely disordered out of the IrO_2 plane.

The intensity of this diffuse rod of scattering drops rapidly with increasing *L* as shown in Figure 4.3.8 (a). Here the background at **Q** = (0.6, 0, L) has been subtracted from the diffuse signal, and the signal vanishing is demonstrated explicitly by *H* scans at increasing *L* values plotted in Figure 4.3.6 (b). Furthermore, an extended *H* scan at the noninteger **Q** = (0, 0, 3.3) position [Figure 4.3.8(b)] shows that the diffuse rod of scattering only extends from the $H = 0$ position and is absent at the next allowed nuclear zone center at $H = 2$. This type of rapid drop in intensity curiously tracks the naive expectation of the isotropic Ir^{4+} form factor; however, the scattering remains only weakly temperature dependent. The precise origin of this short-range scattering is presently unclear; however, it likely reflects local disorder in the in-plane rotations of the oxygen octahedra. The larger relative spectral weight of the diffuse component and the absence of appreciable temperature dependence suggest a structural origin.

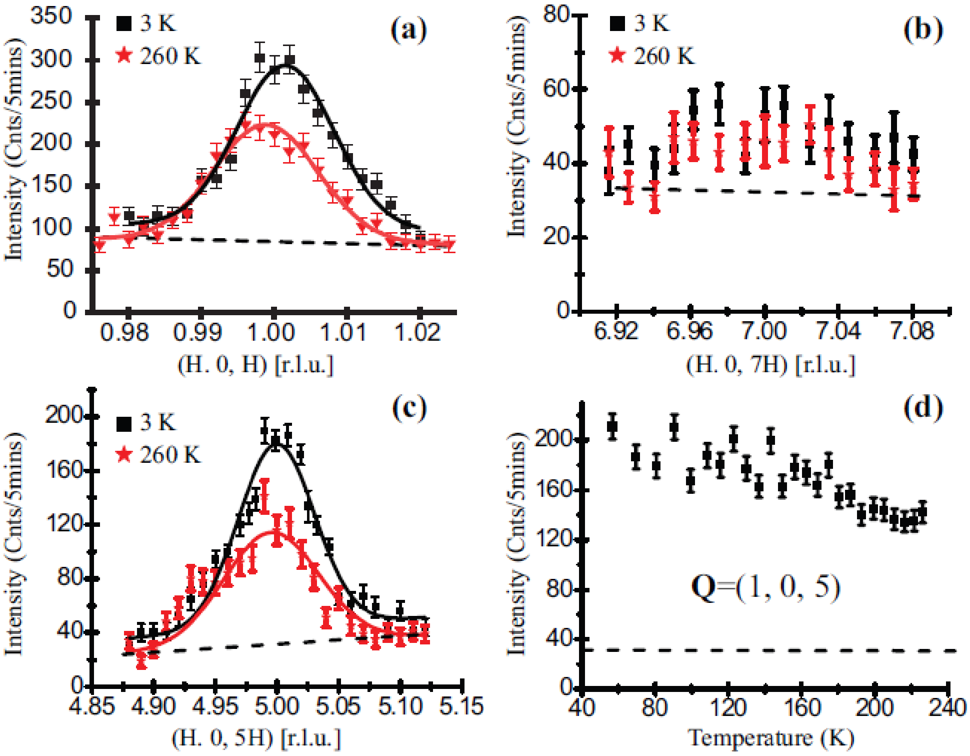

Figure 4.3.7 Radial scans at 3 and 260 K through potential nuclear superlattice peaks violating the *I*41/*acd* space group at (a) **Q** = (1,0,1), (b) **Q** = (1,0,5), and (c) **Q** = (1,0,7). (d) Intensity of the (1, 0, 5) superlattice peak as a function of temperature. The dashed line shows the background level for the (1, 0, 5) peak.

Given the rather delicate pattern of out-of-plane rotations of oxygen octahedra comprising the chemical unit cell within the *I*41/*acd* space group, some degree of local oxygen disorder is likely present, and hints of a similar diffuse component in the nuclear scattering profile were reported by the original polycrystalline refinements of Crawford *et al.* [15]. The degree of oxygen disorder may vary between samples and ultimately account for the variability observed in the transport properties in single crystals of this Sr 214 system [7,17].

4.4 Discussion and Conclusion

Structural scattering violating the *I*41/*acd* space group combined with the twinning observed in the magnetism of this material demonstrates a lower structural symmetry for Sr-214. At present, a full neutron-scattering-based single crystal refinement sensitive to the oxygen distortions has not been performed; however, the temperature evolution of this order parameter, at a minimum, demonstrates the presence of an additional structural order parameter in the ground state of this material, similar to the case of Sr-327 [9].This higher temperature structural distortion likely plays a role in the formation of the electronic gap known to be present above T_N in this material [6]. Due to the remaining uncertainty in the crystal structure, a full representational analysis of the magnetic basis vectors allowed within each irreducible representation of the magnetic phase is not currently possible. Despite this limitation, however, the absolute ordered moment can still be determined and the presence of magnetic domains can be leveraged to gain insight into the magnetic system.

First, the total moment we determine agrees within error with the bounds reported in a recently reported powder diffraction measurement [18] with $\mu_{\text{polycrystal}} = 0.29 \pm 0.04\ \mu_B$; albeit the moment determined in our single-crystal measurement is near the upper bound of the moment derived from the polycrystalline measurement of Lovesey *et al.* Our finding that the ordered AF moment of Sr-214 is $\mu_{214} = 0.36 \pm 0.06$

μB is also empirically consistent with the known saturated ferromagnetic moment of $M_{\text{bulk}} \approx 0.075\ \mu B$ that arises from the in-plane canting of all Sr-214 layers.

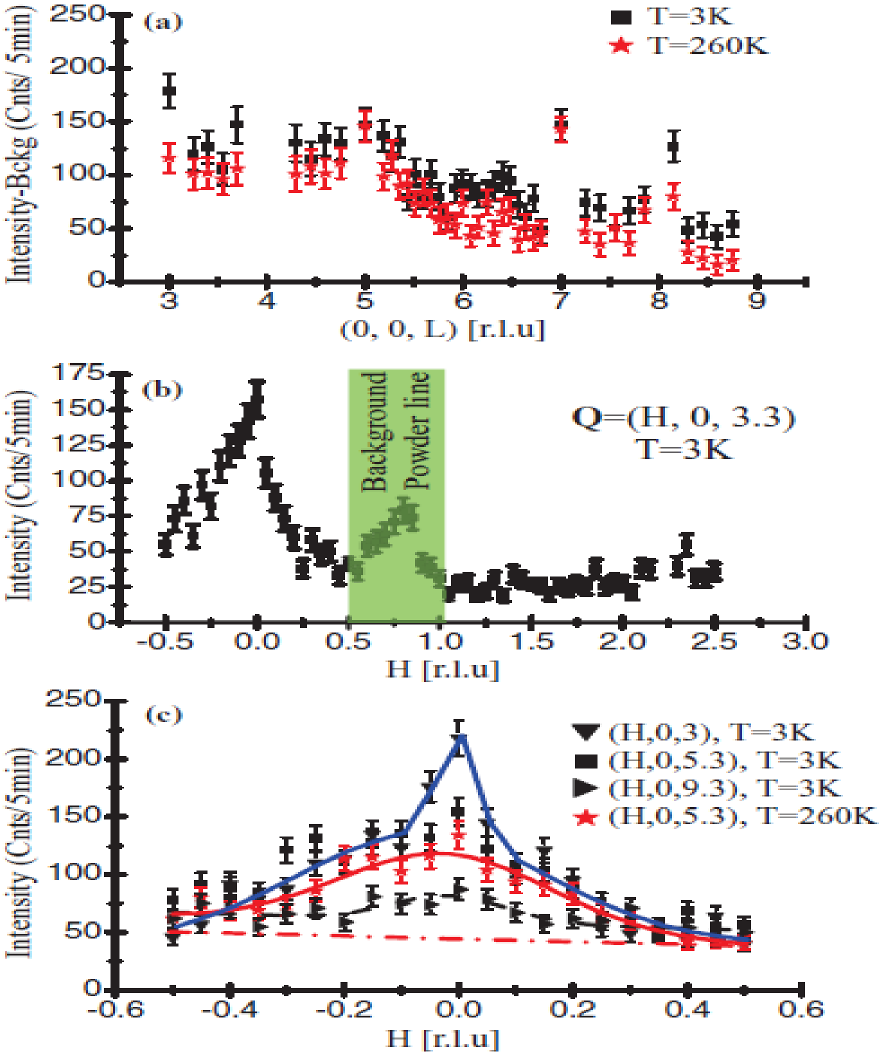

Figure 4.3.8 (a) Q scan along the $(0,0,L)$ direction showing a diffuse rod of scattering at both 3 and 260 K. Peaks at (0,0,4) and (0,0,8) are primary Bragg peaks. (b) H scan through the (0, 0, 3.3) position. The shaded (green) box masks background powder scattering from the sample mount. (c) H scans through the L = 3, 5.3, and 9.3 positions. The dashed line denotes the fit background, and solid lines are Gaussian fits to the data. For the $(H, 0, 3)$ peak, two Gaussian line shapes were fit to the data.

Using the measured AF moment value and assuming a 10^0 basal-plane rotation of the oxygen octahedra, the expected canted ferromagnetic moment from our data is $M_{\text{bulk}} = 0.063\ \mu B$. This value, although slightly smaller, agrees within error with earlier reports; [7,19] however, subtle oxygen stoichiometry/disorder effects can also renormalize the AF moment, resulting in some sample dependence.

The moment determined in our study is also in agreement with early local density approximation theoretical estimates. The near-identical ordered moments of Sr-214 (μ_{214} =0.36 μB) and Sr-327 (μ_{327} =0.35 μB) reflect the comparable correlation strengths between the two systems. This result stands in stark contrast to recent RXS studies which claim a substantially smaller moment within Sr-327 relative to Sr-214 [14] .Neutron scattering, however, provides a more quantitative assessment of the ordered moment size relative to the second-order RXS process, where recent work has theorized that the RXS signal is potentially comprised of only the orbital component of the total angular momentum [20].The intensity variation of magnetic scattering at the (1,0,*L*) positions plotted in Figure 4.3.2(a) surprisingly suggests that, between magnetic domains, moments point along the same unique in-plane axis plus a small degree of canting. Our two-domain picture of domain formation is presently modeled as stemming from crystallographic twinning and we have assumed the same relative orientations between Ir-site spins in each domain. This two domain scenario also can be explained in terms of polarized data shown in Figure 4.3.6. If we maintain this assumption of fixed relative spin orientations in all domains and now consider a more general scenario with tetragonal symmetry, a four-domain picture with crystallographically twinned domains whose moments point along the *a* axis in two of the domains and along the *b* axis in the other two can be envisioned. However, due to the neutron orientation factor, in Sr-214 the domain averaged intensities generated at each magnetic reflection differ between these two pictures of domain creation—most notably through the absence of the (1,0,0) magnetic reflection and only the two-domain scenario with moments oriented along one unique in-plane direction matches the observed data in Figure 43.2(a). This further suggests the notion of an underlying orthorhombic structural symmetry or, alternatively, more exotic means of symmetry breaking that bias the in-plane moment orientation such as single-ion anisotropy effects or an in-plane electronic nematicity.

We note here that in our four-domain models of magnetism in this system, we assumed that the orientations of the in-plane moments can be uniformly rotated from a predominantly a-axis orientation to a b-axis orientation using basis vectors within a single irreducible representation of the magnetic order. This is *not* allowed using the irreducible representations resulting from the decomposition of the magnetic phase using the $I41/acd$ structural symmetry as shown by Lovesey *et al [18]*.

However, given that our present measurements show that the true crystal structure possesses a lower symmetry; such a uniform rotation does become possible in lower candidate symmetries. We also did consistency check of our two and four domain model using representational analysis. Table 4.4.1 shows the representational analysis using *I41/acd* structural symmetry. Using the second table setting (origin choice 2), the Ir moments sit on the 8a Wyckoff position in the zeroth unit cell and a magnetic propagation wave vector of k = (1, 1, 1) as shown by Lovesey et al [18]. This gives four Ir atoms at the (1/2, 1/4, 1/8), (0, 3/4, 1/8), (1/2, 3/4, 3/8), and (0, 1/4, 3/8) positions. Another four positions can be generated via the body centering vector lb=(1/2, 1/2, 1/2).Here, using the BasIreps program, the magnetic representation breaks down into four irreducible representations (IRs) where: $\Gamma mag = 2\Gamma 1 + 2\Gamma 2 + \Gamma 3 + \Gamma 4$. Within this decomposition $\Gamma 3$ and $\Gamma 4$ can be excluded since their basis vectors direct the moment orientation out of the IrO_2-plane in disagreement with experimental data. $\Gamma 1$ and $\Gamma 2$ both possess basis vectors with moments oriented within the plane, and a linear combination of basis vectors within $\Gamma 1$ can describe the data. As mentioned already, in using this decomposition a model of magnetic domains cannot naively rotate the moment direction 90 degrees to point predominantly from along the a-axis to along the b-axis. This would involve basis vectors from two distinct IRs to describe the domain structure.

Γ_1 $I4_1/acd$ $k=(1,1,1)$	Iridium site	(1/2, 1/4, 1/8)	(1/2, 3/4, 3/8)	(0, 3/4, 1/8)	(0, 1/4, 3/8)
	Basis vectors				
	β1	(1, 0, 0)	(1, 0, 0)	(0, -1, 0)	(0, 1, 0)
	β2	(0, 1, 0)	(0, -1, 0)	(-1, 0, 0)	(-1, 0, 0)
	β3	(0, -1, 0)	(0, 1, 0)	(-1, 0, 0)	(-1, 0, 0)
	β4	(1, 0, 0)	(1, 0, 0)	(0, 1, 0)	(0, -1, 0)

Γ_2 $I4_1/acd$ $k=(1,1,1)$	Iridium site	(1/2, 1/4, 1/8)	(1/2, 3/4, 3/8)	(0, 3/4, 1/8)	(0, 1/4, 3/8)
	Basis vectors				
	β1	(1, 0, 0)	(-1, 0, 0)	(0, -1, 0)	(0, -1, 0)
	β2	(0, 1, 0)	(0, 1, 0)	(-1, 0, 0)	(1, 0, 0)
	β3	(0, 1, 0)	(0, 1, 0)	(1, 0, 0)	(-1, 0, 0)
	β4	(-1, 0, 0)	(1, 0, 0)	(0, -1, 0)	(0, -1, 0)

Table 4.4.1 Basis vectors for relevant irreducible representations for generating moments along the IrO_2 planes for the symmetry group I4$_1$/acd (four domain model).

However, if we stress that the structural symmetry is in fact not I4$_1$/acd as evidenced by the forbidden peaks at (1, 0, L=odd) positions and imagine that the structure however still remains tetragonal, the highest symmetry subgroup consistent with observed scattering is I41/a. We can again perform a similar decomposition of the magnetic structure using this modified space group with I41/a (origin choice 2) propagation vector k=(1,1,1) and Ir-atoms located at the 8e Wyckoff positions. In this setting the magnetic representation decomposes into two IRs: $\Gamma mag = 4\,\Gamma 1 + 2\,\Gamma 2$. Now, all basis vectors with moments within the ab-plane are contained within the same IR with the basis vectors shown in Table 4.4.2.

Γ_1 $I4_1/a$ $k=(1,1,1)$	Iridium site	(1/2, 1/4, 1/8)	(1/2, 3/4, 3/8)	(0, 1/4, 3/8)	(1/2, 1/4, 5/8)
	Basis vectors				
	β1	(1, 0, 0)	(0, 1, 0)	(0, 0, 0)	(0, 0, 0)
	β2	(0, 1, 0)	(-1, 0, 0)	(0, 0, 0)	(0, 0, 0)
	β3	(0, 0, 0)	(0, 0, 0)	(-1, 0, 0)	(0, -1, 0)
	β4	(0, 0, 0)	(0, 0, 0)	(0, -1, 0)	(1, 0, 0)
	β5	(0, 0, 0)	(0, 0, 0)	(-1, 0, 0)	(0, 1, 0)
	β6	(0, 0, 0)	(0, 0, 0)	(0, -1, 0)	(-1, 0, 0)
	β7	(1, 0, 0)	(0, -1, 0)	(0, 0, 0)	(0, 0, 0)
	β8	(0, 1, 0)	(1, 0, 0)	(0, 0, 0)	(0, 0, 0)

Table 4.4.2 Basis vectors for irreducible representations for generating moments along IrO_2 planes for symmetry group I4$_1$/a (two domain model).

In this lower symmetry tetragonal scenario, the spin structures within the four-domain picture modeled above (Figure 4.3.3) can all be described by basis vectors within the same IR. This demonstrates the legitimacy of our model of magnetic domains in a tetragonal picture where moments can be uniformly rotated to point predominantly along the a-axis to predominantly along the b-axis.

To summarize, our results demonstrate that the ordered magnetic moment in Sr-214 is identical to that observed in its bilayer Ruddelsden- Popper analog, Sr-327. Scattering from forbidden nuclear reflections and the presence of magnetic twin domains suggest an intrinsic orthorhombicity to the spin structure where oxygen distortions break the *I*41*/acd* symmetry and evolve as a function of temperature. Our results demonstrate that, aside from the ordered moment direction, the magnetic and structural phase behaviors in Sr-214 and Sr-327 parallel one another and suggest that correlation physics likely plays a similar role in each material's respective ground state.

Chapter 4 References

[1] B. Kim, H. Jin, S. Moon, J. Kim, B. Park, C. Leem, J. Yu, T. Noh, C. Kim, and S. Oh, Phys. Rev. Lett. **101**, 076402 (2008).

[2] J. P. Clancy, N. Chen, C. Y. Kim, W. F. Chen, K. W. Plumb, B. C. Jeon, T. W. Noh, and Y. Kim, Physical Review B **86** (2012).

[3] B. Kim, H. Ohsumi, T. Komesu, S. Sakai, T. Morita, H. Takagi, and T. Arima, Science **323**, 1329 (2009).

[4] R. Arita, J. Kunes, A. V. Kozhevnikov, A. G. Eguiluz, and M. Imada, Phys. Rev. Lett. **108** (2012).

[5] J. Carter and H. Kee, Physical Review B **87** (2013).

[6] S. Moon, H. Jin, K. W. Kim, W. Choi, Y. Lee, J. Yu, G. Cao, A. Sumi, H. Funakubo, and C. Bernhard, Phys. Rev. Lett. **101**, 226402 (2008).

[7] G. Cao, J. Bolivar, S. McCall, J. Crow, and R. Guertin, Physical Review B **57**, R11039 (1998).

[8] G. Cao, Y. Xin, C. S. Alexander, J. E. Crow, P. Schlottmann, M. K. Crawford, R. L. Harlow, and W. Marshall, Physical Review B **66** (2002).

[9] C. Dhital, S. Khadka, Z. Yamani*, et al*, Physical Review B **86** (2012).

[10] N. S. Kini, A. M. Strydom, H. S. Jeevan, C. Geibel, and S. Ramakrishnan, Journal of Physics-Condensed Matter **18**, 8205 (2006).

[11] G. Cao, Y. Xin, C. Alexander, J. Crow, P. Schlottmann, M. Crawford, R. Harlow, and W. Marshall, Physical Review B **66**, 214412 (2002).

[12] S. Fujiyama, H. Ohsumi, T. Komesu, J. Matsuno, B. J. Kim, M. Takata, T. Arima, and H. Takagi, Phys. Rev. Lett. **108** (2012).

[13] S. Boseggia, R. Springell, H. C. Walker, A. T. Boothroyd, D. Prabhakaran, D. Wermeille, L. Bouchenoire, S. P. Collins, and D. F. McMorrow, Physical Review B **85** (2012).

[14] S. Fujiyama, K. Ohashi, H. Ohsumi, K. Sugimoto, T. Takayama, T. Komesu, M. Takata, T. Arima, and H. Takagi, Physical Review B **86** (2012).

[15] M. K. Crawford, M. A. Subramanian, R. L. Harlow, J. A. Fernandezbaca, Z. R. Wang, and D. C. Johnston, Physical Review B **49**, 9198 (1994).

[16] F. Ye, S. Chi, B. C. Chakoumakos, J. A. Fernandez-Baca, T. Qi, and G. Cao, Physical Review B **87** (2013).

[17] O. B. Korneta, T. Qi, S. Chikara, S. Parkin, L. E. De Long, P. Schlottmann, and G. Cao, Physical Review B **82** (2010).

[18] S. W. Lovesey, D. D. Khalyavin, P. Manuel, L. C. Chapon, G. Cao, and T. F. Qi, Journal of Physics-Condensed Matter **24** (2012).

[19] B. J. Kim, H. Ohsumi, T. Komesu, S. Sakai, T. Morita, H. Takagi, and T. Arima, Science **323**, 1329 (2009).

[20] L. C. Chapon and S. W. Lovesey, Journal of Physics-Condensed Matter **23** (2011).

Chapter 5: Electronic and Magnetic Phase Behavior of $Sr_3Ir_2O_7$

(In this Chapter I am going to present our study on the electronic/spin behavior of bilayer parent compound $Sr_3Ir_2O_7$.Most of the work described in this chapter is published in an article by Dhital et al "Spin ordering and electronic texture in the bilayer iridate $Sr_3Ir_2O_7$" PHYSICAL REVIEW B86, 100401(R) (2012). After or in parallel to this work there are similar/different works exploring the electronic behavior of this compound which I already discussed in Chapter 2 (Introduction)).

5.1 Motivation

Recently, there has been considerable interest in studying the phase behavior of correlated 5*d*-electron transition metal oxides due to the potential of realizing electronic phenomena possible only when electron hopping, spin-orbit coupling, and Coulomb interaction energy scales are almost equivalent [1--4].Of particular focus has been members of the iridium oxide Ruddelsden-Popper (RP) [5] series $Sr_{n+1}Ir_nO_{3n+1}$, where an experimental picture of a spin-orbit induced $J_{\mathrm{eff}} = 1/2$ Mott insulating state has been proposed [6,7]. Upon increasing the dimensionality of the iridate RP series to higher n, optical [2] and transport measurements [8,9] have shown that the effective bandwidth increases and the system transitions from a quasi-two-dimensional insulating state to a metallic phase in the three-dimensional limit. Specifically, the reported optical gap in the $n = 2$ member $Sr_3Ir_2O_7$ (Sr-327) shifts considerably downward relative to the $n = 1$ Sr_2IrO_4 system into what should be a weakly insulating phase [2],demonstrating that Sr-327 occupies a unique position in the iridate RP phase diagram near the boundary of the metal to insulator phase transition in the RP series. Given this framework, $Sr_3Ir_2O_7$ exhibits a number of anomalous features in its magnetic properties: Bulk magnetization measurements of Sr-327 reveal a rich behavior possessing three distinct energy scales [9,10] and recent muon spin rotation (μSR) measurements have revealed the presence of highly disordered local spin behavior [11] both supporting the notion of multiple coexisting or competing magnetic phases. With these existing situations, I am going to present our study using neutron scattering, transport and magnetization techniques on this bilayer compound.

5.2 Crystal Growth and Preliminary Characterization

Crystals were grown using flux techniques in platinum crucibles using IrO_2 (99.98%, Alfa Aesar), $SrCO_3$ (99.99%, Alfa Aesar), and anhydrous $SrCl_2$ (99.5%, Alfa Aesar) in a 2:3:15 molar ratio. Starting powders were sealed inside the crucible with a Pt lid and further contained inside alumina crucibles to limit volatility. Mixtures were heated to 1300^0C, slowly cooled to 850^0 C at a rate of 3.5 C/hr, and then furnace cooled to room temperature. The resulting boule was etched with deionized water and black $Sr_3Ir_2O_7$ crystals with typical dimensions 2 mm x 2 mm x 0.1 mm were removed. The resulting Sr:Ir ratio was confirmed to be 3:2 via energy dispersive spectroscopy (EDS) measurements, and a number of Sr-327 crystals were also ground into a powder and checked via x-ray diffraction in Bruker D2 Phaser system. No coexisting Sr_2IrO_4 phase was observed and the resulting pattern was refined to the originally reported *I4/mmm* structure—we note, however, that, due to the small scattering signal from oxygen, we are unable to distinguish between this and the various reported orthorhombic symmetries. For the remainder of this thesis, we will index the unit cell using the pseudo tetragonal unit cell with $a = b = 5.50$ A˚, c = 20.86 A˚ .Figure 5.2.1 shows a typical crystal and powder pattern for $Sr_3Ir_2O_7$ refined using FullProf software package [12].

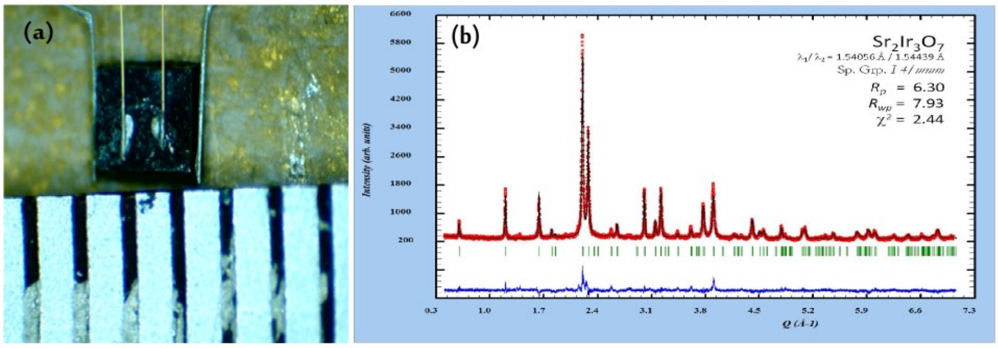

Figure 5.2.1 (a) A single piece of $Sr_3Ir_2O_7$ crystal (b) Powder pattern for $Sr_3Ir_2O_7$ crystals grounded together obtained using Bruker X-ray diffractometer [13].

5.3 Resistivity of $Sr_3Ir_2O_7$

Resistivity data for $Sr_3Ir_2O_7$ was collected in a series of four-wire setups: (1) Zero field resistance from 300 K to 12 K was collected with a Keithley 2182A voltmeter, (2) data from 12 to 0.3 K was collected in a He^3 absorption refrigerator with an Keithley Model 617 electrometer, and (3) magnetoresistance data was collected in a 9 T Quantum Design PPMS. Looking first at the results of our *ab*-plane transport measurements under low (1 μA) current, Figure 5.3.1 (a) shows the zero field resistivity as a function of temperature. The sample's resistivity increases from several mΩ cm at room temperature to beyond 10 MΩ cm below 20 K, and begins to show saturation behavior below 2 K. There is no substantial interval of constant activation energy, as illustrated by the overplot of $\partial \ln\rho/\partial(1/T)$ versus T in this same panel. Instead, $\partial \ln\rho/\partial(1/T)$ shows two peaks suggestive of two phase transitions coupling to charge carriers: the first near the known magnetic phase transition at T_{AF} = 280 K [9,13] and the second indicating a lower temperature phase formation at $T^* \approx$ 70 K.

In order to investigate further the transport properties of this lower temperature, T^* phase, the charge transport was characterized via a voltage driven I - V sweep at 300 mK shown in Figure 5.3.1 (b). A pronounced nonlinearity appears, where with increasing field strength the system switches from a linear, Ohmic regime with near zero conductance into highly non-Ohmic field enhanced conductivity (FEC) regime. To determine the temperature evolution of this FEC feature, a separate sample was mounted and probed with 600 μs current pulses to minimize heating effects [Figure 5.3.1 (c)]. While it is difficult to completely preclude all heating effects within the rise and sample time of the pulse, these pulsed measurements show that the nonlinear bend in the I -V curve persists and eventually vanishes below resolution at $T \approx 60$ K. A separate (rough) check for discriminating the nonlinear conduction from simple Joule heating can be performed by looking at the 30 K data in Figure 5.3.1 (c). The Ohmic regime R (30 K) = 42 kΩ and the maximum pulsed current (2 mA) during the 600 μs pulse delivers a maximum $\Delta Q = 10.1 \times 10^{-5}$ J. While low temperature heat capacity data are needed for Sr-327, as a lower estimate, the heat capacity of Sr_2IrO_4 at 30 K can be used (≈14 J/K) [14] giving a maximum $\Delta T = 5.5$ K (for a 1.32×10^{-6} mol sample). In carrying out a similar analysis for each current value pulsed at 30 K and assuming *perfect* thermal isolation, the measured Ohmic $R(T)$ can be used to determine the lowest fields possible due to pure Joule heating as a function of the pulsed current density. This limiting case is plotted as a dashed line in Figure 5.3.1 (c), demonstrating that the nonlinear feature at 30 K is intrinsic.

In looking at the magnetoresistance of the same sample plotted in the Figure 5.3.1 (d), the $MR = [R(9\ T) - R(0\ T)]/R(0\ T)$ ratio is negative and shows two minima at $T^* \approx 70$ K and $T_{AF} = 280$ K. The lower minimum appears approximately at the temperature where the onset of FEC emerges and coincides with the low-T peak in $\frac{\partial ln\rho}{\partial(1/T)}$. The origin of the negative magnetoresistance is likely the removal of spin disorder scattering due to biased magnetic domain populations and the inflection below T^* supports the idea of a field coupled order parameter freezing below 70 K. The suppression of enhanced fluctuations originating from an additional electronic instability, however, may also account for the overall negative MR.

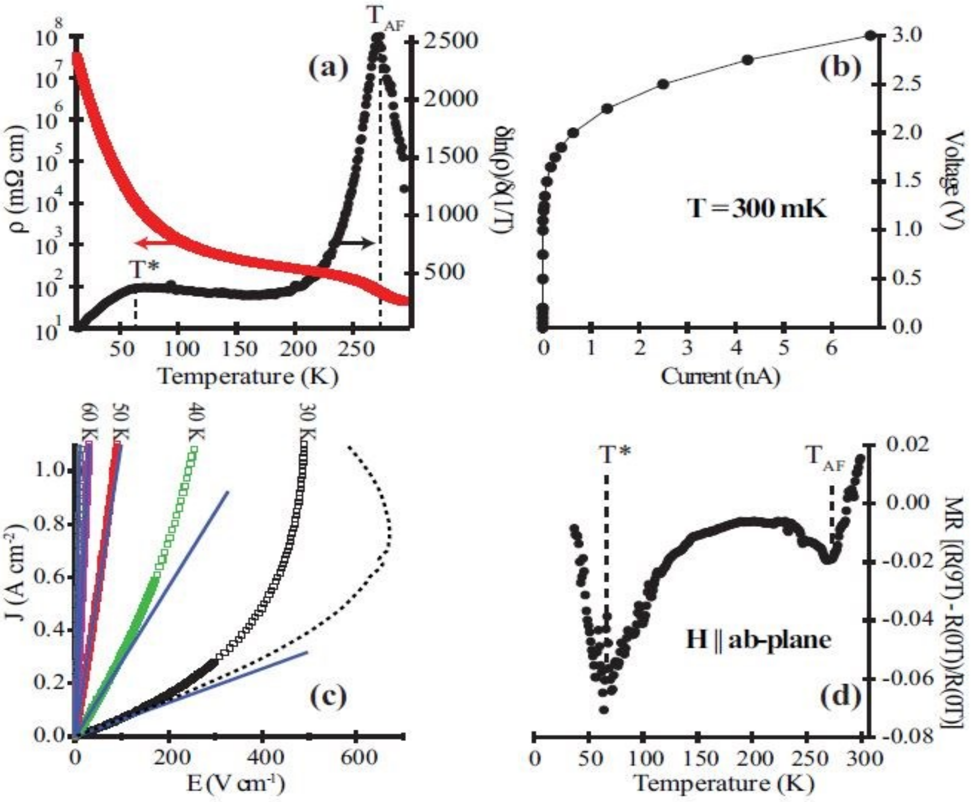

Figure 5.3.1 (a) Temperature dependence of the *ab* plane resistivity for Sr-327. Also plotted is the $\partial \ln \rho / \partial(1/T)$ vs T showing two peaks at T_{AF} and T^* . (b) *I-V* curve of *ab*-plane transport at 300 mK showing voltage biasing into a FEC regime. (c) Current driven, pulsed, *I -V* measurements as a function of temperature. Solid lines show linear fits to the Ohmic regime at each temperature. The dashed line is a Joule heating model at 30 K as described in the text. (d)Magnetoresistance (MR) ratio as described in the text plotted as a function of temperature showing two well defined minima at the T and T_{AF} transitions [13].

5.4 Magnetization of Sr$_3$Ir$_2$O$_7$

The magnetization measurement was carried out using Quantum design SQUID magnetometer and plotted in Figure 5.4.1(a). Magnetization data shown in Figure 5.4.1 (a) supports the idea of a bulk phase transition below 70 K where a downturn in the dc susceptibility originally reported by Cao *et al* [9] begins, suggestive of a glassy freezing process. Consistent with earlier reports [9,10], three energy scales are apparent in the field cooled magnetization data: a canted AF phase transition at T_{AF} =280 K, a sharp upturn at T_O = 220 K and an eventual decrease in susceptibility below T^*=70 K. Both field cooled (FC) and zero field cooled (ZFC) data show similar downturns near T^* and an irreversibility temperature near T_O. I also want to make a note that the feature at T_O = 220 K is not reproduced in every sample studied.

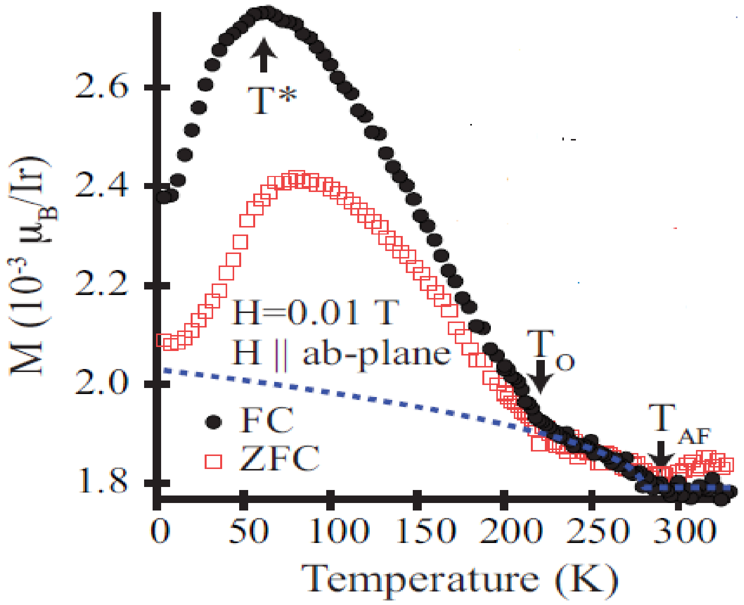

Figure 5.4.1 (a) dc-magnetization data for Sr-327 with H = 0.01 T aligned parallel to the *ab* plane for both FC (solid symbols) and ZFC temperature sweeps (open symbols). The dashed line shows the mean-field order parameter fit to the net moment from the 280 K transition. The inset shows M vs H sweep at 300K [13].

5.5 Neutron Scattering of $Sr_3Ir_2O_7$

As mentioned in the introduction (Chapter 2), neutron scattering is an ideal measurement for resolving spin structure and the superlattice peaks arising from Oxygen atom displacements. But in case of the iridium containing compounds, there was fear about the success of the experiment due to small size and strong neutron absorption of these crystals. But we manage to grow reasonable sized crystal sufficient for doing elastic neutron diffraction. We performed unpolarized neutron diffraction measurements on a 7 mg single crystal Sr-327 sample with the results plotted in Figure 5.5.1 and 5.5.2. As an starting point all three scattering planes: [*H*,0,*L*], [*H*,*K*,0], and [*H*,*H*,*L*] were explored and magnetic reflections were observed only at the (1,0,*L*) positions for *L* = 1,2,3,4,5,6,….The correlated order is three dimensional with $\xi_L = \sqrt{2}\ \ln(2) \times 1/w = 147 \pm 10$ A° ,where w(°A^{-1}) is the peak's Gaussian width [Figure 5.5.1(a)]. The appearance of both *L* = even and *L* = odd reflections in a simple collinear picture of the spin structure is therefore consistent with recent x-ray results resolving the presence of two magnetic domains [10] attributable to in-plane structural twinning in an orthorhombic symmetry[1]. Looking at the order parameters for both the *L* = 3 and *L* = 2 reflections in Figure 5.5.1 (f), the magnetic intensities show that the *L* = 2 peak disappears at T_{AF} while substantial intensity remains at 280 K in the *L* = 3 reflection. **Q** scans plotted in Figure 5.5.1(b) demonstrate this more explicitly. The peak remaining above 280 K is long-range ordered with a minimum correlation length of 93 ± 18 A°, comparable to the correlation length observed at 10 K (97 ± 5 A°). Due to the rather coarse collimations used, both these values and those of all magnetic Bragg reflections are resolution limited. At 300 K peaks remain at the (1, 0, *L*) *L* = 1, 3, 4 positions, all forbidden in the reported structural space groups to date. This same crystal was then loaded into a furnace and measured at higher temperatures, where, upon warming, the remnant peaks continue to decrease in intensity as illustrated in Figure 5.5.1(d); however, they notably remain present beyond 600 K. To confirm the presence of high temperature peak we performed rocking scan at different temperatures in different instrument which is plotted in Figure 5.5.1 (e). This verifies that the presence of superlattice peak

---

[1] The same group, however, reported twin domains but with moments pointing along c axis [15] in place of moment in ab plane which was described in reference [10]

at high temperature is reproducible. The persistent temperature dependence of these peaks beyond 300 K, and the absence of peaks at higher order L and H gave us a reason to doubt the possibility of its magnetic origin with additional order parameter. However, with polarized neutron diffraction we ruled out the possibility of high temperature magnetic phase which I will discuss in subsequent section.

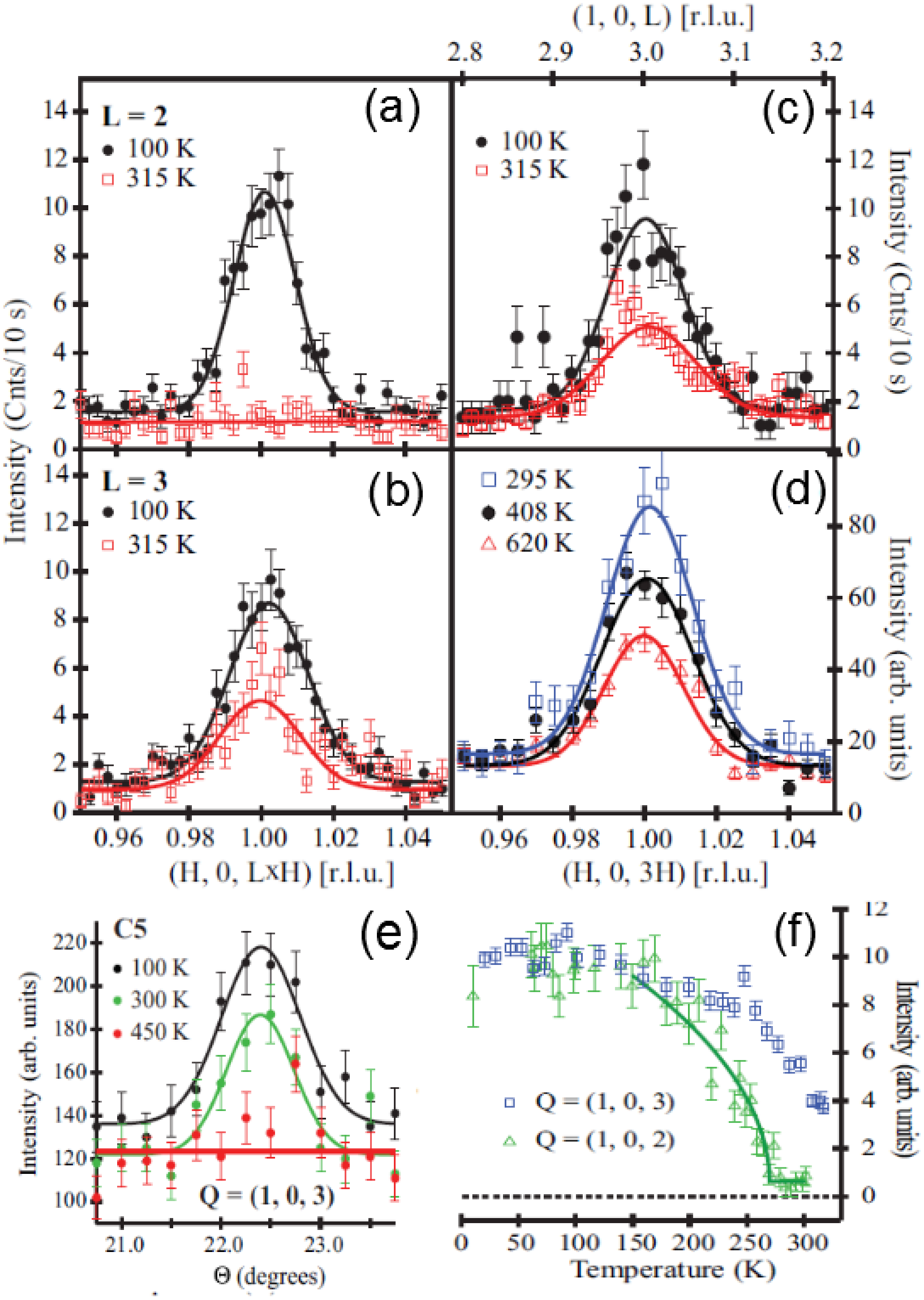

Figure 5.5.1 (a) Radial Q-scans at 100 K and 315 K through the (a) Q= (1, 0, 2) (b) and Q= (1, 0, 3) reflections. Solid lines are Gaussian fits to the data. (c) L-scans across the (1, 0, 3) point showing 3D AF at 100 K and 315 K. (d) Q-scans showing the temperature dependence of the (1, 0, 3) peak above 300 K (e) Rocking scans on a separate crystal showing the temperature dependence of the (1,0,3) peak above 300 K. (f) Temperature dependence of the peak intensities at (1,0,3) and (1,0,2) magnetic reflections. The solid line is a power law fit to the (1, 0, 2) order parameter [13].

Due to presence of (1 0 L=1, 2,3,4,5...) forbidden nuclear peaks but with different temperature dependence, we proceeded with two possibilities. (i) High temperature (T > 280 K) phase is non-magnetic or at least have different origin (ii) High temperature phase is also magnetic. In the first possibility, we subtracted the additional intensity at 315 K from 100 K data so that only the magnetic component survives. The observed intensity obtained from this subtraction is consistent with the expected magnetic intensity from twin domains of G-type AF structure [Figure 5.5.2 (a)] with moments pointing along *c* axis [Figure 5.5.2 (b)] consistent with similar studies using x-rays [15,16]. The ordered moment using this model is $\mu = 0.36 \pm 0.06\mu B$.[2]

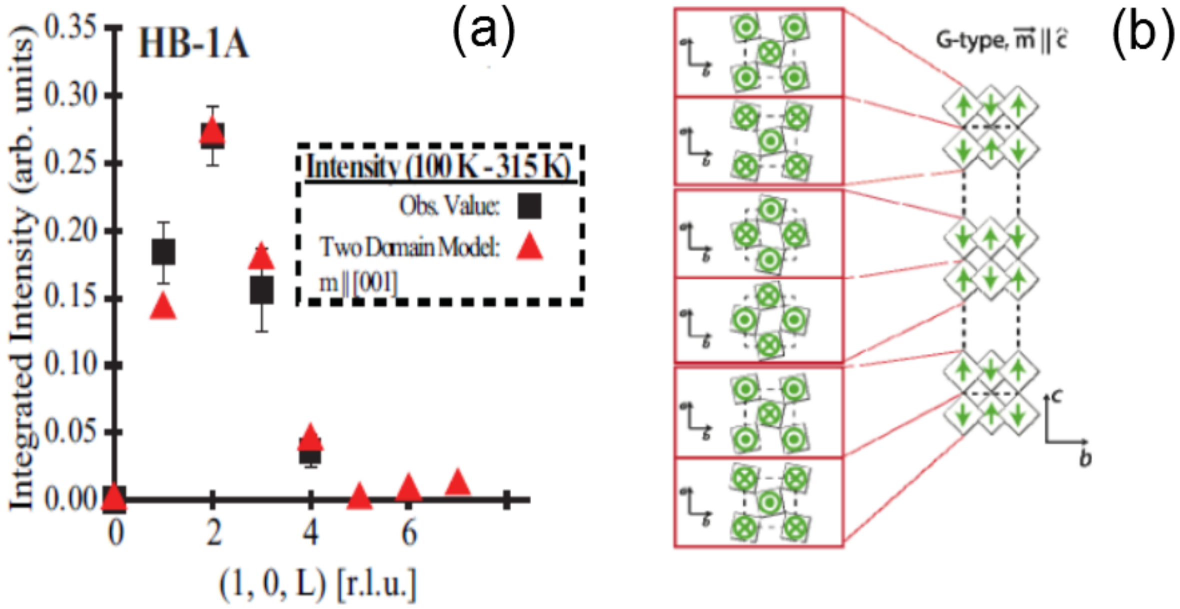

Figure 5.5.2 (a) Integrated intensities plotted at 100 K with 315 K data subtracted compared with corresponding calculated intensities (b) Projection of the G-type AF ordered spin structure in both the bc and ab planes for moments parallel to the c-axis. Dashed lines denote the orthorhombic unit cell and diamonds are projections of the oxygen octahedral coordinated around the magnetic Ir^{4+} ion [13].

---

[2] However I found that this moment value depends upon normalization procedure .

If we consider the second possibility and use the total integrated intensity at 100 K then the integrated intensity variation looks like in Figure 5.5.3 (b) (black square).If we again assume a twinned G-type aligned spin structure now with two magnetic domains, then a second domain added to the previous model [Figure 5.5.2 (b)] with moments directed along the (1, 0, 0) [Figure 5.5.3 (a)] axis roughly fits the data [Figure 5.5.3 (b)].

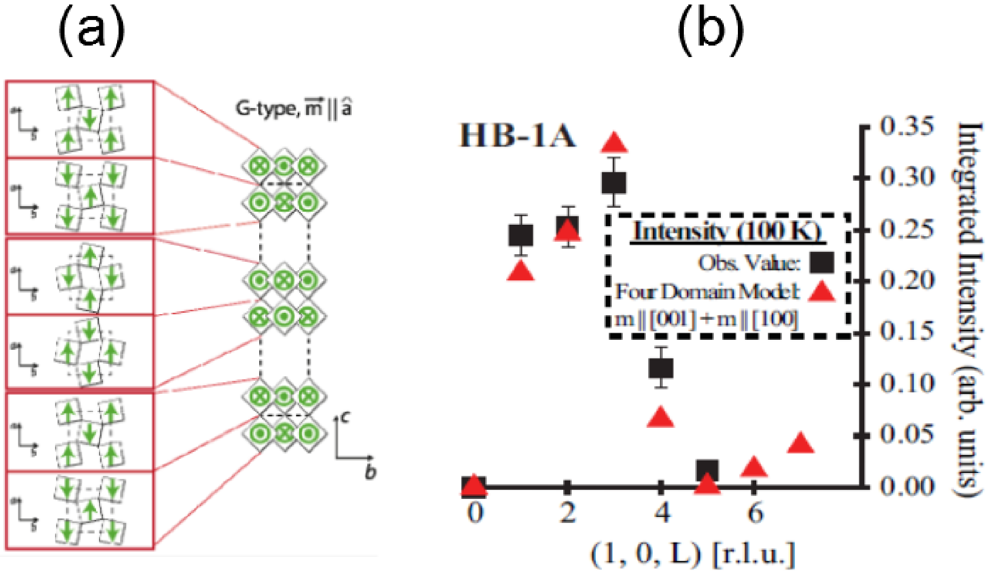

Figure 5.5.3 (a) Projection of the G-type AF ordered spin structure in both the *bc* and *ab* planes for moments parallel to the a-axis. Dashed lines denote the orthorhombic unit cell and diamonds are projections of the oxygen octahedral coordinated around the magnetic Ir^{4+} ion (b) the total integrated intensity at 100 K and compared with corresponding model [13].

However, as I mentioned before, we were not fully convinced with the magnetic behavior persisting above nominal T_{AF}, so we performed polarized neutron diffraction measurements with the results plotted in Figure 5.5.4. Radial scans through Q= (1,0,3) show that the (1, 0, L)-type superlattice reflections appear only in the non-spin-flip channel with the neutron guide field applied parallel to Q. This demonstrates the structural origin of the superlattice peak and mandates a space group symmetry lower than Bbcb. The high temperature (1, 0, L)-type peaks argue for oxygen octahedral tilting as well as in-plane rotation in this system. Such a tilt necessarily exists for the moments oriented along the *c*-axis in order to generate the net in-plane moment observed in bulk magnetization measurements, and the strong spin-lattice coupling in Ruddelsden Popper iridates naturally leads to an expectation of an accompanying structural tilt.

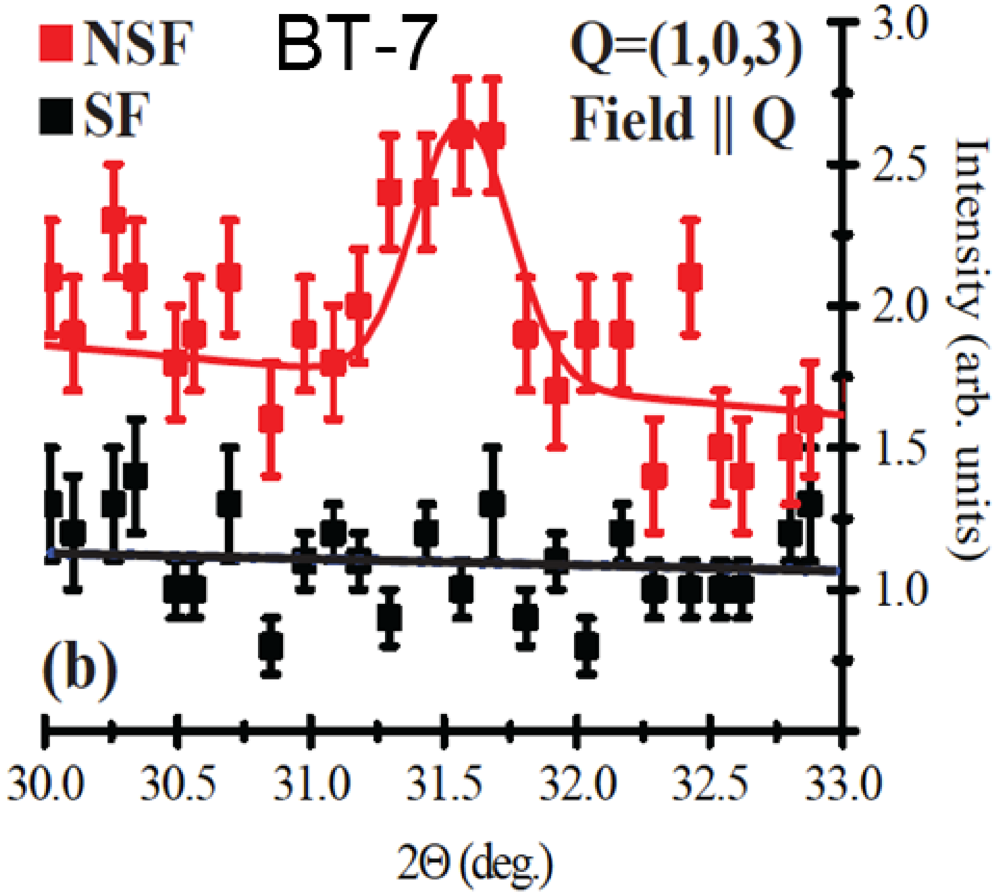

Figure 5.5.4 Polarized neutron diffraction measurements of $Sr_3Ir_2O_7$ showing radial scans through the **Q**= (1, 0, 3) superlattice peak at 300K in both spin-flip (SF) and non-spin-flip (NSF) channels. The magnetic guide field was applied parallel to the momentum transfer **Q**. Error bars represent one standard deviation.

5.6 Discussion and Conclusion

Our combined data demonstrate the presence of canted 3D antiferromagnetic domains whose phase evolution is decoupled within resolution from the fluctuation and freezing behavior at T^* and T_O, precluding any additional major spin reorientations at these temperatures. This suggests that there remain additional moments weakly coupling to fluctuations below T_O and eventually freezing below T^*.

Our measurements in their entirety therefore suggest a picture of three distinct order parameters driving the phase behavior of Sr-327: (1) a high temperature phase with $T_{\text{onset}} > 620$ K, (2) a canted AF magnetic transition at 280 K, followed by (3) the freezing of the T^* phase into an electronically textured ground state.

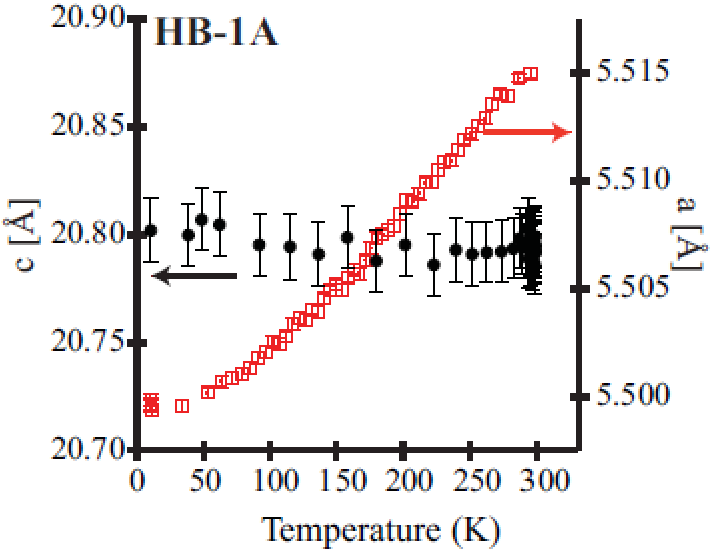

Figure 5.6.5 variation of *a* and *c* axis lattice parameters as function of temperature for $Sr_3Ir_2O_7$ [13].

The T^* transition is nominally suggestive of a charge density wave (CDW) or collective transport mechanism which becomes depinned above a threshold field, leading to an avalanche process in the carrier number. The structural lattice parameters [Figure 5.6.5], however, evolve smoothly as the system is cooled from 315 to 10 K and, to date, no structural distortion associated with a conventional CDW formation has been observed below 300 K [9] although, high temperature structural measurements are a promising avenue for future studies. An alternative scenario of exchange coupled metallic islands condensing below T^* with a substantial Coulomb barrier for tunneling may also address the transport mechanism below $T*$ [18,19].Similar non-Ohmic behavior has also been reported in other correlated iridates [20,21] suggesting an electronic inhomogeneity intrinsic to these 5*d*-correlated materials. Curiously x-ray measurements on a Sr-327 sample with a qualitatively similar bulk spin susceptibility have reported the onset of AF order at T_O [22].This resonant x-ray scattering (RXS) study speculated about the presence of short-range order setting in at T_{AF} and diverging at T_O as the reason for the discrepancy [10], however, our measurements reveal no appreciable change in the correlation length upon cooling through T_O. Given that more recent RXS measurements show the onset of magnetism at the expected T_{AF} = 285 K, variation in sample quality is likely the cause for the variance reported between these two RXS studies.

To summarize, our studies have illustrated a complex electronic ground state in the $Sr_3Ir_2O_7$ system with multiple electronic order parameters. Although our unpolarized experiment was not conclusive, the polarized experiment performed later indicated that the origin of high temperature peak above nominal T_{AF} is nonmagnetic. This indicates that the two domain model with G-type structure with moment along c axis is the correct model rather than four domain models. But still there may be some canting of that moment due to rotation of octahedra. Below T_{AF} =280 K, the system exhibits multiple magnetic domains or alternatively non-collinear spin order in its ground state. The spin order appears decoupled from two additional energy scales appearing in transport and bulk susceptibility measurements, suggesting a fluctuating charge/orbital state that freezes into an inhomogeneous electronic ground state where tunneling and sliding effects manifest under increasing electric field strength.

Chapter 5 References

[1] F. Wang and T. Senthil, Phys. Rev. Lett. **106**, 136402 (2011).

[2] S. Moon, H. Jin, K. W. Kim, W. Choi, Y. Lee, J. Yu, G. Cao, A. Sumi, H. Funakubo, and C. Bernhard, Phys. Rev. Lett. **101**, 226402 (2008).

[3] D. Pesin and L. Balents, Nature Physics **6**, 376 (2010).

[4] B. Yang and Y. B. Kim, Physical Review B **82**, 085111 (2010).

[5] S. Ruddlesden and P. Popper, Acta Crystallogr. **11**, 54 (1958).

[6] B. Kim, H. Ohsumi, T. Komesu, S. Sakai, T. Morita, H. Takagi, and T. Arima, Science **323**, 1329 (2009).

[7] B. Kim, H. Jin, S. Moon, J. Kim, B. Park, C. Leem, J. Yu, T. Noh, C. Kim, and S. Oh, Phys. Rev. Lett. **101**, 076402 (2008).

[8] J. Longo, J. Kafalas, and R. Arnott, Journal of Solid State Chemistry **3**, 174 (1971).

[9] G. Cao, Y. Xin, C. Alexander, J. Crow, P. Schlottmann, M. Crawford, R. Harlow, and W. Marshall, Physical Review B **66**, 214412 (2002).

[10] S. Boseggia, R. Springell, H. Walker, A. Boothroyd, D. Prabhakaran, D. Wermeille, L. Bouchenoire, S. Collins, and D. McMorrow, Physical Review B **85**, 184432 (2012).

[11] I. Franke, P. Baker, S. Blundell, T. Lancaster, W. Hayes, F. Pratt, and G. Cao, Physical Review B **83**, 094416 (2011).

[12] J. Rodriguez-Carvajal, in *satellite meeting on powder diffraction of the XV congress of the IUCr* (Toulouse, France:[sn], 1990).

[13] C. Dhital, S. Khadka, Z. Yamani*, et al*, Physical Review B **86** (2012).

[14] N. Kini, A. Strydom, H. Jeevan, C. Geibel, and S. Ramakrishnan, Journal of Physics: Condensed Matter **18**, 8205 (2006).

[15] S. Boseggia, R. Springell, H. C. Walker, A. T. Boothroyd, D. Prabhakaran, S. P. Collins, and D. F. McMorrow, Journal of Physics-Condensed Matter **24** (2012).

[16] J. W. Kim, Y. Choi, J. Kim, J. F. Mitchell, G. Jackeli, M. Daghofer, J. van den Brink, G. Khaliullin, and B. J. Kim, Phys. Rev. Lett. **109** (2012).

[17] C. Dhital, T. Hogan, Z. Yamani, C. de la Cruz, X. Chen, S. Khadka, Z. Ren, and S. D. Wilson, Physical Review B **87**, 144405 (2013).

[18] D. Arovas, F. Guinea, C. Herrero, and P. S. Jose, arXiv preprint cond-mat/0211686 (2002).

[19] P. San-Jose, C. P. Herrero, F. Guinea, and D. P. Arovas, The European Physical Journal B-Condensed Matter and Complex Systems **54**, 309 (2006).

[20] G. Cao, J. Bolivar, S. McCall, J. Crow, and R. Guertin, Physical Review B **57**, R11039 (1998).

[21] G. Cao, J. Crow, R. Guertin, P. Henning, C. Homes, M. Strongin, D. Basov, and E. Lochner, Solid State Commun. **113**, 657 (2000).

[22] G. Cao, Y. Xin, C. S. Alexander, J. E. Crow, P. Schlottmann, M. K. Crawford, R. L. Harlow, and W. Marshall, Physical Review B **66** (2002).

Chapter 6: Electronic/magnetic Phase Diagram of $Sr_3(Ir_{1-x}Ru_x)_2O_7$

(In this chapter I am going to present our comprehensive study on the electronic/magnetic phase behavior of doped system $Sr_3\ (Ir_{1-x}Ru_x)\ _2O_7$. Most of the work presented in this chapter is published in an article by Dhital et.al "Carrier localization and electronic phase separation in a doped spin-orbit driven Mott phase in $Sr_3(Ir_{1-x}Ru_x)_2O_7$" *Nature Communications* 5, 3377 (2014).

6.1 Motivation

Iridium^{4+} ions with a half-filled 5d shell in a cubic octahedral oxygen coordination occupy a unique region in relative energy scales: one where a model of crystal field splitting combined with strong spin-orbit coupling (SOC) breaks the five-fold degeneracy of electronic states into fully occupied $J_{eff}=3/2$ and half-filled $J_{eff}=1/2$ bands [1,2]. The resulting bandwidth-narrowed $J_{eff}=1/2$ states allow the relatively modest U (~1.5-2 eV) [3] inherent to these 5d-transition metal elements to split the band and generate a charge-gap. A SOC-assisted Mott phase results, allowing an unexpected manifestation of correlation-driven physics in materials with extended 5d-electron wave functions. Doping this spin-orbit Mott phase has since generated predictions of stabilizing states analogous to those found in doped strongly correlated 3d-electron Mott insulators such as the high temperature cuprate superconductors [4]. To date however, the role of Coulomb interactions in the doped $J_{eff}=1/2$ Mott phase remains contentious with no direct observations of correlated electronic phase behavior. Two prototypical $J_{eff}=1/2$ Mott materials are the n=1 and n=2 members of the iridate Ruddelsden-Popper series $Sr_{n+1}Ir_nO_{3n+1}$ [5,6]. Here the bilayer system $Sr_3Ir_2O_7$ (Sr-327) possesses a low temperature charge-gap of $E_g=130$ meV [7] roughly reduced by a factor of four from the gap of its single layer cousin Sr_2IrO_4 [8]. This reduced gap renders the Sr-327 system a fortuitous starting point for perturbing the $J_{eff}=1/2$ Mott phase and exploring carrier-induced electronic phase behavior as the system is driven toward the metallic regime. In this chapter we describe the electronic phase behavior of Sr-327 as it is driven from a $J_{eff}=1/2$ Mott insulator into the metallic regime via hole-doping in an effort to understand the role that electron-electron correlations play once free charge carriers are introduced.

6.2 Crystal Growth and Preliminary Characterization

The single crystals of $Sr_3(Ir_{1-x}Ru_x)_2O_7$ were grown by conventional flux methods similar to earlier reports [1] using a $SrCl_2$ flux. Crystals were grown in platinum crucibles using IrO_2 (99.98%, Alfa Aesar), RuO_2 (99.98%, Alfa Aesar), $SrCO_3$ (99.99%, Alfa Aesar), and anhydrous $SrCl_2$ (99.5%, Alfa Aesar) in a 2:3:15 molar ratio. Starting powders were partially sealed inside the crucible with a Pt lid and further contained inside alumina crucibles. Mixtures were heated up to 1380 °C, cooled to 850 °C at a rate of 3.5 °C/hr, and then furnace cooled to room temperature. The resulting boule was etched with deionized water and shiny, black $Sr_3(Ir_{1-x}Ru_x)_2O_7$ crystals with typical dimensions 2 mm x 2 mm x 0.1 mm were removed. Energy Dispersive Spectroscopy (EDS) measurements were performed on numerous samples across different regions of samples from each growth batch, and measurements were also collected across different length scales to verify chemical homogeneity. Multiple crystals were tested from every batch, and from point to point on a given sample. We were able to resolve a Ru distribution homogenous within a central value +/- 1% (2% spread). The central value of Ru-concentrations between crystals from a single growth batch would vary no more than +/- 2% from a central value (4% spread). The same crystals measured via transport and magnetization measurements (only the x=0.20 and x=0.15 samples were not, although crystals from the same batch were) were used for the neutron diffraction study. Single crystals from a single batch of each concentration were ground into a powder and measured via x-ray powder diffraction within a Bruker D2 Phaser diffractometer. Lattice parameters were refined within the *I4/mmm* space group using the FullProf Rietveld refinement program [9]. Within our resolution of measurement, both *a*- and *c*-axis lattice parameters decrease continuously with increased Ru substitution [Figure. 6.2.1] as expected as the smaller Ru^{4+} ions are introduced into the lattice. We note here that laboratory-based powder x-ray measurements typically lack the intensity to resolve the known orthorhombic superlattice reflections in this material so each concentration was instead refined within the tetragonal *I4/mmm* space group. While the reduction in lattice constants is monotonic, it is not linear and seemingly maps the nonlinear contraction previously observed in $Sr_2(Ir_{1-x}Ru_x)O_4$ [10].

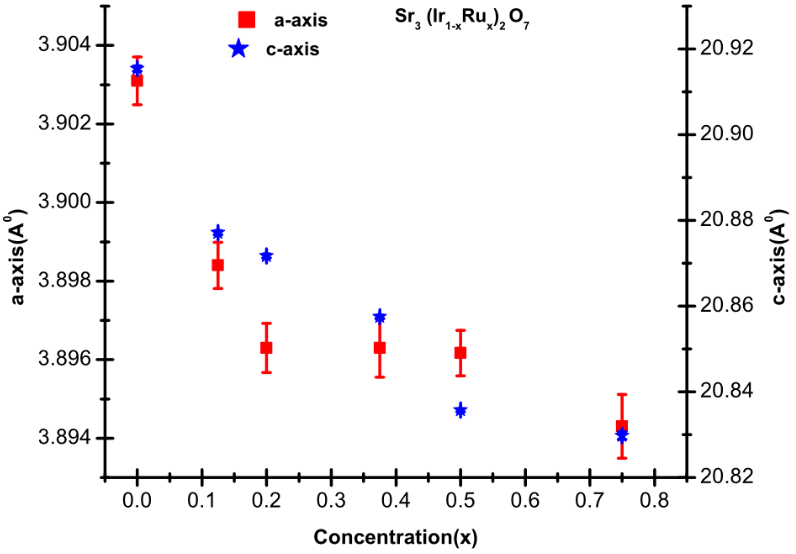

Figure 6.2.1 Variation of *a-axis* (Red square) and *c* –axis (blue star) lattice parameter as function of ruthenium concentration at room temperature.

6.3 Resistivity of $Sr_3(Ir_{1-x}Ru_x)_2O_7$

The resistivity of $Sr_3(Ir_{1-x}Ru_x)_2O_7$ crystals were measured with standard four probe techniques using Quantum design PPMS and ARS cryostat. Figure 6.3.1 (a) shows the resistivity as function of concentration and temperature for all the concentrations studied. Surprisingly, the insulating ground state of $Sr_3Ir_2O_7$ remains robust to Ru-substitution with a low temperature metallic phase appearing only beyond the critical concentration of x=0.33.Concentrations near the phase boundary show a thermally-driven MIT as illustrated in the inset of Figure 6.3.1(a) for x=0.33 with T_{MIT}=135 K. As one initial window into the corresponding evolution of the magnetic order, the high temperature inflection in ρ(T) in the x=0 parent compound is known to identify the onset of canted AF order at T_{AF} = 280 K. This feature in ρ(T) is gradually suppressed to lower temperatures upon Ru-doping, where the anomaly vanishes in the metallic regime suggesting either that the spin-charge coupling is substantially weakened in the metallic regime or that the AF order itself is substantially suppressed. We also tracked the thermally driven MIT for samples with $0.17 \leq x \leq 0.35$. Figure 6.3.2 (a,b,c,d) show the thermally driven MIT for x=0.35,0.32,0.30 and 0.17 respectively.

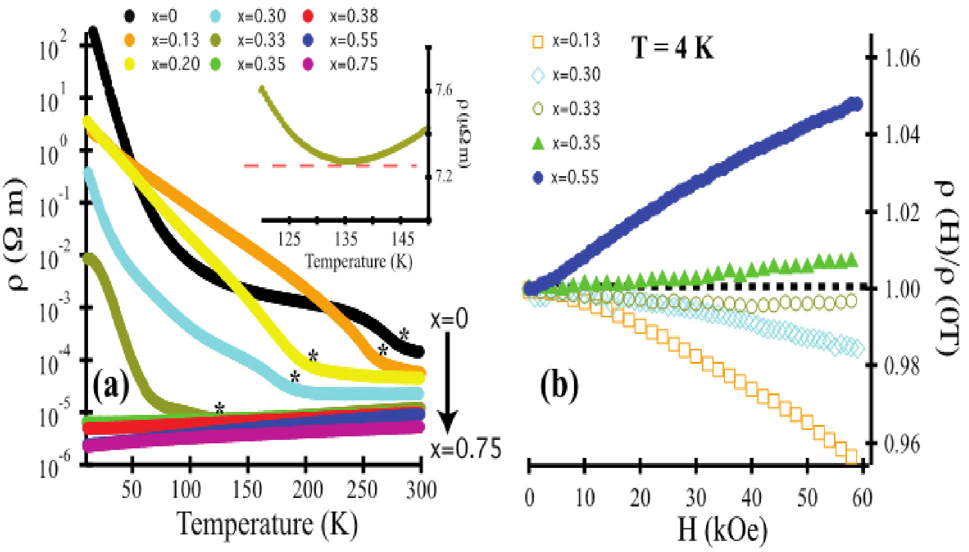

Figure 6.3.1 (a) Resistivity plotted as a function of temperature for Ru concentrations spanning the MIT. Inset shows thermally driven transition at T_{MIT} = 135 K for x=0.33. (b) 4 K magnetoresistance plotted as a function of applied field for Ru concentrations spanning the MIT.

Supporting the notion of suppressed magnetism, low temperature magnetoresistance (MR) data with the magnetic field applied perpendicular to the ab-plane are plotted in Figure. 6.3.1(b). The negative magnetoresistance previously reported in the parent material [11] (Chapter 4) and indicative of suppressed spin fluctuations or magnetic domain scattering persists in lightly doped, insulating samples; however, as the system transitions into the metallic phase, the MR smoothly switches sign from negative to positive values that increase in magnitude with continued Ru-doping. This suggests that orbital (Lorentz force) effects begin to dominate across the MIT phase boundary as the carrier concentration is enhanced while fluctuation/domain effects from AF order are damped.

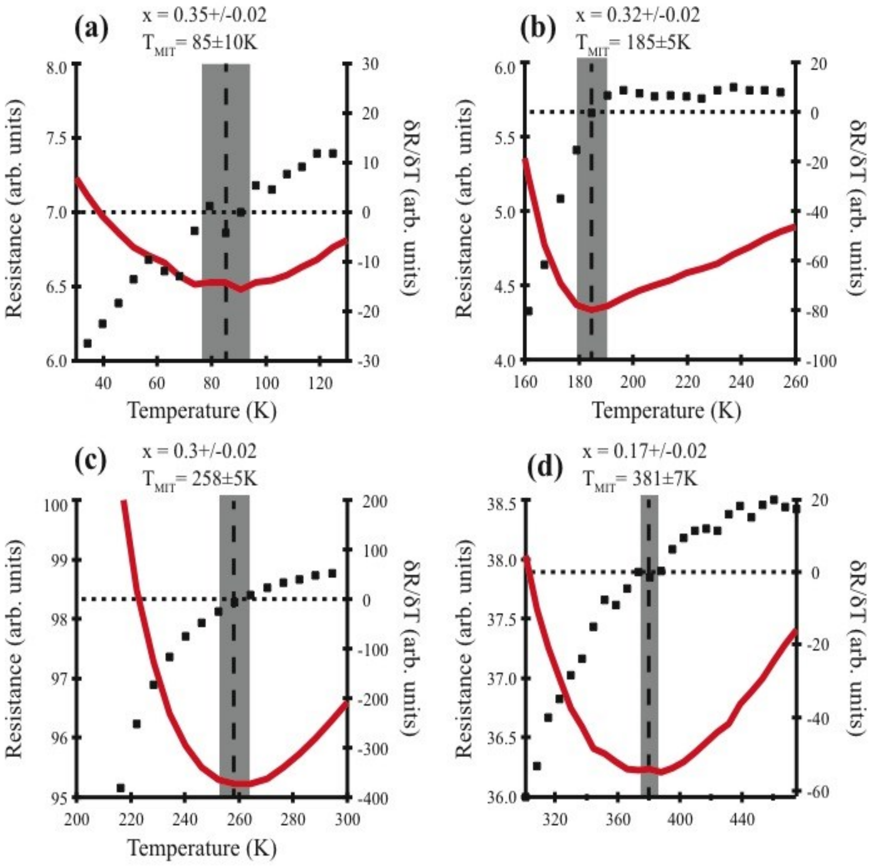

Figure 6.3.2 Resistance (red lines) and its first derivative $\frac{\delta R}{\delta T}$plotted (black squares) plotted as a function of temperature for $Sr_3(Ir_{1-x}Ru_x)_2O_7$ samples with (a) x=0.35, (b) x=0.32, (c) x=0.3, and (d) x=0.17 respectively. Vertical dashed lines show the temperature T_{MIT}. Shaded grey region shows the uncertainty in determining T_{MIT}.

6.4 Magnetization of $Sr_3(Ir_{1-x}Ru_x)_2O_7$

We also performed bulk magnetization measurements of the in-plane susceptibility on select samples using SQUID. The results are shown in Figure 6.4.1 (a). As Ru is doped into Sr-327, the onset temperature of the net ferromagnetism, arising from the canted AF order and denoted via the irreversibility temperature (T_{irr}), is reduced. Close to the critical regime, the x=0.33 sample exhibiting a thermally driven MIT with T_{MIT}=135 K [Figure 6.3.1 (a) inset] shows an onset of canted AF order at the same temperature. This suggests that near the MIT phase boundary the two transitions (T_{MIT} and T_{CAF}) become coupled and that this coupling diminishes in lightly doped samples deeper within the insulating regime. Samples with Ru-doping x>0.33 show no irreversibility in magnetization, and concentrations with a metallic ground state show only local moment behavior within resolution. The only exception is that the highest doped sample with x=0.75 shows the reemergence of T_{irr} at low temperature [Figure 6.4.1 (b)]; however the origin of this may simply be an extrinsic perturbation of the nearby Fermi-liquid phase of $Sr_3Ru_2O_7$ [12] .

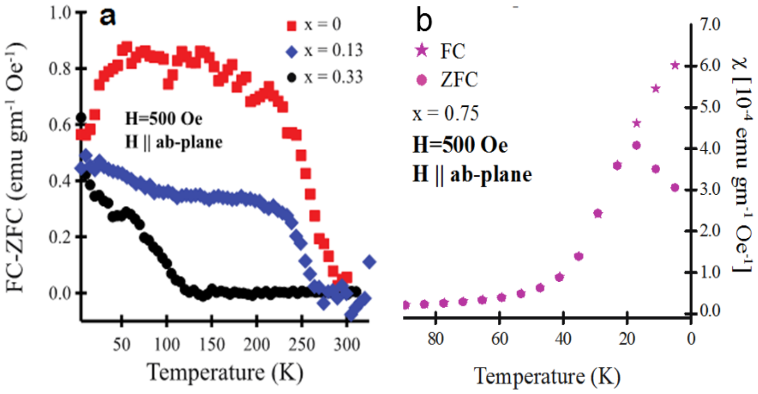

Figure 6.4.1 (a) Field cooled (FC) minus zero-field cooled (ZFC) magnetization as a function of temperature for select Ru-dopings. (b) zero-field cooled (ZFC) and field cooled (FC) magnetization data collected for the x=0.75 concentration.

Through direct analogy with $Sr_3Ru_2O_7$, [13] Ru nominally enters the Sr-327 iridate lattice in the low spin state of Ru^{4+} and subsequently introduces S=1 impurities into the J_{eff}=1/2 magnetic background. The parent Sr-327 iridate shows no local moment

(Curie-Weiss) behavior even at high temperatures, [14] unlike its single layer cousin Sr_2IrO_4 [15] however as Ru-ions are introduced into the lattice, a paramagnetic upturn begins to build in the low temperature magnetization data.

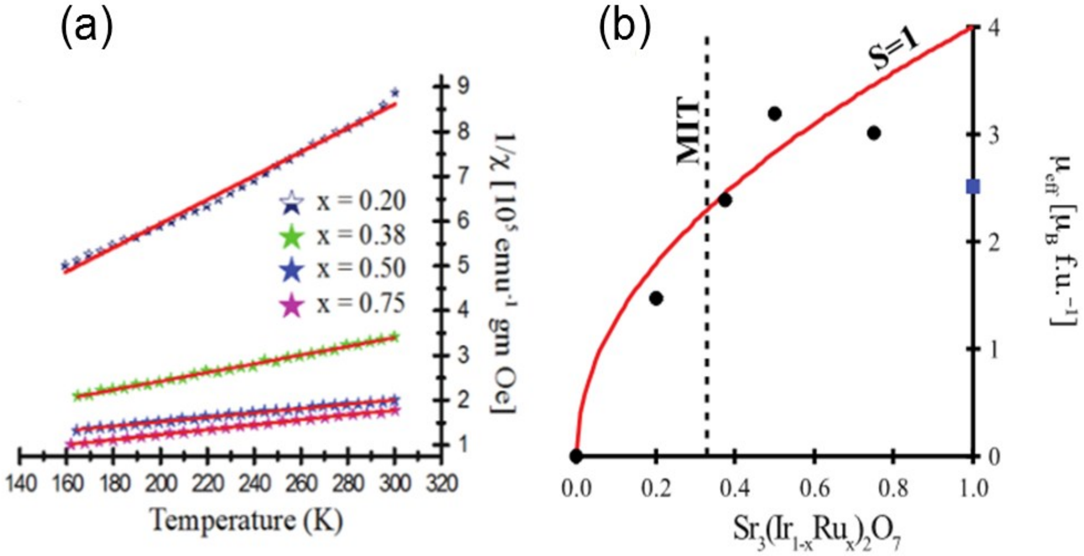

Figure 6.4.2 (a) 1/χ as a function plotted as a function of temperature. A 500 Oe field was applied parallel to the ab-plane for all concentrations with the exception of x=0.2 where a 1 T field was applied. Solid lines are fits to Curie-Weiss behavior. (b) Local moments extracted from Curie-Weiss fits plotted as a function of Ru concentration. Solid line denotes the expected full moment value for $S = 1$ impurities. Blue square shows data taken from Ikeda et al. 1 emu g^{-1} Oe^{-1} = 4π x 10^{-3} m^3 kg^{-1}. Error bars in all plots represent one standard deviation.

Immediately upon doping Ru, the known low-temperature downturn in χ (T) in the parent system [11] (Fig. 6.4.1(a)) rapidly vanishes and is replaced by a weak paramagnetic upturn. For ruthenium doped samples, the high temperature tail in the susceptibility can be fitted to a Curie-Weiss law of the form $1/\chi(T)=\Theta/C+T/C$ (where Θ is the Weiss constant and C is the Curie constant). The slope of this fit gives the effective local moment μ_{eff} by relation: $C=\frac{N_A}{3k_B}\mu_{eff}^2$, where N_A is Avogadro's number. Figure 6.4.2 (a) represent the fitted high temperature parts for x=0.2, 0.38, 0.5 and 0.75 and the resulting local moments extracted by this method are plotted in

Figure 6.4.2(b). For low dopant levels, the effective local moments extracted from each concentration track the expectation for contributions solely arising from local S=1 impurities which build continuously across the MIT. This suggests Ru-ions remain largely localized at low Ru-dopings within the insulating background of $Sr_3Ir_2O_7$ and that their survival unperturbed into the metallic regime demonstrates robust correlation effects on either side of the MIT. For doping levels beyond x=0.5, the local moments of the d-electron site ions are screened and smoothly connect to the known local moment value of metallic $Sr_3Ru_2O_7$ [13].

6.5 Neutron Scattering of $Sr_3(Ir_{1-x}Ru_x)_2O_7$

We also performed neutron diffraction experiments on HB1-A triple axis spectrometer at the High Flux Isotope Reactor (HFIR) at Oak Ridge National Laboratory (ORNL) and at N-5 triple axis spectrometer at Canadian Neutron Beam Center, Chalk River Canada. For HB1-A the incident beam was monochromated by the (0, 0, 2) reflection of a double-bounce pyrolitic-graphite (PG) monochromator with a fixed incident energy of Ei=14.65 meV, and a PG(002) analyzer crystal was used on the scattered side. Two PG filters were placed before the sample, and collimations of 40′-40′-40′-80′ were used before the monochromator, sample, analyzer, and detector respectively. Experiments on N5 were performed with a PG monochomator and E_i = 14.5 meV and PG analyzer with one PG filter placed after the sample. Collimations of 30′-60′-33′-144′ were used before the monochromator, sample, analyzer, and detector respectively. For all experiments, the crystals were aligned in HOL scattering plane. The results of the neutron scattering experiments are plotted in Figure 6.5.2. Figure 6.5.2(a) shows that, for insulating samples, the onset of long-range AF order coincides with the T_{irr} determined via the magnetization curves in Figure 6.4.1(a). Upon increased doping, however, the AF phase surprisingly survives across the MIT at the same **Q**–positions as the insulating phase, [11,16]. The resulting order parameters for metallic samples are plotted in Figure 6.5.2 (b). From the limited number of magnetic peaks observable in our neutron measurements (1, 0, *L*); *L* = 1, 2, 3, 4), the spin structure remains consistent with that of the parent system across the MIT in the phase diagram, albeit the small degree of spin canting present in the insulating parent system is necessarily eliminated or strongly suppressed in the metallic regime. The persistent AF order remains long-range within resolution with a minimum correlation length $\xi \approx 200$ Å ($\xi = 2\sqrt{2\ln(2)}\frac{1}{w}$) where w is obtained by fits of radial scans to the form $I = I_0 + Ae^{-\frac{1}{2}\left(\frac{x-c}{w}\right)^2}$).

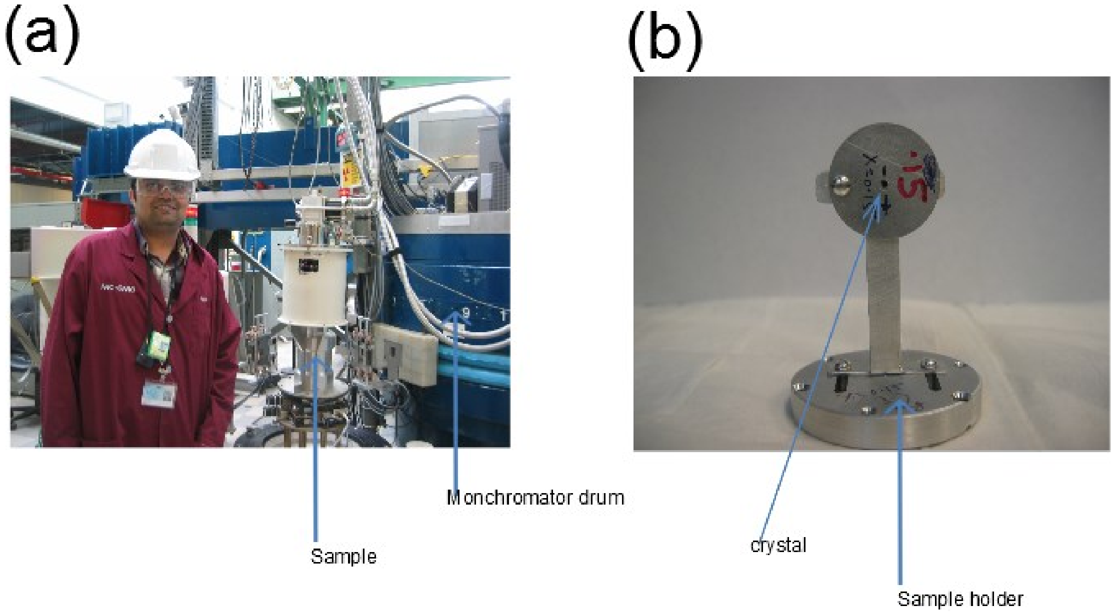

Figure 6.5.1 (a) I standing in front of N-5 triple axis spectrometer CNBC, Canada (b) A small crystal mounted on the sample mount.

Keeping a model of *c*-axis aligned moments across the MIT [5,11,16], Figure 6.5.3 (b) shows a nearly linear suppression of the AF moment in the insulating regime due to the dilution of ordered Ir-ions by localized Ru S=1 impurities; however once in the metallic regime, the ordered moment is quickly screened. In close proximity to the

MIT phase boundary, an anomalous enhancement in the ordered AF moment appears (Figure 6.5.3 (a) and b), potentially suggesting a partial relaxation of the octahedral distortion and enhanced magnetic exchange or, alternatively, induced ordering of S=1 moments from doped $4d^4$ electrons.

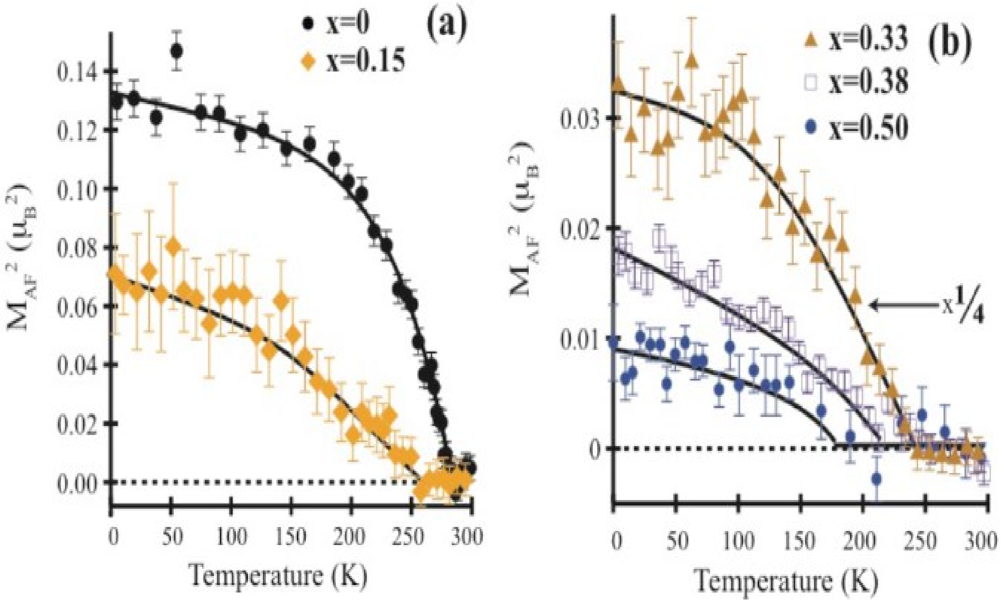

Figure 6.5.2 Neutron scattering characterization of Sr_3 $(Ir_{1-x}Ru_x)_2O_7$. (a) Temperature evolution of the square of the antiferromagnetic order parameter ($M_{AF}^2(T)$) for fully insulating x = 0 and x = 0.15. Data for x=0 reproduced from Ref. 7. (b) $M_{AF}^2(T)$ for metallic x=0.5 and x=0.38 samples as well as for x=0.33 at the phase boundary. The data for x=0.33 have been scaled by ¼ for clarity. Data for x=0, 0.38 and 0.5 were taken in HB1-A whereas the data for x=0.15 and x=0.33 were taken in N-5 triple axis spectrometer.

6.6 Scanning tunneling spectroscopy study of $Sr_3(Ir_{1-x}Ru_x)_2O_7$

In order to better understand the formation of the metallic phase, low temperature (4K) STS measurements were performed on two metallic samples x=0.35 and x=0.5 in Professor Madhavan laboratories at Boston College. The choice of two concentration is such that x=0.35 is close to MIT phase boundary toward metallic side and x=0.5 is deep into the metallic region. Figure 6.6.1 (a) shows the resulting topography of STS measurements exploring the local density-of-states (LDOS) in the *x*=0.35 concentration. Strong inhomogeneity across nanometer length scales in this sample is immediately apparent from the topography and reveals the coexistence of two distinct local environments whose representative tunneling spectra are plotted in Figure 6.6.1 (c). Dark regions with low LDOS in the corresponding map show fully gapped spectra paralleling that of the parent $Sr_3Ir_2O_7$ insulating phase [7] reproduced in Figure 6.6.1 (f), while the bright regions reveal metallic regions with an enhanced LDOS. The striking *nanoscale* coexistence of both fully gapped and gapless, metallic regions in this sample demonstrate that the sample segregates into electronically distinct regions.

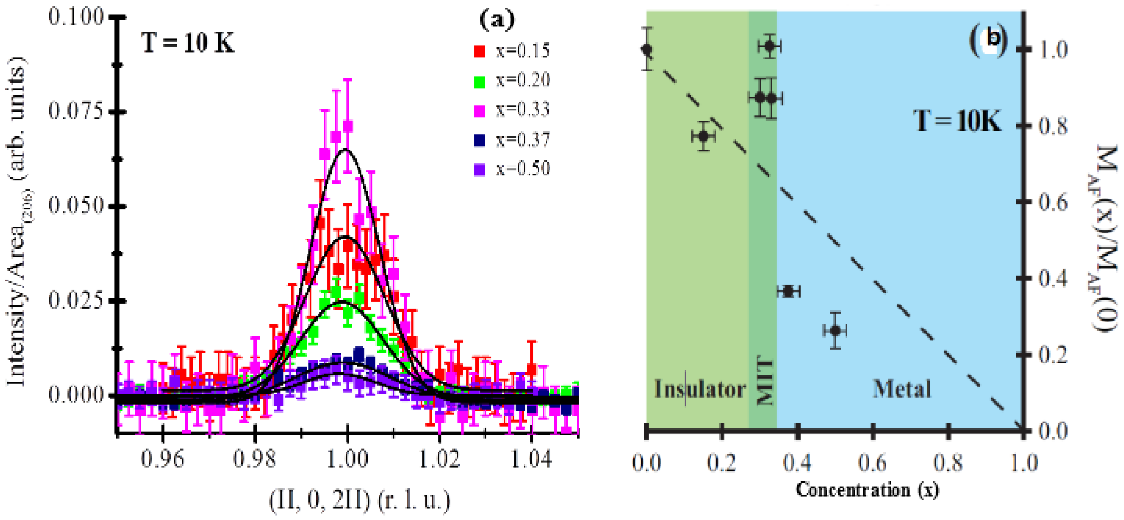

Figure 6.5.3 (a) Radial scans through the antiferromagnetic Bragg reflection **Q**=(1, 0, 2) for select concentrations of $Sr_3(Ir_{1-x}Ru_x)_2O_7$. Intensity for each sample has been divided by the integrated area of the sample's corresponding **Q** = (2, 0, 6) nuclear Bragg reflection. Solid lines are Gaussian fits to the data. Error bars are one standard deviation. (b) Ordered AF moments for $Sr_3(Ir_{1-x}Ru_x)_2O_7$ scaled relative to the parent $Sr_3Ir_2O_7$ insulator. Shaded areas denote boundaries between insulating, metallic, and critical MIT regimes.

In exploring the extent of this segregation between electronic phases or doped-carriers further, we also performed STS measurements on the metallic x=0.5 concentration. These measurements reveal this sample to be globally gapless; however, the spectra also resolve a substantial degree of electronic inhomogeneity within this nominal metal, as illustrated by a representative topography in Figure 6.6.1 (b). Correspondingly, the spectra plotted in Figure 6.6.1(d) again show two distinct shapes representing different local environments: one with suppressed V-shaped LDOS, and the second with enhanced LDOS and a spectrum that strongly resembles that of $Sr_3Ru_2O_7$ [17]. To better illustrate this, a comparison with $Sr_3Ru_2O_7$ is provided as shown in Figure 6.6.1 (e). The similarity between the hole-rich regions of the metallic x=0.5 sample and the pure bilayer ruthenate system is particularly striking, with the tunneling data resembling a thermally broadened version of a qualitatively similar electronic structure. This combined with the strong inhomogeneity of this metallic state indicates that even the fully metallic compounds continue to remain electronically segregated over nanometer length scales.

6.7 Discussion and Conclusion

Our combined transport, magnetization, neutron scattering, and STS data viewed globally paint a picture of an electronically phase separated ground state for in-plane carriers doped within a J_{eff}=1/2 Mott phase, $Sr_3Ir_2O_7$ as shown in the phase diagram (Figure 6.7.1(a)). Since the meaning of “electronic phase separation” is rather subtle at the nanoscale in doped transition metal oxides, we define its use explicitly here simply as the observation of two different local environments with distinct electronic properties. This general scenario of nanoscale phase separation either via the coexistence of distinct electronic phases or the direct segregation of holes results in the stabilization of two different local environments and a percolating conduction network sensed by our earlier transport measurements. Bare charge accumulation into puddles of 1-2 nanometer length scales may not be energetically favorable due to unscreened long-range Coulomb interactions. Without knowing the effective screening length for the Coulomb interaction and the pinning potential for carriers, it is hard to quantify what the length scale should be in $Sr_3Ir_2O_7$.

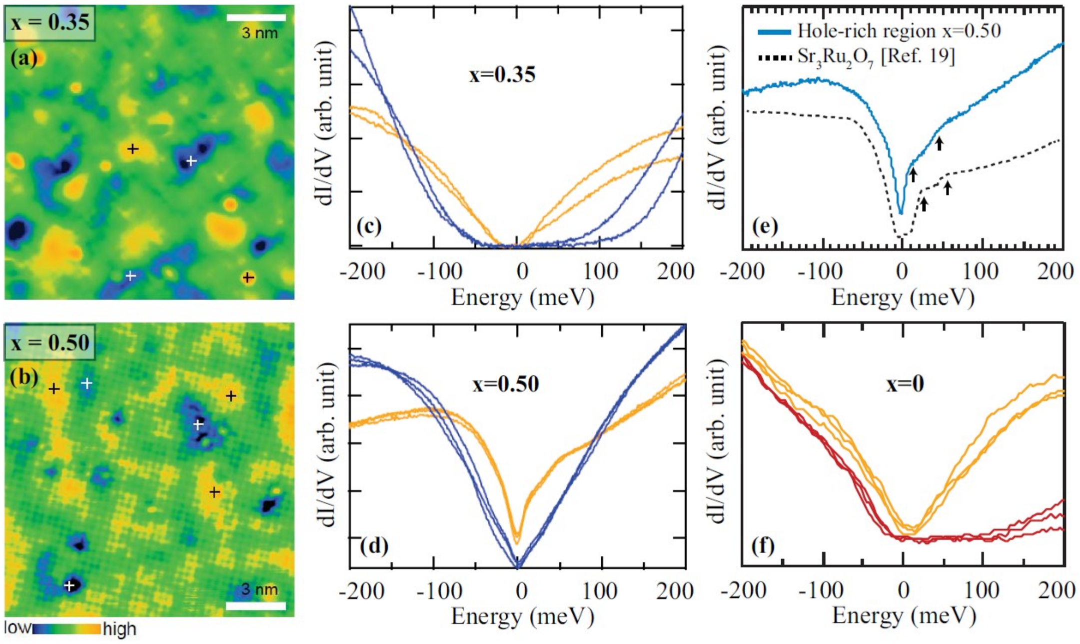

Figure 6.6.1 (STM measurements of $Sr_3(Ir_{1-x}Ru_x)_2O_7$. (a) Topography at a bias voltage of -100 mV for the x=0.35 concentration near the MIT. (b) Topography at a bias voltage of -100 mV for the x=0.5 metallic concentration. Intensity scales for topography in panels (a) and (b) are unique to each plot and their relative variation is shown via the color bar below the panels. White bars in each plot denote the length scale of 3 nm. (c) Tunneling spectra collected in gapped and gapless electronically phase separated regions denoted by blue and yellow curves collected at white and black crosses in the corresponding map (d) Spectra for x=0.5 within two electronically phase separated regions denoted by yellow and blue curves collected at black and white crosses respectively in the topography. (e) High resolution tunneling data collected within a bright region of the x=0.5 sample in panel (b). Dashed line is low temperature STM data for $Sr_3Ru_2O_7$ reproduced from Iwaya et.al [17]. (d) Spectra collected for $Sr_3Ir_2O_7$ in regions with enhanced LDOS due to oxygen defects (yellow curves) and spectra collected away from defects showing the full charge gap (red curves). We note here that the inhomogeneity observed within the parent insulating system stems from relatively rare regions of oxygen defects and that the majority of the surface showed fully gapped behavior (red curves), whereas for the x=0.35 and x=0.5 systems the entirety of the samples showed strong electronic inhomogeneity across nanometer length scales.

An alternative phase separation into electrically neutral, yet electronically distinct, phases separated by a first order phase transition is instead a likely mechanism; however we are unable to differentiate this from the pure carrier segregation scenario. Regardless of which scenario dominates, the carriers within metallic patches remain initially localized across ~1-2 nm length scales, and at the critical concentration where transport measurements show a MIT (x~0.35), this leads to the formation of metallic patches percolating within the fully gapped, spin-orbit Mott insulating background. At Ru-substitution levels below x=0.35, the thermally driven MIT is therefore the likely result of the expansion of these metallic puddles due to thermal shifts in their free energy relative to insulating host phase. Phase inhomogeneity continues deep into the metallic regime, where our STS data directly demonstrate nm-scale texture in metallic Sr_3IrRuO_7 comprised of two distinct regions: (1) Large LDOS regions with an electronic response mirroring the $4d^4$ electronic spectrum of isostructural $Sr_3Ru_2O_7$ [17] and (2) Regions with V-shaped spectra with LDOS suppressed close to the Fermi energy. Since their valence states are rather far from the Fermi-level, A-site doping in perovskite oxides is historically envisioned as controlling the filling of d-bands on the B-sites by donating their valence electrons to the entire system. The resulting doping mechanism gives rise to a rapid suppression of the Mott phase such as in A-site doped Sr_2IrO_4 [18] and $Sr_3Ir_2O_7$. Our B-site doping in Sr-327, however, reveals that holes nominally added via Ru-substitution remain localized within the IrO_2-planes until nearly 35% of the Ir $5d$ ions have been replaced, close to the classical 2D percolation threshold of 41% [19].Even beyond this threshold at 50% replacement; hole-rich regions remain phase separated. Given that Ru-doping is nominally a strong perturbation to the weakly insulating ground state of Sr-327, this observation is striking and suggests that Coulomb interactions and correlation effects remain essential across the majority of the phase diagram of this system.

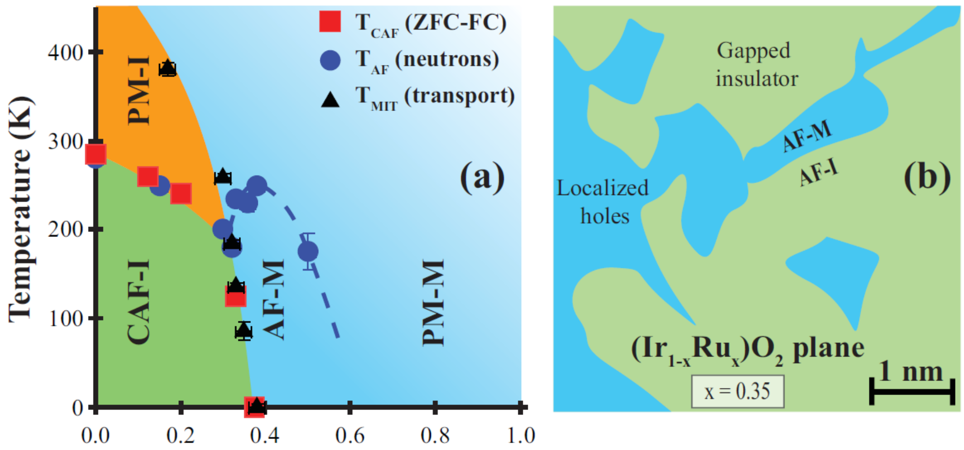

Fig 6.7.1 Electronic phase diagram of $Sr_3(Ir_{1-x}Ru_x)_2O_7$ (a) Evolution of electronic phases of $Sr_3(Ir_{1-x}Ru_x)_2O_7$ as a function of Ru concentration. CAF-I denotes the insulating canted antiferromagnetic phase, PM-I denotes the paramagnetic insulating phase, AF-M denotes the AF ordered metallic state, and PM-M indicates the paramagnetic metallic regime. Squares indicate the onset of canted AF order determined with bulk susceptibility measurements, circles denote the onset of AF order as observed via neutron direction measurements, and triangles indicate the transition temperatures for thermally driven MITs near the phase boundary. (b) Illustration of the basal-plane showing electronically phase separated holes near the percolative threshold, which nucleate within the spin-orbit Mott insulating background of $Sr_3Ir_2O_7$. Error bars in all plots represent one standard deviation.

Our combined neutron scattering and STS data reveal that the AF ordered state that survives across the MIT has a spin-spin correlation length (ξ>200 Å) that spans across the phase separated puddles of gapped and metallic regions—revealing a globally AF ordered phase. Furthermore in concentrations doped close to the MIT, the recovery of the ordered AF moment to values nearly equaling that of the undoped parent $Sr_3Ir_2O_7$ rules out any trivial superposition of chemically distinct phases. A magnetically ordered, metallic state beyond the MIT is reminiscent of the phase diagrams of $(Ca_{1-x}Sr_x)_3Ru_2O_7$ [20] and $Ca_{2-x}Sr_xRuO_4$ [21]; however, from our current measurements of $Sr_3(Ir_{1-x}Ru_x)_2O_7$ the critical point is not directly tied to a structural phase transition. AF metallic states have also been proposed in disordered and binary alloy Mott phases as an intermediate state prior to the onset of Anderson localization [22, 23]. The global picture our data provide show that the physics here is more complex than that of a trivially diluted AF system with percolative transport. The percolating metallic network seemingly can be induced to order by the host AF matrix, which may explain why the ordered AF moment is actually enhanced near the region of maximum heterogeneous interface area at the MIT as well as why AF order survives across the percolation threshold where no infinite domain of the AF host persists. Local antiferromagnetism does however naively persist across the critical concentration and can continue to influence the metallic phase into the heavily Ru-doped regime. Eventually this gives way to a globally gapless AF phase in the x=0.5 sample. We propose the following picture of magnetic interactions within this system: When they are dilute within the matrix, Ru-doped holes behave in a manner consistent with isolated ions in the S=1 low spin state giving rise to the local moment response; however, increasing the Ru-doping level increases the density of these isolated magnetic impurities, eventually nucleating clusters of metallic regions (resolved directly in our STS measurements). Within these metallic puddles, whose percolation generates the MIT, the local moment should be quenched at low temperatures in a Fermi-liquid ground state; however, these puddles may still be magnetically ordered due to proximity of local AF order in neighboring regions and a large spin susceptibility arising from their nested Fermi surface pockets. Such an instability is indeed known to be present along the $\mathbf{Q}=(\pi, \pi)$ in-plane wave vectors of $Sr_3Ru_2O_7$ [24] where an enhanced density of states is nested at the Fermi level due to the $\sqrt{2}\times\sqrt{2}$ structural zone folding. In this regard, this suggests similarities to the thermally driven MIT in the prototypical Mott system VO_2, where percolating metallic puddles display significant correlation effects [25]. More broadly, the survival of an ordered magnetic moment into the metallic state of the system demonstrates that electron-electron correlations remain relevant across the MIT of this system and argues against the picture of $Sr_3Ir_2O_7$ as a trivial band-insulator simply driven by the zone-folding that occurs at the onset of AF order. The evolution of AF order across the MIT in the phase diagram of this hole-doped spin-orbit Mott insulator demonstrates that a rich interplay can be realized at the boundary between a novel J_{eff}=1/2 insulator and a correlated metal. The localization of Ru-doped carriers into a phase separated ground state surprisingly parallels the strongly correlated phase behavior of *3d*-transition metal oxide systems such as the B-site doped correlated manganites [26--29] and reveals that correlation physics can play a dominant role in the electronic phase formation of a doped spin-orbit Mott insulator. Our findings demonstrate that correlation effects felt by carriers introduced within in a *5d* Mott phase remain robust enough to drive electron localization, a key ingredient in emergent phenomena such as high temperature superconductivity and enhanced ferroic behavior. This opens up a new frontier for exploring correlated electron phases within the presence of strong spin-orbit coupling effects inherent to a 5d-electron setting.

Chapter 6 References

[1] B. J. Kim, H. Ohsumi, T. Komesu, S. Sakai, T. Morita, H. Takagi, and T. Arima, Science **323**, 1329 (2009).

[2] B. J. Kim, H. Jin, S. J. Moon*, et al*, Phys. Rev. Lett. **101** (2008).

[3] Q. Wang, Y. Cao, J. Waugh, S. Park, T. Qi, O. Korneta, G. Cao, and D. Dessau, Physical Review B **87**, 245109 (2013).

[4] F. Wang and T. Senthil, Phys. Rev. Lett. **106**, 136402 (2011).

[5] J. Kim, Y. Choi, J. Kim, J. Mitchell, G. Jackeli, M. Daghofer, J. van den Brink, G. Khaliullin, and B. Kim, Phys. Rev. Lett. **109**, 037204 (2012).

[6] S. Moon, H. Jin, K. W. Kim, W. Choi, Y. Lee, J. Yu, G. Cao, A. Sumi, H. Funakubo, and C. Bernhard, Phys. Rev. Lett. **101**, 226402 (2008).

[7] Y. Okada, D. Walkup, H. Lin, C. Dhital, T. Chang, S. Khadka, W. Zhou, H. Jeng, M. Paranjape, and A. Bansil, Nature materials (2013).

[8] J. Dai, E. Calleja, G. Cao, and K. McElroy, arXiv preprint arXiv:1303.3688 (2013).

[9] J. Rodriguez-Carvajal, in *satellite meeting on powder diffraction of the XV congress of the IUCr* (Toulouse, France:[sn], 1990).

[10] R. Cava, B. Batlogg, K. Kiyono, H. Takagi, J. Krajewski, W. Peck Jr, L. Rupp Jr, and C. Chen, Physical Review B **49**, 11890 (1994).

[11] C. Dhital, S. Khadka, Z. Yamani*, et al*, Physical Review B **86** (2012).

[12] S. Grigera, R. Perry, A. Schofield, M. Chiao, S. Julian, G. Lonzarich, S. Ikeda, Y. Maeno, A. Millis, and A. Mackenzie, Science **294**, 329 (2001).

[13] S. Ikeda, Y. Maeno, S. Nakatsuji, M. Kosaka, and Y. Uwatoko, Physical Review B **62**, R6089 (2000).

[14] G. Cao, Y. Xin, C. Alexander, J. Crow, P. Schlottmann, M. Crawford, R. Harlow, and W. Marshall, Physical Review B **66**, 214412 (2002).

[15] N. Kini, A. Strydom, H. Jeevan, C. Geibel, and S. Ramakrishnan, Journal of Physics: Condensed Matter **18**, 8205 (2006).

[16] S. Boseggia, R. Springell, H. C. Walker, A. T. Boothroyd, D. Prabhakaran, S. P. Collins, and D. F. McMorrow, Journal of Physics-Condensed Matter **24** (2012).

[17] K. Iwaya, S. Satow, T. Hanaguri, N. Shannon, Y. Yoshida, S. Ikeda, J. He, Y. Kaneko, Y. Tokura, and T. Yamada, Phys. Rev. Lett. **99**, 057208 (2007).

[18] M. Ge, T. Qi, O. Korneta, D. De Long, P. Schlottmann, W. Crummett, and G. Cao, Physical Review B **84**, 100402 (2011).

[19] V. K. Shante and S. Kirkpatrick, Adv. Phys. **20**, 325 (1971).

[20] Z. Qu, L. Spinu, H. Yuan, V. Dobrosavljević, W. Bao, J. W. Lynn, M. Nicklas, J. Peng, T. Liu, and D. Fobes, Physical Review B **78**, 180407 (2008).

[21] S. Nakatsuji, D. Hall, L. Balicas, Z. Fisk, K. Sugahara, M. Yoshioka, and Y. Maeno, Phys. Rev. Lett. **90**, 137202 (2003).

[22] D. Heidarian and N. Trivedi, Phys. Rev. Lett. **93**, 126401 (2004).

[23] N. Paris, A. Baldwin, and R. Scalettar, Physical Review B **75**, 165113 (2007).

[24] A. Tamai, M. Allan, J. Mercure, W. Meevasana, R. Dunkel, D. Lu, R. Perry, A. Mackenzie, D. J. Singh, and Z. Shen, Phys. Rev. Lett. **101**, 026407 (2008).

[25] M. M. Qazilbash, M. Brehm, B. Chae, P. Ho, G. O. Andreev, B. Kim, S. J. Yun, A. Balatsky, M. Maple, and F. Keilmann, Science **318**, 1750 (2007).

[26] A. Machida, Y. Moritomo, K. Ohoyama, T. Katsufuji, and A. Nakamura, Physical Review B **65**, 064435 (2002).

[27] E. Dagotto, T. Hotta, and A. Moreo, Physics Reports **344**, 1 (2001).

[28] K. Pradhan, A. Mukherjee, and P. Majumdar, EPL (Europhysics Letters) **84**, 37007 (2008).

[29] M. Uehara, S. Mori, C. Chen, and S. Cheong, Nature **399**, 560 (1999).

Chapter 7: Iron Based Superconductors

(In this chapter I will present results of our neutron diffraction experiment revealing the effect of uniaxial pressure on the structural and magnetic phase behavior of the parent and electron (Co) doped compound Ba $(Fe_{1-x}Co_x)_2As_2$. Most of the work described in this chapter is published in an article by Dhital et al "Effect of uniaxial strain on the structural and magnetic phase transitions in $BaFe_2As_2$" Phys. Rev. Lett. 108, 087001 (2012)).

7. 1 Introduction

Iron based superconductors are a class of high temperature superconducting materials having iron as one of the constituent elements. The name begins with the discovery of superconductivity in $LaO_{1-x}F_xFeAs$ at a temperature of 26 K in February 2008 [1]. This work has invited many researchers to focus on different iron based compounds resulting in the discovery many different families of iron based superconductors with T_C as high as 56 K like: 1111 families, 122 families, 111 families, 11 families, 21311 families, 32522 families etc. Figure 7.1.1 shows the different families of compounds with highlighted FePn/Ch plane.

There are some obvious reasons why these compounds are interesting systems to study, the first reason being the coexistence of superconductivity and magnetism [2]. Second reason is the existence of wide variety of compounds that provide a playground for research. A third reason is the multiband nature of the Fermi surface which adds additional complexity to the problem. They also have high critical current and critical fields compared to cuprates which may be useful in power engineering [2]. More than that, the coexistence of magnetism and superconductivity may find its application in spintronics. All these families of superconductors share some common properties (certainly with some exceptions) which can be summarized as below [3].

1. All families have at least a two dimensional plane of FePn/Ch tetrahedra as shown in Figure 7.1.1. The superconducting transition temperature T_C is a function of bond angles as well as height of Pn/Ch above the Fe layer.
2. 3d electrons of iron are at the Fermi level and take part in superconductivity.
3. Unlike cuprates, the parent compounds are spin density wave metals (bad metals).
4. The iron moments in most of the compounds are magnetically ordered at least in some part of the phase diagram and even coexist with superconductivity.
5. The parent compounds of 1111 and 122 families of compounds are non-superconducting. Both electron and hole doping introduce superconductivity.
6. All the parent compounds of 1111 and 122 families of compounds have either simultaneous or nearly simultaneous structural and magnetic transitions [4,5] however in 111 or 11 systems this rule doesn't always apply.
7. There is Fermi surface nesting between multiple 3d bands.
8. There is evidence of presence of broken C_4 rotational symmetry phase regarding the electronic properties even if the system maintains C_4 crystalline symmetry [6].

The details of each family of compounds have been comprehensively reviewed in a few good review papers [2,3,7--10] in this field which give a broad overview of these superconducting compounds. This work is focused on the structural and magnetic phase behavior of the parent and doped 122 systems namely $Ba(Fe_{1-x}Co_x)_2As_2$ under the application of uniaxial pressure applied in this electronically anisotropic phase. I will discuss about the need for applying uniaxial pressure and its consequences in the subsequent sections.

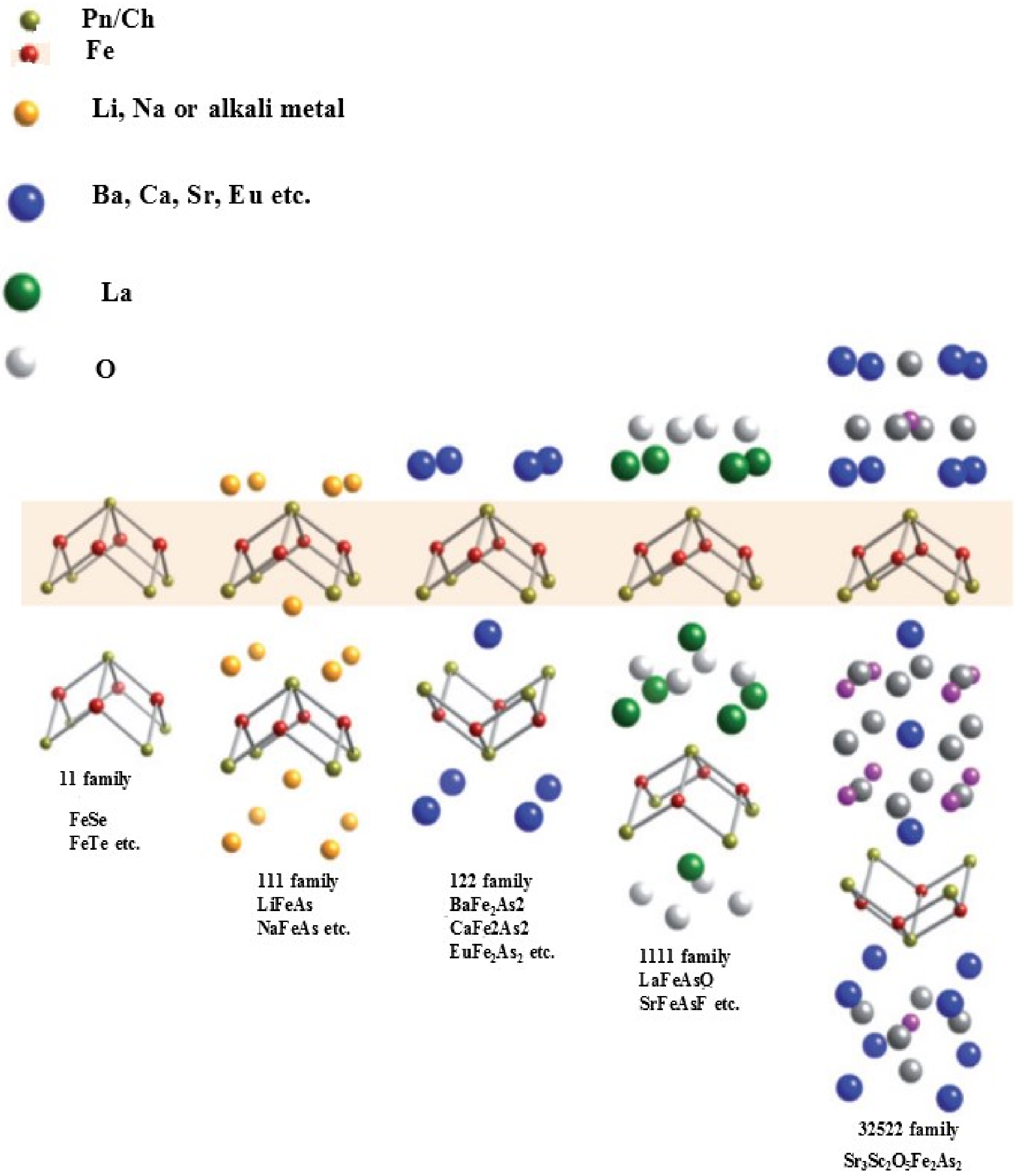

Figure 7.1.1 Different families of iron based superconductors. Reproduced from Paglione et.al [9]

7.2 Phase Diagram of Ba $(Fe_{1-x}Co_x)_2As_2$ system

This is one family among different families of iron-based superconductors abbreviated as 122 families. The parent compound $BaFe_2As_2$ undergoes almost simultaneous structural and magnetic phase transitions from high temperature tetragonal paramagnetic phase to low temperature orthorhombic antiferromagnetic (spin density wave) phase at a temperature of about T= (136 K-140 K). Under ambient conditions, the electron doping (Co doping) introduces following effects as shown in the phase diagram [Figure7.2.1].

1. The structural transition temperature (T_S) and magnetic transition temperature (T_N) are lowered.
2. The splitting of these two transitions T_S-T_N increases progressively with increasing dopant concentration.
3. The magnetic transition changes its nature from almost first order to continuous about the tricritical point x=0.22.
4. Superconductivity and magnetism coexist in the underdoped side of the phase diagram but the magnetism vanishes completely at the optimal doping where T_C is maximum (x_{op}=0.6, T_{Cmax}=22K). The magnitude of the ordered moment decreases monotonically from about 1μ_B/Fe in parent compound to immeasurably small value in the optimally doped compounds.
5. The orthorhombicity defined by: $\delta = \frac{(a_o - b_o)}{(a_o + b_o)}$ (where a_o and b_o are orthorhombic a and b axis lattice parameters) decreases progressively with doping and becomes immeasurably small upon optimal doping.
6. The superconducting dome is anisotropic. The rate of increase of T_C in underdoped region is higher than rate of decrease of T_C in overdoped region because the superconductivity and magnetism compete with each other in the underdoped region for the same electrons.

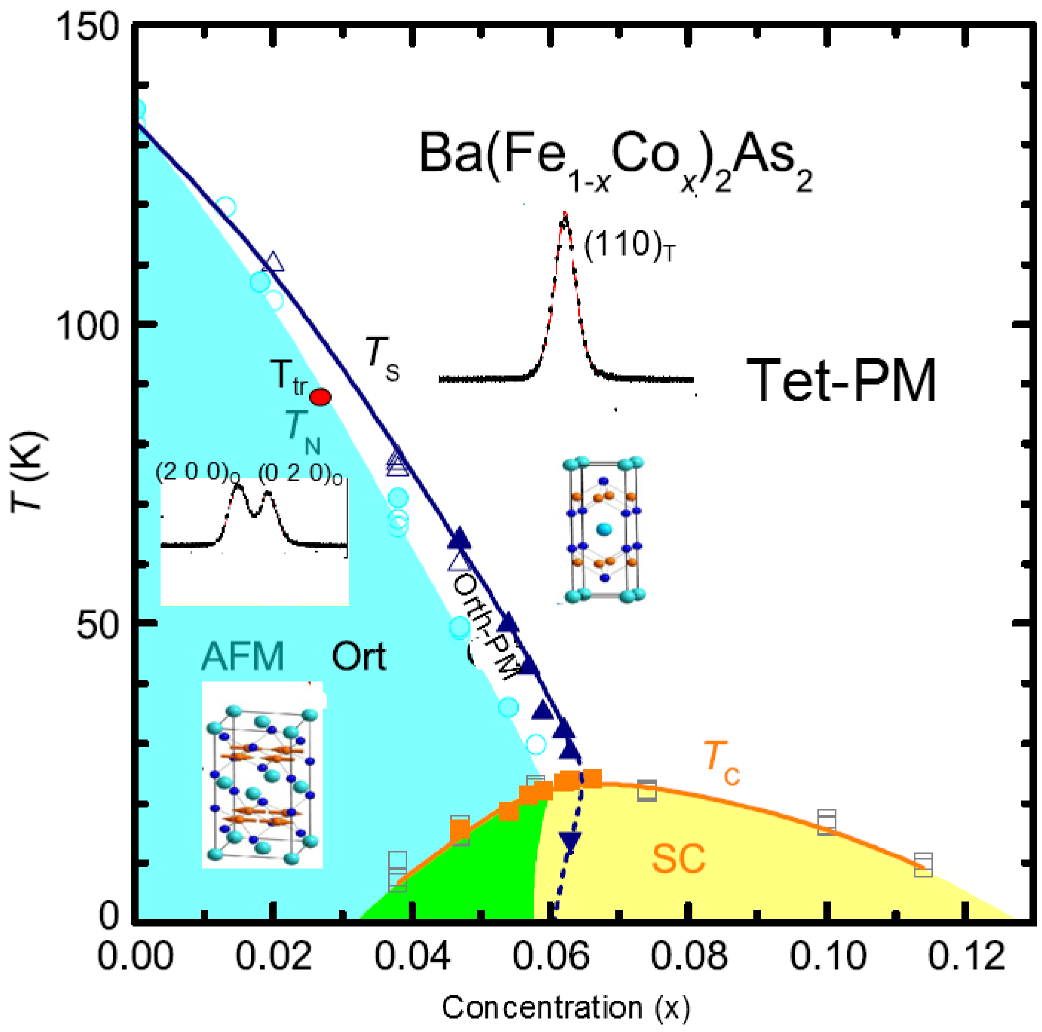

Figure 7.2.1 (a) Phase diagram of Ba (Fe$_{1-x}$Co$_x$) $_2$As$_2$ system along with crystal and magnetic structures. The red point denotes tricritical point (x_{tr},T_{tr}) [3,11--13].

7.3 Nematicity and Detwinning

One of the central questions in understanding the electronic phase behavior of the iron pnictide high temperature superconductors (high-Tc) remains the unresolved origin of their ubiquitous tetragonal-to-orthorhombic structural distortions in both parent and underdoped concentrations. While the distortion itself is subtle, resulting in a relative elongation of the basal plane a-axis by about 1%, it is widely believed to be a secondary effect driven by electronic symmetry breaking such as orbital order [14] or low energy spin fluctuations [8,15,16]. In a number of scenarios considered, the microscopic origin for this structural distortion is rooted in the presence of an otherwise hidden, electronic, nematic [6,17,18] phase whose fluctuations are ultimately suggested to play a role within the superconducting pairing mechanism. To date, however, this scenario remains a subject of active investigation. As part of this, one of the key metrics sought as a signature of nematicity (broken rotational symmetry while preserving discrete translational symmetry) is an indication of C_4-symmetry breaking within the electronic properties of the iron pnictides in an otherwise nominally paramagnetic, tetragonal (C_4-symmetric) phase. Numerous experimental probes such as dc-transport [6,19,20], optical conductivity [21], scanning tunneling microscopy [22], angle-resolved photoemission [23], neutron scattering [24], and magnetic torque [18] measurements have either directly or indirectly resolved the presence of the electronic behavior violating the C_4 rotational symmetry within the FeAs planes of different families of iron pnictide high-Tc systems. Initial studies relied on bulk probes of crystals which manifested twin structural domains below their tetragonal-to-orthorhombic structural distortion temperatures (T_S) [Figure 7.3.1]. These bulk studies necessarily rely on a symmetry breaking field [6,25] which biases twin domain formation and allows uniquely defined directions within the basal planes of these systems. The symmetry breaking fields are typically comprised of simple uniaxial strain applied to the underlying crystalline lattice; however magnetic fields [6] are also utilized. In both cases, the strong spin-lattice coupling inherent to these materials necessarily results in the perturbation of both the underlying nuclear lattice and the antiferromagnetic order as the system are prepared for study. Correspondingly, the core observation of the nematic behavior inherent to these systems, as seen via bulk probes, stems from their dramatic susceptibility to the perturbations brought on by these external symmetry breaking fields, which ultimately allow the nematic order parameter to develop. A variety of scenarios have been proposed in modeling the microscopic origin of the nematic susceptibility in the iron-based high-Tc compounds such as orbital ordering/fluctuations [14,23], low-frequency spin dynamics [24], or, more recently, scenarios that incorporate both effects [26]. Regardless of the primary driver of the electronic nematicity, a second debate has focused on the relationship between impurity scattering/in-plane defects and the origin of the nematic response [27,28]. This second debate is rooted in whether the dopant atoms themselves introduce anisotropic scattering effects that bias bulk measurements (such as charge transport studies) or whether the electronic anisotropy stems directly from a Fermi surface instability [29] that is simply tuned via charge-doping.

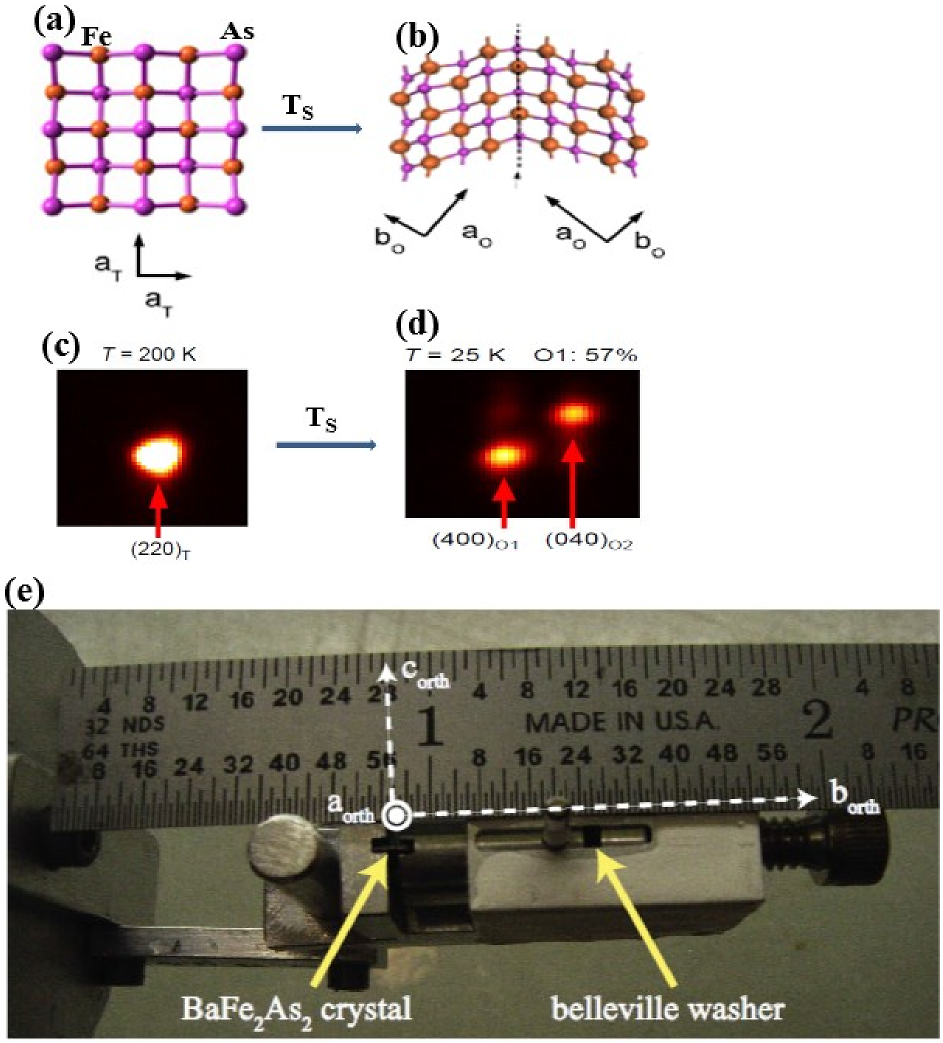

Figure 7.3.1 Illustration of twinning [6] (a) tetragonal single domain (b) Orthorhombic twin domains formed after structural distortion. (c) X-ray diffraction peak for $(220)_T$ domain (d) X-ray diffraction peaks for twin orthorhombic domains (e) small aluminum device (detwinner) designed for applying uniaxial pressure [30].

The application of external uniaxial pressure to define unique crystallographic direction for the measurement of electronic properties is called detwinning (stop twin domain formation). But this uniaxial pressure itself can bring a change in the structural and spin behavior of the system because of the spin-lattice and orbital-lattice coupling inherent in these systems. In the following sections I will discuss about our experiments focusing on the effect of uniaxial pressure on the structural and spin behavior of the parent and underdoped system.

7.4 Effect of Uniaxial Pressure on Structural and Magnetic Phase Behavior of Ba $(Fe_{1-x}Cox)_2As_2$

The bilayer pnictide system Ba $(Fe_{1-x}Co_x)_2As_2$ has proven a well-studied platform for exploring the above mentioned scenarios of electronic anisotropy [20]. In seminal charge transport studies, data showed that in-plane transport anisotropy surprisingly persisted well above the nominal tetragonal-to-orthorhombic transition temperature and the extent of this high temperature transport anisotropy evolved as a function of electron-doping [20]. Subsequent studies, however, reported that post-growth annealing and alternative means of doping dramatically dampen this anisotropy, suggesting the dominant role of an anisotropic scattering mechanism driven by in-plane dopant impurities [28,31]. Adding to the debate, recent results have shown that, above the nominal T_S, strain-induced anisotropy is independent of relative levels of disorder in samples with similar antiferromagnetic (AF) ordering temperatures (T_N) [29]. Strain-induced anisotropy in this high-temperature, paramagnetic regime is widely interpreted as directly resulting from incipient nematic order; however direct measurements of the strain-induced response of correlated magnetic order and its evolution upon doping in this regime are notably lacking. In this thesis, I will focus first on the structural and magnetic phase behavior of parent $BaFe_2As_2$ under different level of uniaxial pressure and then subsequently on the magnetic phase behavior of the Co doped system in presence of same level of uniaxial pressure.

7.5 Experimental Details

The single crystal samples were grown in Oak Ridge National Laboratory (Athena Sefat's group) using standard self-flux techniques [32]. The samples were cut along either orthorhombic *a*-axis [1 0 0] or *b*-axis [0 1 0] and mounted on a small aluminum device in [H O L] scattering plane. The force was applied along orthorhombic *b*-axis [0 1 0] (except one case where force was applied along tetragonal *b* axis) and the pressure was monitored using Belleville washer as shown in Figure 7.3.1(e). Assuming the Belleville washer is within the elastic limit, the pressure was calculated using relation $P = -kx/A$, where k is the elastic constant of washer, x the displacement from the initial position and A is the area of cross-section of the crystal. The pressure was applied at room temperature and kept fixed and the sample was loaded into the closed cycle refrigerator with He-exchange gas. We label all the lattice vectors and momentum transfers using reciprocal lattice units (r.l.u) in orthorhombic settings. Neutron scattering experiments were carried out on C-5 triple axis spectrometer and N-5 triple axis spectrometer in Canadian Neutron Beam Center Chalkriver, Canada and HB-1 and HB1-A triple axis spectrometers in High Flux Isotope Reactor (HFIR), Oakridge. Experiments on N-5 and C-5 were performed with a pyrolitic graphite (PG) monochromator and analyzer (E_i=14.5 meV) with a PG filter placed after the sample and collimations of 30’-60’-sample-33’-144’. The HB1 and HB1-A setup consisted of a double-bounce monochromator (E_i=14.64 meV), PG analyzer with a PG filter before the sample collimations of 48’-80’-sample-80’-240’.

In our experiments, we identify the onset of the structural distortion (T_S) via radial scans through the nuclear Q= (2, 0, 0) reflection. In the nominal case (without uniaxial pressure) the structural distortion is identified by significant change in the Gaussian width of this radial scan due to the formation of twin orthorhombic domains. The center of (2, 0, 0) peak however corresponds to a domain-weighted average lattice parameter, and this lattice value also shifts as the system distorts through T_S due to the inequivalent expansion/contraction of the in-plane a/b-axes. We simply label this value as the “*a-axis*" lattice constant since it is the apparent value in our scattering experiments. For the magnetic order parameter, we record the Q = (1, 0, 3) peak intensity as function of temperature. The temperature at which the peak intensity exceeds the background level is roughly defined as the onset of antiferromagnetic ordering temperature (T_N). In the following sections, the study is divided into two cases: (a) response of T_S and T_N to different levels of uniaxial strain in parent compound (ii) Effect on T_S and T_N for different doping for the same level of uniaxial pressure.

7.6 Effect of Uniaxial Pressure on T_S and T_N for Parent $BaFe_2As_2$

As mentioned earlier, the measurement of structural distortion temperature (T_S) requires radial scans along Q= (2, 0, 0) direction. We performed radial scans under 3 different conditions of uniaxial pressure: P=0 MPa, P=0.5 MPa, and P=0.7 MPa.

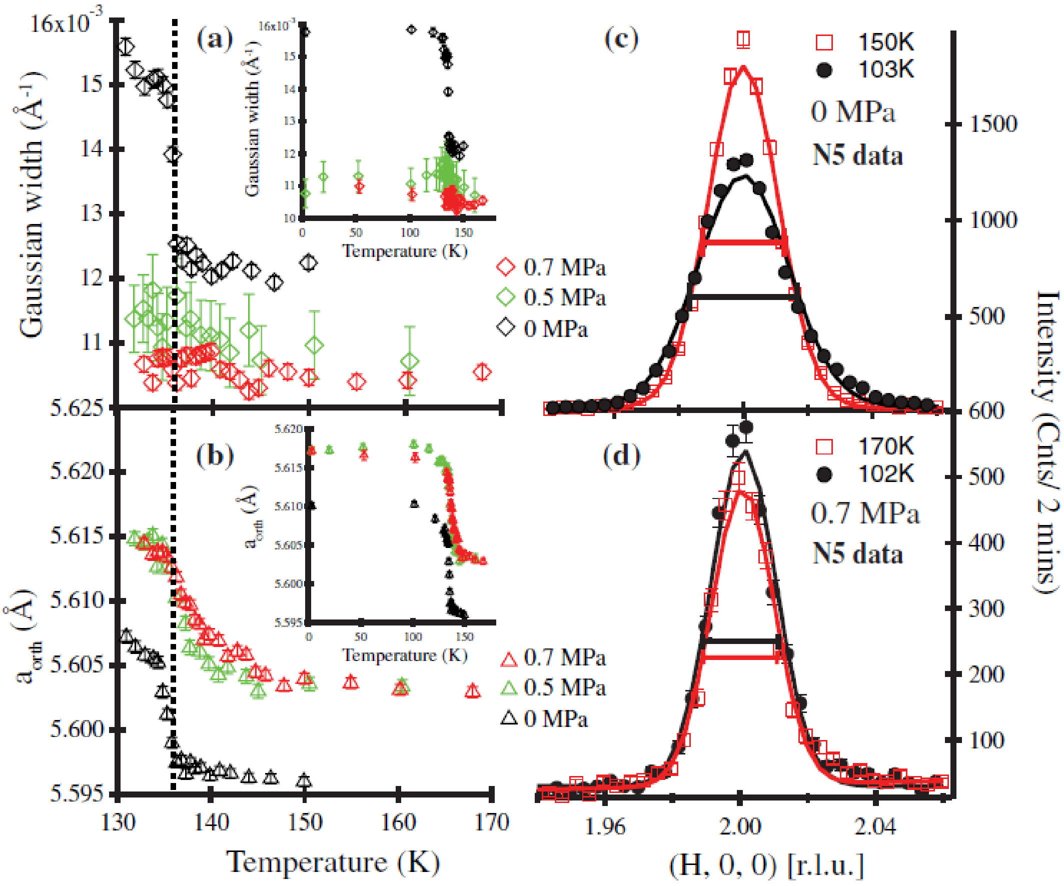

Figure 7.6.1 Peak widths and lattice parameters determined from Gaussian fits to the Q = (2, 0, 0) nuclear reflection plotted in (a),(b), respectively. Fit parameters show the evolution of the phase behavior as pressure along the b axis is increased incrementally in the same crystal. The insets show the global picture of the phase transition. Radial scans through Q= (2, 0, 0) both above and below T_S, with (c) 0 MPa and (d) 0.7 MPa of uniaxial pressure applied. Horizontal bars show the FWHM of the Gaussian fits.

The peak widths and resulting lattice parameters determined by the Gaussian peak fits to the (2, 0, 0) nuclear Bragg peak are plotted as a function of temperature for three strain fields in Figure 7.6.1(a) and 7.6.1 (b) respectively. The (2, 0, 0) peak width broadens at T_S =135.7 K in the strain-free case consistent with the expected T_S from previous studies; however, as pressure along the [0 1 0] axis is increased progressively to 0.7 MPa, the broadening observed at T_S vanishes. This is explicitly shown in Figures. 7.6.1 (c) and 7.6.1 (d), where the (2, 0, 0) peak is shown above and below T_S in both 0 and 0.7 MPa, respectively. Within the resolution of our measurements, there is no resolvable width change in peak line shape once 0.7 MPa is applied, suggesting that the crystal has been substantially detwinned. In order to resolve the onset of the structural phase transition as the crystal is progressively detwinned, the longer in-plane lattice parameter *a* is plotted as a function of temperature in Figure. 7.6.1(b) for the three different applied pressures. Here, the shift in the average in-plane lattice parameter for the strain-free crystal simply reflects the asymmetric splitting between *a* and *b* axes as the structural phase transition sets in; however, under 0.7 MPa of pressure, it is immediately apparent that the onset of T_S has shifted upward in temperature to T_S =147 K. Figure 7.6.1 (b) explicitly demonstrates that, as pressure is increased, the onset temperature for T_S shifts systematically upward as strain fields approaching the detwinning threshold are approached.

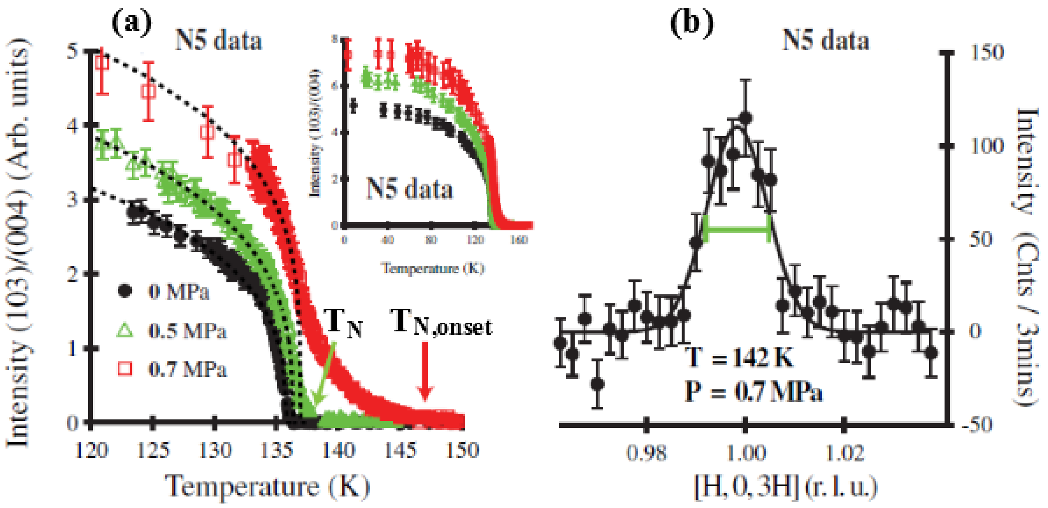

Figure 7.6.2 (a) Intensity ($I \propto M^2$) at the Q= (1, 0, 3) AF peak position normalized by the (0, 0, 4) nuclear peak plotted as a function of temperature for different pressures applied along the b axis. The inset shows the magnetic phase transition over the entire temperature range. Dashed lines are power-law fits, as described in the text. (b) Scan Q = (1, 0, 3) at T =142 K with nonmagnetic background subtracted. Horizontal bar indicates the FWHM of the (1, 0, 3) reflection measured at 3 K.

We also tracked down the effect of uniaxial pressure on the spin behavior of this parent system. As mentioned already, the peak intensity of Q= (1, 0, 3) magnetic peak as function of temperature corresponds to the good magnetic order parameter. We measured temperature dependence of the peak intensity for different pressure which is plotted in Figure 7.6.2 (a). Similar to the response of the structural phase transition, the onset of magnetic order systematically increases as strain is increased across the sample. Specifically, an enhanced tail of magnetic scattering appears that deviates from the previously modeled power-law behavior. Previous studies [5] in strain-free $BaFe_2As_2$ have already demonstrated that this kind tail of scattering is present across a similar range of temperatures (albeit at much lower intensities) and suggest that the application of strain enhances the volume fraction of the ordered moment formation across this higher temperature scale. The spin order that develops in this tail of scattering shown in Figure 7.6.2(b) is long-range, with a minimum spin-spin correlation length at 142 K of $\xi = 208 \pm 19$ Å identical within error to data collected at 3 K in this sample. The diameter of the correlation length was found via $\xi = \frac{2}{w}\sqrt{2\ln 2}$, where w is Gaussian peak width in $Å^{-1}$.

Looking at Figure7.6.2 (a), at T = 3 K, the relative scattering intensity from magnetic moments contributing to the (1, 0, 3) reflection [determined by normalizing the (1, 0, 3) to the (0, 0, 4) nuclear peak intensity] increases upon the application of increased strain. This may be simply due to the progressive reduction of the volume fraction of the sample with magnetic domains whose moments are oriented out of the scattering plane. We note, however, that, if we assume no twinning under 0.7MPa, the ordered moment at 3 K is only 0.87 μ_B, relative to 1.04 μ_B measured in the twinned, zero-strain state suggesting that the sample remains partially twinned (~43%) at 0.7 MPa pressure or the variation of moment itself with the applied pressure. The tail of scattering above T_N in Figure 7.6.2 (b) at present does not seem to originate from a simple picture of critical fluctuations above a second-order phase transition, given the lack of a resolvable divergence in the 3D spin-spin correlation length; rather, the enhanced magnetic scattering seems to stabilize over large domains within the sample as strain is increased.

As an approach to understand the mechanism behind this large shift in T_S and T_N, we applied relatively large strain field of ≈2.2 MPa along *b* axis i.e. [0 1 0] direction in a different piece of parent compound. The results are plotted in Figure 7.6.3. Consistent with our first sample, there is a sizeable shift in $T_{N,\ onset}$ which is almost same as the $T_{N,\ onset}$ of the previous sample with relatively low pressure of 0.7 MPa. This may indicate that the shift in T_N is locked irrespective of the pressure value. Similar to the previous sample, the apparent intensity of the magnetic peak increases due to the detwinning effect of the uniaxial pressure which rotates a larger volume fraction of the magnetic domains into the scattering plane. Naively, one would expect apparently doubled magnetic intensity once the sample is completely detwinned, however we only observe about 50% increase in the magnetic intensity despite the fact that the in-plane nuclear reflections no longer exhibit any broadening at the structural distortion as plotted in Figure 7.6.3 (b). Regarding the structural response at this high strain field, the sample is completely detwinned by 2.2 MPa which is evident from the absence of broadening of Gaussian width of (2, 0, 0) radial scans as shown in Figure 7.6.3 (b). Although the structural distortion temperature (T_S) is not rigorously defined due to presence of symmetry breaking field, we define a temperature $T_{S,onset}$ where sample's phase transition is detectable above any subtle distortion induced via strain as shown in Figure 7.6.3 (c). This temperature ($T_{S,onset}$=157 K) is clearly decoupled from the onset of antiferromagnetic ordering temperature which was not clear in our previous study [30].

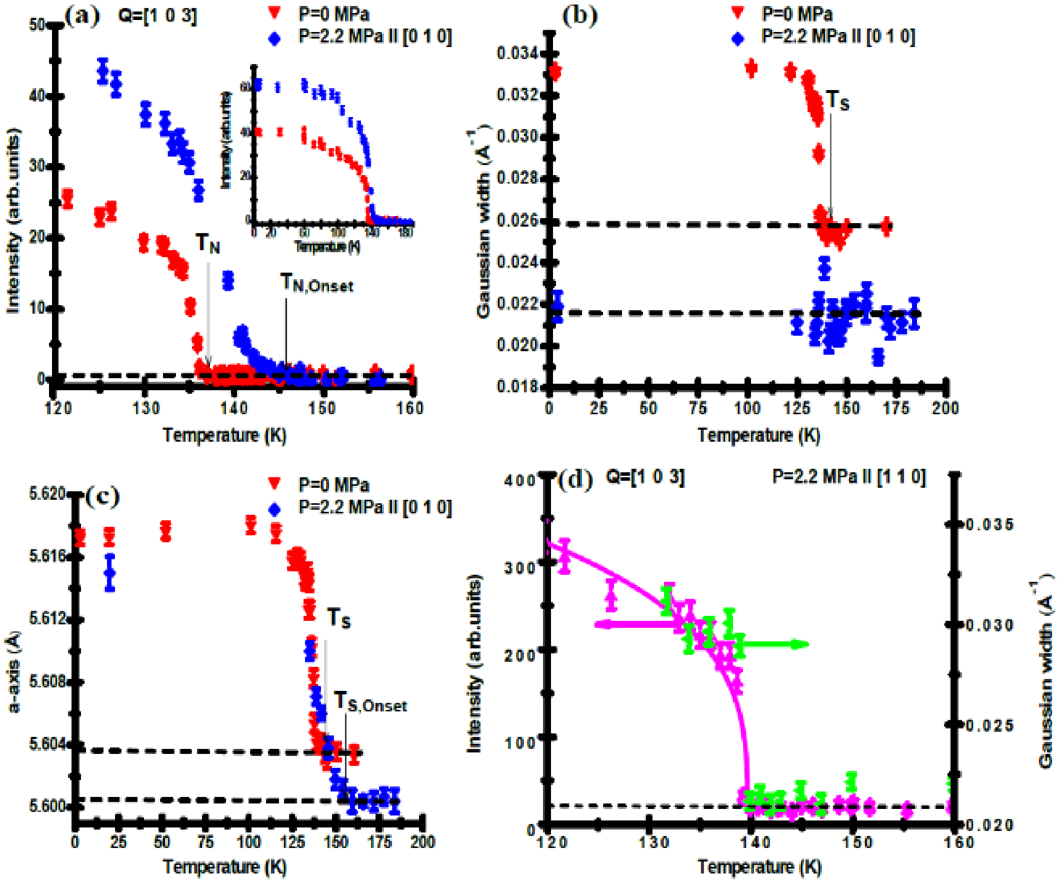

Figure 7.6.3 Neutron scattering data collected on the $BaFe_2As_2$ (x=0) sample. (a) Raw data showing the square of the magnetic order parameter collected at the (1, 0, 3) AF Bragg peak as a function of temperature. Red triangles and blue diamonds show the evolution of AF order for 0 MPa and 2.2 MPa of uniaxial pressure applied respectively (b) Temperature evolution of the fit Gaussian width of the Q=(2, 0, 0) reflection for both 0 MPa (red triangles) and 2.2 MPa (blue diamonds). (c) Temperature evolution of the effective a-axis for both 0 MPa and 2.2 MPa uniaxial pressures. (d) Raw data showing the magnetic order parameter squared collected at the (1, 0, 3) reflection and the Gaussian width of the nuclear (2, 0, 0) reflection plotted as a function of temperature. This data was instead collected with 2.2 MPa uniaxial pressure applied along the [1 1 0] direction.

We also performed a similar experiment on another different piece of parent compound but this time applying uniaxial pressure of about 2.2 MPa along orthorhombic [1 1 0] direction i.e. [0 1 0] direction in tetragonal notation. Although, T_N and T_S of this sample are different from the previous two samples, there is no shift in the onset temperature for both structural distortion and magnetic ordering [Figure

7.6.3 (d)]. The absence of a high-temperature tail within the AF order parameter for this case of [1 1 0]-oriented pressure explicitly demonstrates that the strain-induced enhancement of AF order in this system stems solely from uniaxial strain fields oriented parallel to the in-plane orthorhombic [0 1 0] axes. This fact directly parallels charge transport anisotropy effects and suggests that the enhancement of AF order and the large lattice response to the uniaxial strain stem from the same susceptibility.

7.7 Evolution of Spin Susceptibility with doping in Ba(Fe$_{1-x}$Co$_x$)$_2$As$_2$ under Uniaxial Pressure

We now turn our attention to the underdoped side of the phase diagram that covers the entire region corresponding to first order magnetic transition as well as second order magnetic transition [11]. Similar measurements across Q= (1, 0, 3) and Q = (0, 0, 4) were performed with pressure applied along orthorhombic b axis i.e. [0 1 0] direction. Figure 7.7.1 shows the response of AF order parameter under comparable levels of uniaxial strain ≈2 MPa. There is upward shift in the AF order in all samples similar to the parent system. For, x=0.015 concentration, the first order magnetic phase transition develops a prominent strain-induced tail, mirroring the parent phase behavior; however, unlike the parent material, the apparent magnetic intensity fully doubles in this sample under applied pressure. This may suggest a complete detwinning of the sample, although the behavior of the parent crystal (discussed earlier) suggests that the ordered moment may also evolve under uniaxial pressure. For the two concentrations on the second order side of tricritical point (x=0.030 and x=0.040), applied pressure also manifests a similar high-temperature tail in the AF order which convolves with the power law behavior of the order parameter.

We also measured near optimally doped sample (x=0.06) with the same procedure. This sample nominally lacks long-range AF order, and the goal here was to explore the possibility of inducing AF order under modest uniaxial pressure. The data shown in Figure 7.7.2 show that no ordered moment develops above 5 K under the application of pressure, and the system remains paramagnetic within resolution. This is consistent with the near vanishing transport anisotropy [20] at this concentration.

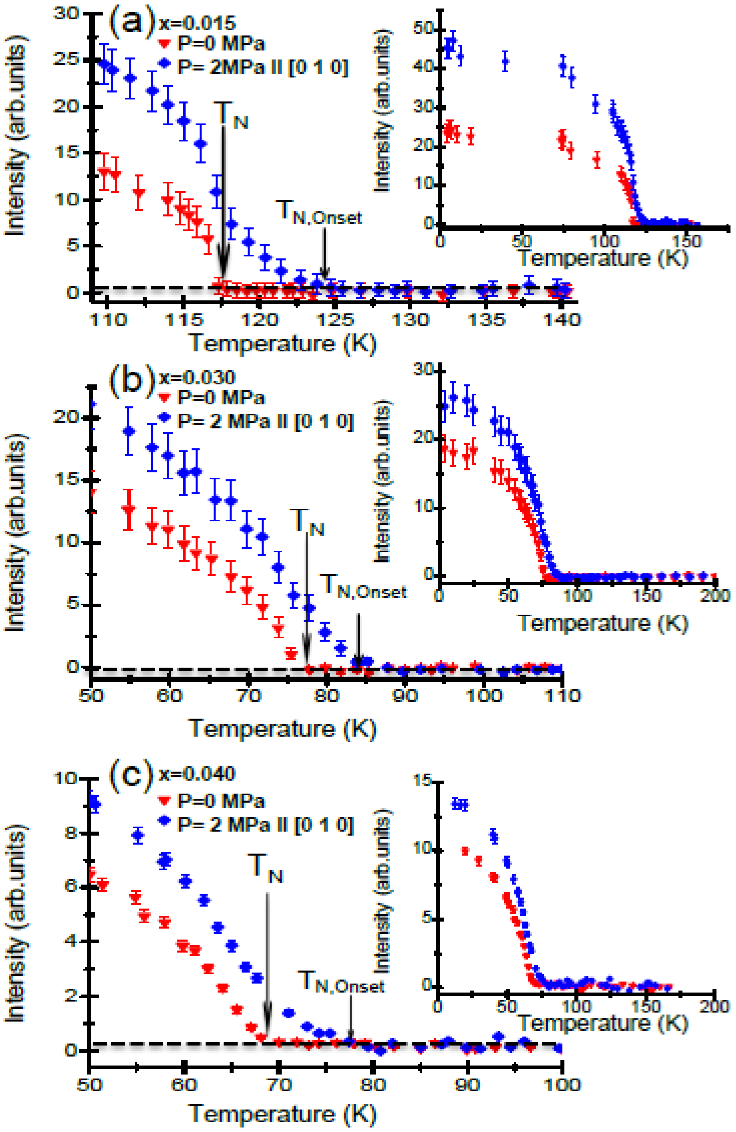

Figure 7.7.1 Raw data showing the temperature evolution of the magnetic order parameter squared, collected at the (1, 0, 3) reflection under 0 MPa (red triangles) and 2 MPa (blue triangles) pressure applied along the [0 1 0] axis. Data for the x =0.015, x =0.03, and x =0.04 samples are plotted in panels (a), (b), and (c) respectively. Insets in each panel show an expanded view of thermal evolution of the order parameter.

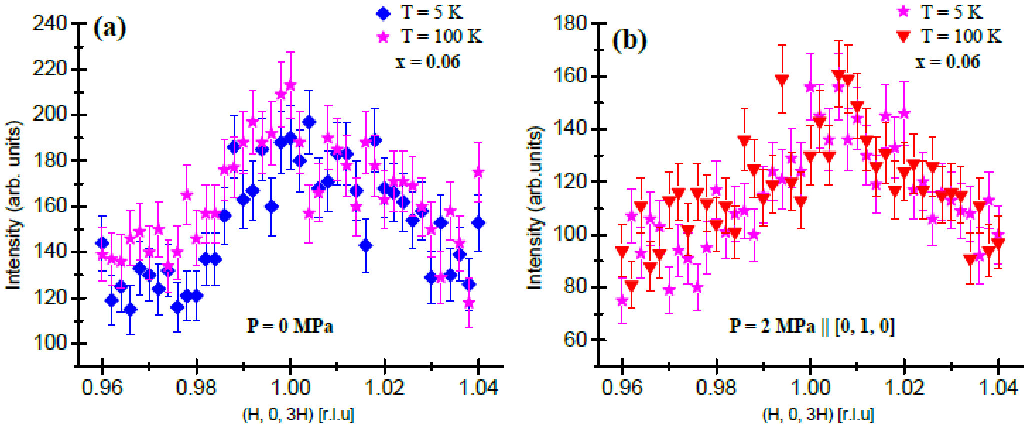

Figure 7.7.2 Radial Q-scans through (1, 0, 3) AF Bragg position both in zero pressure (a) and 2 MPa (b) for x=0.06 Co-doped sample. Data was collected at 5K and 100K.

Figure 7.7.3 shows the background subtracted radial scans collected within the tail of the strain-induced AF order parameter for all 3 samples. The data here simply reinforce our earlier observation that the AF order induced by strain fields is long-range within the resolution of our measurements. The difference in peak widths between Figure 7.7.3 panels (a,b) and panel (c) arises from differing spectrometer resolutions stemming from the use of different instruments and collimations. The experimental Bragg resolution (defined by the Gaussian full width at half-maximum of the resolution ellipsoid) for each measurement is illustrated as a central line in each sample in Figure 7.7.3 panels (d-f). These plots more clearly illustrate the gain in the apparent, saturated, long-range ordered AF moment under the application of uniaxial pressure.

We also plotted the structural distortions in Co doped samples which are presented in Figure 7.7.4. For the x=0.015 concentration, the in-plane nuclear (2, 0, 0) reflection distorts simultaneously with the onset of AF order under zero strain. Under [0 1 0] - oriented pressure, this sample detwins within resolution and the onset of T_S decouples from T_N and shifts substantially upward-similar to the response of parent material. For x=0.030 and x=0.040 concentrations, similar levels of uniaxial pressure also shift the onset of T_S upward; however neither of these samples are appreciably detwinned under this same level of pressure. This is consistent with higher Co-impurity concentrations pinning domain boundaries that subsequently require a higher strain field to bias through T_S. While the precise pressure necessary to detwinn a sample is largely an extrinsic quantity, to best of our knowledge there has been no systematic study reporting the evolution of the pressures necessary to detwinn Co-doped Ba-122 in similar quality samples.

An alternative means of analyzing the AF order parameter under strain is to fit AF order parameters as simple power laws broadened by a distribution of ordering temperatures within the sample. This broadening would potentially be due to an inhomogeneous strain field imposed across the crystal that nucleates AF order across a distribution of temperatures. The presence of a severely inhomogeneous strain field would naively be unable to account for the sharp nuclear (2, 0, 0) peak throughout the structural phase transition in the parent and x=0.015 samples; however, if the volume fraction of high strain regions is small enough, it is conceivable the expected structural broadening may be diminished below experimental resolution. In either case, fitting the magnetic order parameter to a Gaussian broadened power law behavior generates an alternative metric for assessing the influence of uniaxial strain on the development of AF order.

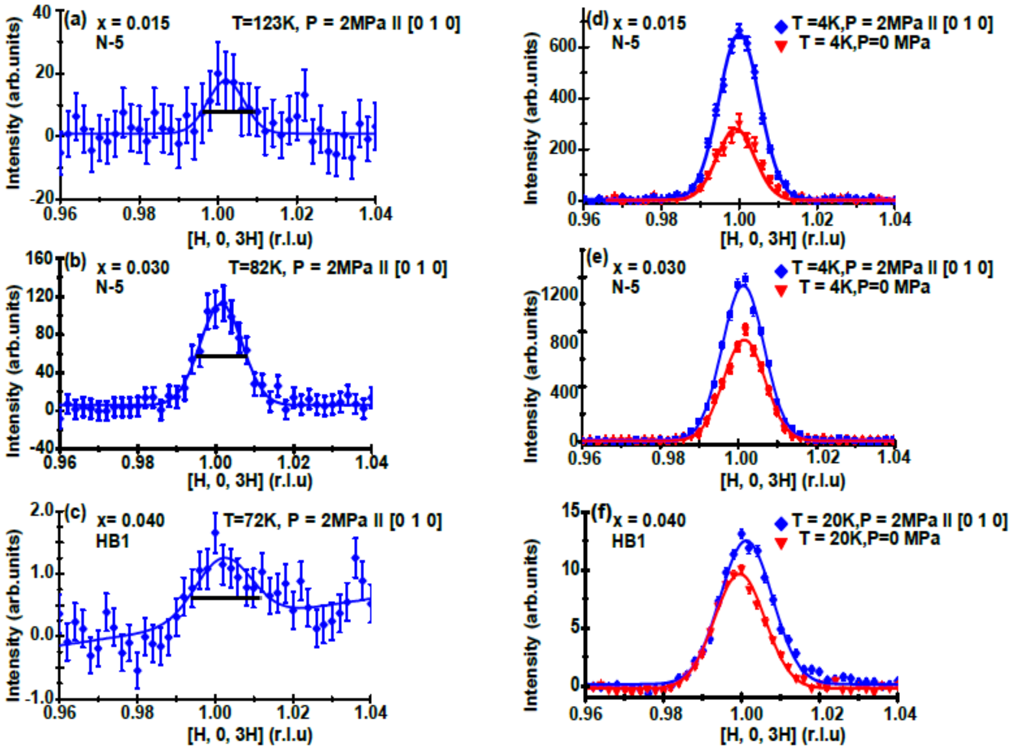

Figure 7.7.3 Background subtracted radial Q-scans through the (1, 0, 3) AF Bragg position collected within the pressure-induced high-temperature AF "tail" of the order parameter for the x =0.015 (a), x =0.03 (b), x =0.04 (c) samples. Data showing radial scans collected in the saturated region of the AF order parameter under both zero pressure and 2 MPa are plotted for x =0.015, x =0.030, and x =0.040 in panels (d), (e), and (f) respectively.

For each magnetically ordered sample (x=0, 0.015, 0.03, 0.04), the data was fit to a power law of the form [33]

$$M^2(T)=\int_0^\infty (1-\frac{T}{T_N})^{2\beta}\frac{1}{\sqrt{2\pi\sigma}}e^{-\frac{(t_\sigma-T_N)2}{2\sigma^2}}dt_\sigma \qquad (7.7.1)$$

Here β is the critical exponent and σ is the thermal width of the Gaussian distribution of T_N within the sample. It was assumed that zero strain β values remained unchanged upon the application of small levels of strain. This served to more reliably decouple β and σ values as the system transitions into the second order regime (above tricritical point).

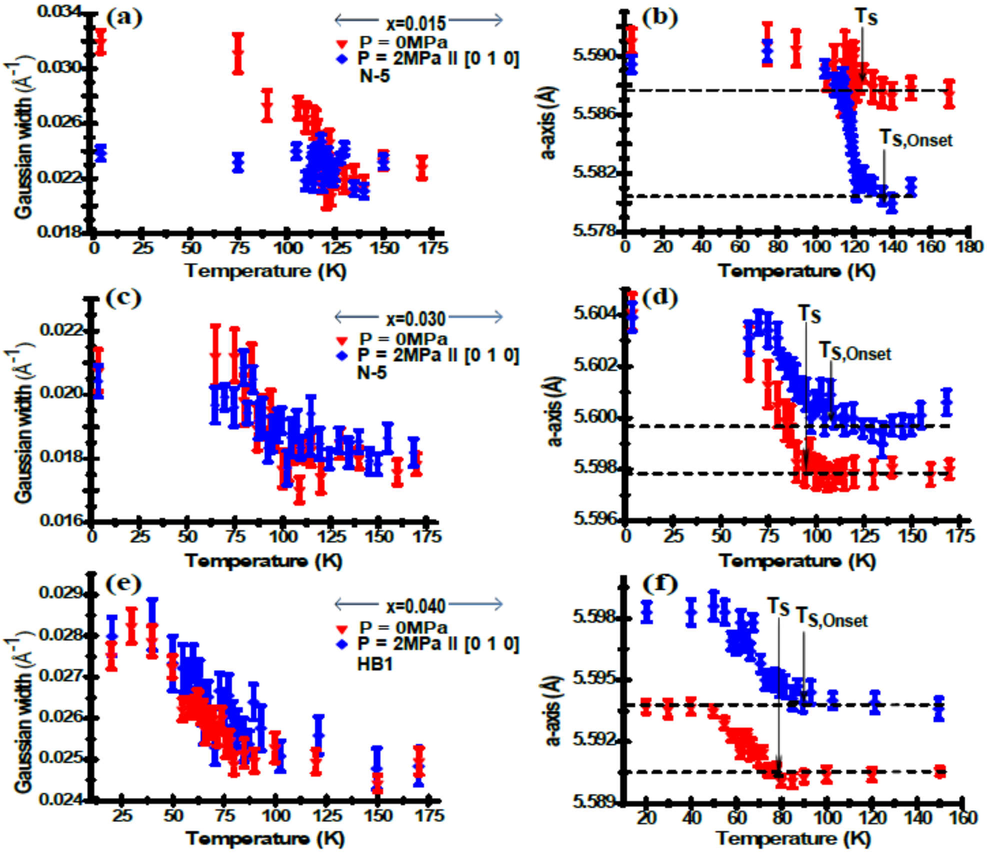

Figure 7.7.4 Gaussian widths of the (2, 0, 0) nuclear reflection measured both under 0 MPa (red triangles) and 2 MPa (blue diamonds) uniaxial pressure for the (a) x =0.015, (c) x =0.030, and (e) x =0.040 samples. The corresponding effective a-axis lattice parameters determined by the (2, 0, 0) peak position are plotted for these same samples in neighboring panels (b), (d), and (f) respectively.

Figure 7.7.5 shows the results of Gaussian-broadened fits to the square of magnetic order parameters of the x=0, 0.015, 0.03 and 0.04 samples both with and without uniaxial pressure applied along the [0 1 0] axis. Within error, the application of ≈ 2 MPa uniaxial pressure along the b-axis induces an increase of the effective Gaussian width of distribution of T_N by approximately 2 K for all samples. This uniform increase in the distribution of T_N effectively models the high temperature tail of AF order parameter and is accompanied by an upward shift in the average T_N of ≈3.5 K(within error) for all samples excluding the x=0.015 sample. This x=0.015

sample shows a minimal shift in its central T_N, potentially reflective of its closer proximity to the tricritical point at x=0.022. The fit β values using this fit method were consistent with earlier observations of a near two-dimensional Ising exponent on the first order side of the tricritical point with β = 0.14 ± 0.02 for x=0.015 which then transitions to β = 0.25 ± 0.02 for x=0.030 and β = 0.23 ± 0.01 for x = 0.040 on the second order side of the tricritical point. Ultimately, this alternative form of analyzing the magnetic order parameters under strain reveals a similar conclusion to the simple method of identifying the AF onset temperature discussed previously-namely that the absolute thermal shift in the onset of long range AF order under pressure is nearly Co-doping independent.

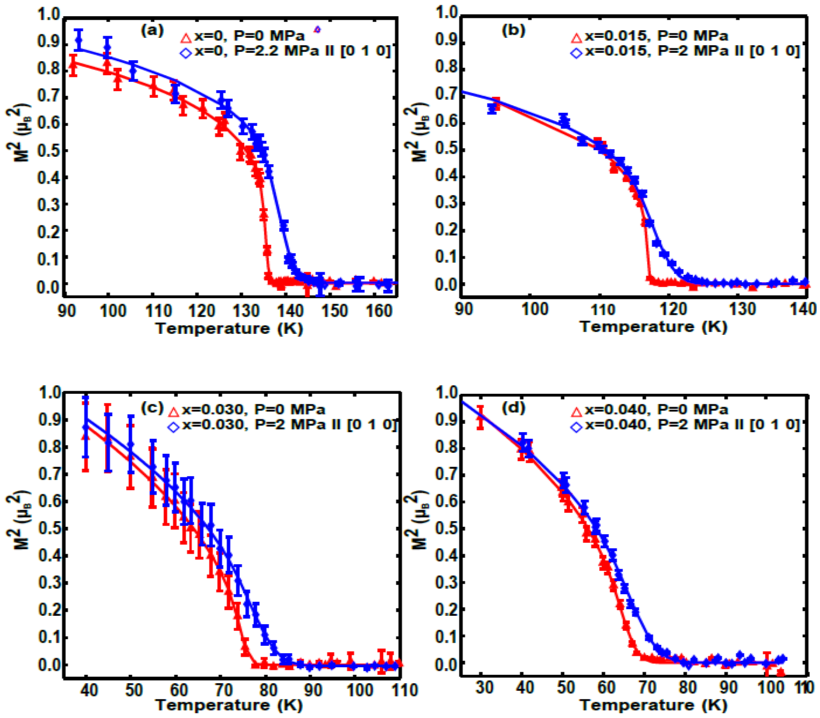

Figure 7.7.5 The results of power law fits with a Gaussian distribution of T_N (as described in the text) are plotted in panels (a-d) for the x =0, 0.015, 0.030, and 0.040 samples respectively. Fits are plotted for both 0 MPa (red triangles) and 2 MPa (blue diamonds) pressures. The corresponding fit parameters are summarized in Table 7.7.1.

7.8 Discussion and Conclusion

As mentioned earlier, in this chapter, we focused on two different aspects (i) The response of structural and magnetic behavior to different levels of uniaxial strain in parent compound and (ii) Evolution of spin behavior with doping in presence of same level of uniaxial pressure.

In parent compound the thermal shift in both T_S and T_N increases progressively with uniaxial pressure. But the onset of long range AF order seems to be locked at about 146-147 K (for P =0.7MPa as well as 2.2 MPa), however the structural distortion temperature continuously increases reaching up to about 157 K at 2.2 MPa pressure meaning that the onset of structural distortion and the magnetic ordering are decoupled.

x	T_N (0 MPa)	σ (0 MPa)	T_N(2 MPa)	σ (2 MPa)	2β
0.000	135.6 ± 0.1	0.6 ± 0.1	139.1 ± 0.3	2.6 ± 0.2	0.22 ± 0.02
0.015	117.1 ± 0.1	0.23 ± 0.06	118.4 ± 0.3	2.5 ± 0.2	0.27 ± 0.02
0.030	75.2 ± 0.2	1.3 ± 0.4	79.6 ± 0.6	4.2 ± 0.7	0.49 ± 0.03
0.040	66.0 ± 0.1	2.8 ± 0.3	69.3 ± 0.5	4.7 ± 0.5	0.46 ± 0.02

TABLE 7.7.1 Parameters for Gaussian-broadened power law fits of AF order parameters as described in the text. Units of temperatures and Gaussian widths are in Kelvin.

In the case of our doping dependent study, since the definition is T_S is not strict, we mainly focused on thermal shift of T_N for all concentrations under same level of strain field. Figure 7.8.1 (a) shows the pressure normalized shift in the onset of $T_{N,onset}$ upon applying pressure along the [0 1 0] axis i.e. the plotted quantity is $[\frac{dT_N}{P}]_{Onset} = \frac{(T_{N},_{Onset}(P) - T_{N,Onset}(0))}{P}$. Here $T_{N,onset}$ is determined empirically at the first temperature at which long-range AF order is observed above the background and P is the applied pressure. The second panel in Figure 7.8.1 (b) plots the shift in the mean distribution of T_N plus the increase in half-width at half maximum of the modeled distribution of T_N using the Gaussian-broadened power law fits plotted in Figure 7.7.5.

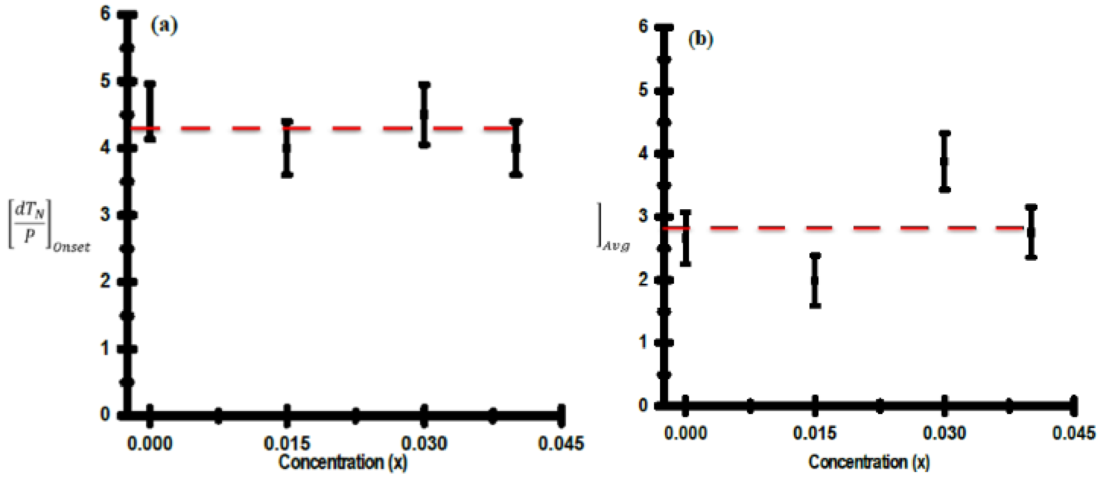

Figure 7.8.1 The shift in the empirically observed onset of $T_{N,Onset}$ normalized by the applied pressure is plotted as a function of doping in panel (a). The doping dependent shift in the average $T_{N;Avg}$ determined by the fitting parameters of Table 7.7.1 and defined in the text is normalized by the applied pressure and plotted in (b).

Explicitly, we defined a quantity $T_{N},_{Avg} = T_N + \sigma\sqrt{2\ln 2}$ to define effective shift in the leading edge of the tail of the AF order parameter using this alternative metric and the corresponding relation $[\frac{dT_N}{P}]_{Avg} = \frac{T_{N,Avg}(P) - T_{N,Avg}(0)}{P}$. In both ways of defining the pressure normalized thermal shift, the thermal shift of onset temperature seems to be independent of the doping concentration for same level of strain field. However, it corrrespondingly diverges as a fraction of T_N as Co-doping suppresses AF order as shown in Figure 7.8.2. This finding is seemingly at odds with the previous phenomenological models which predict a decrease in the strain response of AF order as the structural and AF transitions are decoupled upon electron doping. For instance, a previous analysis based on Ginzberg-Landau treatment of the magnetoelastic coupling of the structural and magnetic order parameters predicts that the shift in T_N under uniaxial stress should vary as $\partial T_N / \partial \sigma \propto (T_S - T_N)^{-1}$ [34] . Similarly, a minimal microscopic J_1-J_2-J_Z model with nearest neighbor biquadratic coupling suggests that the shift in T_N should scale as $(T_S - T_N)^{-\gamma}$ with an exponent $\gamma>2$ [35]. Recent Monte Carlo simulations simultaneously treating both the spin-lattice and orbital-lattice couplings within the Hamiltonian [26] suggest that additional degrees of complexity such as modified orbital lattice coupling upon electron-doping will likely need to be accounted for in future theoretical efforts to model AF order's response to symmetry breaking strain fields in Co-doped Ba-122.

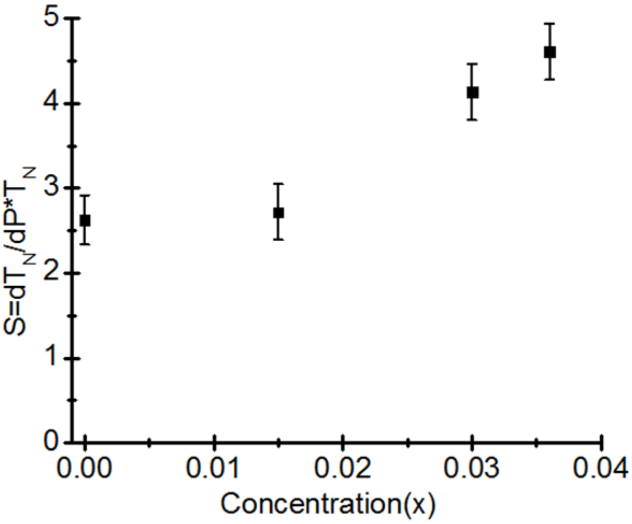

Figure 7.8.1 Shift of T_N as a fraction of T_N and applied pressure**.**

Generally, in the presence of strain, C_4 symmetry is broken, and we don't expect a sharp structural transition in our measurements. For the scenario in which orbital ordering drives the underlying lattice instability, the onset of the C_4 symmetry breaking structural orthorhombicity due to the applied strain field lifts the degeneracy of the d_{xz} and d_{yz} orbitals and rounds off the orbital ordering transition. This enables a small but non-zero orbital imbalance at higher temperatures over the regime where the orthorhombic structure distortion is observed. This orbital configuration potentially promotes AF SDW order and increases the transition temperature T_N below which the required time reversal symmetry breaking takes place.

Our data suggest a reduction in the AF ordered moment of parent $BaFe_2As_2$ under uniaxial pressure which is consistent with recent predictions from ab initio density functional theory (DFT) [36]. Pressure induced changes in pnictogen height are predicted to modify the resulting ordered moment as in-plane stress is applied; however we note here that the effect we observe occurs at significantly lower pressures than those modeled in Ref [36]. It is difficult to completely preclude the effect of remanant twin domains changing the apparent moment value, but to provide an estimate, we can simply assume that the structural peaks serve as a reliable indicator for when the sample has been completely detwinned. Using this assumption, the ordered moment has been reduced by 12% relative to its stress free value under the application of ≈2 MPa. Upon doping a slight amount of Co-impurities however, this effect seems to diminish and the 1% Co-doped sample shows complete detwinning without an effective AF moment change under similar level of pressure.

The decoupling of T_S and T_N under uniaxial pressure suggests that the magnetic order parameter shifts upward in temperature as a secondary effect driven by the pressure enhanced orthorhombicity of the lattice. This decoupling occurs for both Co-concentrations measured below the magnetostructural tricritical point in the electronic phase diagram (x=0, x=0.015), and more generally the separation between T_N and T_S appears to depend on the magnitude of applied uniaxial pressure. From phenomenological models, the differing response of both T_S and T_N to strain can readily be explained via the magnetoelastic coupling constant which necessarily dampens the shift of AF order relative to the shifted temperature at which significant orthorhombic distortion sets in. Another possible explanation may arise from a varying response of spin-lattice and orbital-lattice coupling strengths which respectively tune the relative response of AF and structural order parameter to the applied pressure.

Chapter 7 References

[1] Y. Kamihara, T. Watanabe, M. Hirano, and H. Hosono, J. Am. Chem. Soc. **130**, 3296 (2008).

[2] A. Kordyuk, Low Temp. Phys. **38**, 888 (2012).

[3] G. Stewart, Reviews of Modern Physics **83**, 1589 (2011).

[4] C. de La Cruz, Q. Huang, J. Lynn, J. Li, W. Ratcliff II, J. L. Zarestky, H. Mook, G. Chen, J. Luo, and N. Wang, Nature **453**, 899 (2008).

[5] S. D. Wilson, Z. Yamani, C. Rotundu, B. Freelon, E. Bourret-Courchesne, and R. Birgeneau, Physical review.B, Condensed matter and materials physics **79**, 184519 (2009).

[6] I. R. Fisher, L. Degiorgi, and Z. Shen, Reports on Progress in Physics **74**, 124506 (2011).

[7] P. Hirschfeld, M. Korshunov, and I. Mazin, Reports on Progress in Physics **74**, 124508 (2011).

[8] P. Dai, J. Hu, and E. Dagotto, Nature Physics **8**, 709 (2012).

[9] J. Paglione and R. L. Greene, Nature Physics **6**, 645 (2010).

[10] H. Wen and S. Li, Annu.Rev.Condens.Matter Phys. **2**, 121 (2011).

[11] M. Kim, R. Fernandes, A. Kreyssig, J. Kim, A. Thaler, S. Bud'ko, P. Canfield, R. McQueeney, J. Schmalian, and A. Goldman, Physical Review B **83**, 134522 (2011).

[12] J. Teng, C. Chen, Y. Xiong, J. Zhang, R. Jin, and E. Plummer, Proceedings of the National Academy of Sciences **110**, 898 (2013).

[13] S. Nandi, M. Kim, A. Kreyssig, R. Fernandes, D. Pratt, A. Thaler, N. Ni, S. Bud'Ko, P. Canfield, and J. Schmalian, Phys. Rev. Lett. **104**, 057006 (2010).

[14] W. Lee and C. Wu, Phys. Rev. Lett. **103** (2009).

[15] M. D. Lumsden and A. D. Christianson, Journal of Physics: Condensed Matter **22**, 203203 (2010).

[16] J. T. Park, D. S. Inosov, A. Yaresko*, et al*, Physical Review B **82** (2010).

[17] R. M. Fernandes, A. V. Chubukov, J. Knolle, I. Eremin, and J. Schmalian, Physical Review B **85** (2012).

[18] S. Kasahara, H. J. Shi, K. Hashimoto*, et al*, Nature **486**, 382 (2012).

[19] E. C. Blomberg, A. Kreyssig, M. A. Tanatar*, et al*, Physical Review B **85** (2012).

[20] J. Chu, J. G. Analytis, K. De Greve, P. L. McMahon, Z. Islam, Y. Yamamoto, and I. R. Fisher, Science **329**, 824 (2010).

[21] A. Dusza, A. Lucarelli, A. Sanna, S. Massidda, J. Chu, I. R. Fisher, and L. Degiorgi, New Journal of Physics **14** (2012).

[22] M. Allan, T. Chuang, F. Massee, Y. Xie, N. Ni, S. Bud'ko, G. Boebinger, Q. Wang, D. Dessau, and P. Canfield, Nature Physics **9**, 220 (2013).

[23] M. Yi, D. Lu, J. Chu, J. G. Analytis, A. P. Sorini, A. F. Kemper, B. Moritz, S. Mo, R. G. Moore, and M. Hashimoto, Proceedings of the National Academy of Sciences **108**, 6878 (2011).

[24] L. W. Harriger, H. Q. Luo, M. S. Liu, C. Frost, J. P. Hu, M. R. Norman, and P. Dai, Physical Review B **84** (2011).

[25] E. C. Blomberg, M. A. Tanatar, A. Kreyssig, N. Ni, A. Thaler, R. Hu, S. L. Bud'ko, P. C. Canfield, A. I. Goldman, and R. Prozorov, Physical Review B **83** (2011).

[26] S. Liang, A. Moreo, and E. Dagotto, arXiv preprint arXiv:1305.1879 (2013).

[27] M. Nakajima, S. Ishida, Y. Tomioka, K. Kihou, C. Lee, A. Iyo, T. Ito, T. Kakeshita, H. Eisaki, and S. Uchida, Phys. Rev. Lett. **109**, 217003 (2012).

[28] S. Ishida, M. Nakajima, T. Liang, K. Kihou, C. Lee, A. Iyo, H. Eisaki, T. Kakeshita, Y. Tomioka, and T. Ito, J. Am. Chem. Soc. **135**, 3158 (2013).

[29] H. -. Kuo, J. G. Analytis, J. -. Chu, R. M. Fernandes, J. Schmalian, and I. R. Fisher, Physical Review B **86** (2012).

[30] C. Dhital, Z. Yamani, W. Tian, J. Zeretsky, A. S. Sefat, Z. Wang, R. J. Birgeneau, and S. D. Wilson, Phys. Rev. Lett. **108** (2012).

[31] Y. Song, S. V. Carr, X. Lu, C. Zhang, Z. C. Sims, N. Luttrell, S. Chi, Y. Zhao, J. W. Lynn, and P. Dai, Physical Review B **87**, 184511 (2013).

[32] A. S. Sefat, R. Jin, M. A. McGuire, B. C. Sales, D. J. Singh, and D. Mandrus, Phys. Rev. Lett. **101**, 117004 (2008).

[33] R. Birgeneau, J. Skalyo, and G. Shirane, J. Appl. Phys. **41**, 1303 (1970).

[34] A. Cano and I. Paul, Physical Review B **85**, 155133 (2012).

[35] J. Hu, C. Setty, and S. Kivelson, Physical Review B **85** (2012).

[36] M. Tomic, H. O. Jeschke, R. M. Fernandes, and R. Valentí, Physical Review B **87**, 174503 (2013).

Chapter 8: Conclusion and Future Works

The results presented in chapter 4 to 6 helped to increase the present understanding regarding the electronic/magnetic behavior of the single layer and bilayer compounds of the Ruddelsden-Popper series oxides. Chapter 4 presents the result of the neutron scattering study on the single layer compound Sr_2IrO_4. This study reveals an antiferromagnetic spin structure lying in the ab plane and oriented along a unique axis with the ordered moment of 0.36 μ_B/Ir. This moment is comparable to that of bilayer compound $Sr_3Ir_2O_7$. Our results also reveal the presence of previously unreported structural superlattice peaks suggesting a discrepancy with the previously reported crystal structures.

In chapter 5, I presented a detailed study of bilayer parent compound $Sr_3Ir_2O_7$ using magnetotransport, magnetization and neutron scattering studies. My studies of this bilayer iridate reveal an electronically textured, G-type antiferromagnetic (m // c) ground state with non-Ohmic behavior at temperature below 70 K with ordered moment of 0.35 μ_B/Ir. Neutron diffraction measurements also indicate the presence of previously unreported structural superlattice peaks persisting at least up to 620 K.

In chapter 6, the results of our comprehensive study on the doped system $Sr_3(Ir_{1-x}Ru_x)_2O_7$ using magnetotransport, magnetization, scanning tunneling microscopy, and neutron scattering are presented. Here, we are able to map out the complete electronic/magnetic phase diagram with identification of multiple phases coexisting together. Our study gives a detailed picture of how the electronic/magnetic behavior of this system evolves as the system is doped progressively from AF insulator ($Sr_3Ir_2O_7$) to a Fermi liquid metal ($Sr_3Ru_2O_7$). Given the doubt about the importance of electronic correlations in this bilayer parent material, our results argue for the substantial role of electronic correlations in this otherwise weakly correlated insulating compound.

Our neutron scattering studies exploring the effect of uniaxial pressure on the structural and magnetic phase behaviors of parent and underdoped high temperature superconducting system Ba $(Fe_{1-x}Co_x)_2As_2$ were discussed in Chapter 7. We found a dramatic, upward thermal shift in both T_S and T_N upon the application of the uniaxial pressure. Curiously, the upward shift of T_N remains almost independent of doping for the same level of uniaxial pressure.

In this work, we found two problems regarding the discrepancy in the reported iridate crystal structures but we do not have the solutions yet. The future work should be focused on the detailed single crystal structural analysis of both the single layer and bilayer compound. In our doping studies, various factors may come into play at the same time e.g change in disorder, change in spin-orbit interactions, change in carrier density etc. A systematic study can be done by varying only one parameter keeping others fixed which may be done by doping other candidates cation elements e.g Rh, Os, Pt etc.

In iron based superconductors, similar pressure studies can be done either with other dopants on the same site (Fe site) or to the different site (As or Ba site). Furthermore, there is some debate about the nature of this effect whether that is intrinsic or extrinsic. This can be done by doing thorough annealing studies. Although, the definition of T_S becomes unclear in presence of symmetry breaking uniaxial pressure, inelastic scattering measurements can also be performed to look for the phonon softening in presence of uniaxial pressure. With alignment of many pressurized crystals together, similar studies can also be performed exploring the low energy spin dynamics of this system in the presence of uniaxial pressure.

Appendix

A.Some Facts about Magnetic Neutron Scattering

Neutron scattering is an ideal method for magnetic structure and ordered moment determination. The prediction of moment direction and the ordered moment depends upon following key facts about the magnetic neutron scattering.

(1) Neutrons can only measure the component of ordered moment that is perpendicular to the scattering vector **Q**. If the moments are pointing along the scattering vector then the intensity of magnetic scattering is zero.

(2) The magnetic scattering generally decreases with increasing Q due to decrease in the magnetic form factor. Depending upon the lattice parameters of the crystal, a right instrument has to be chosen so that one cannot miss the magnetic scattering present at low Q. The magnetic scattering also decreases with increasing temperature (in general). But the most definitive way to distinguish magnetic and nuclear scattering is by doing polarized neutron experiment.

(3) The identification of magnetic propagation vector **K** which defines the relative orientation of the moments in the lattice. For two sites m and n, the spin in site n is related to that in site m by a relation $S_n = S_m \exp(i\mathbf{K}.\mathbf{R})$, where R is the vector connecting two sites.

(4) The size of magnetic unit cell which can be same as the crystallographic unit cell or different from crystallographic unit cell. For example in case of ferromagnetic structure with magnetic wave vector **K** = (0, 0, 0) the magnetic and crystallographic unit cell will be same. For antiferromagnetic structure with magnetic wave vector (0.5, 0, 0), the magnetic unit cell will be doubled

along *a* axis whereas it is same as crystallographic unit cell along b and c axis. Similarly for antiferromagnetic spin arrangement with (0.5, 0.5, 0), the magnetic unit cell is doubled along *a* and *b* axis but remains same along c axis. But in this case, the common practice is to use the orthorhombic unit cell $\sqrt{2}a \times \sqrt{2}b$ as the magnetic unit cell where the volume of magnetic unit cell is two times ($\sqrt{2} \times \sqrt{2}$) the crystallographic unit cell. This is the case in our moment calculation for $Sr_3Ir_2O_7$ where we assumed orthorhombic unit cell as the magnetic unit cell. For Sr_2IrO_4, the crystal structure I41/acd is already a distorted tetragonal structure thus we assumed this unit cell as the magnetic unit cell.

(5) The occupancy of each magnetic atom in the unit cell e.g for a cubic or tetragonal or orthorhombic system, if the magnetic atom is fully inside the unit cell then the occupancy is 1. If it is at the center of face then occupancy is 2. If it is at the center of edge then occupancy is 4 and if it is at the corner then occupancy is 8.

(6) The fractional coordinates of all the magnetic atoms in the unit cell which can be obtained by visualization of the magnetic structure using crystal structure analysis software. The crystal and magnetic structure analysis software can also be used.

(7) In neutron scattering experiment, the observed intensity is the final result after considering several different instrumental (collimation, masking, detector efficiency, filtering, background, incident flux etc.) and sample parameters (absorption, extinction, mosaic, volume/mass of sample, temperature etc). Thus, rather than defining the absolute intensity, only relative intensity is a meaningful quantity. In nuclear scattering, the expected intensity for a certain

Q position can be calculated using different structural analysis software like Fullprof or GSAS. Thus, in practice, the nuclear scattering intensity is measured at different Q positions and comparing them with the expected intensity a scale factor is defined. This scale factor is in turn used for scaling magnetic intensity.

B. Calculation of the Scale Factor (S):

(In this section the temperature factor and the absorption effects are not taken into account)

For single crystal diffraction using the triple axis spectrometer, the scale factor (S) is defined by the relation [1]

$$\left|F_N^{obs}(Q)\right|^2 = \frac{S\left|F_N(Q)\right|^2}{1+B\left|F_N(Q)\right|^2} \tag{B1}$$

Where B is the extinction factor. $\left|F_N^{obs}(Q)\right|^2 = I_N(Q)\sin(2\theta)$. $I_N(Q)$ is the integrated intensity (integrated over Q) of nuclear peak at position Q and θ is the Bragg angle for that nuclear peak. $\left|F_N(Q)\right|^2$ is the expected square of structure factor for the corresponding nuclear peak . The structure factor F_N can be calculated using the relation

$$F_N(Q) = \sum_j O_j b_j \exp(i\mathbf{Q}.\mathbf{d}_j) \tag{B2}$$

Where sum is over all j atoms in the crystallographic unit cell, b_j is the coherent nuclear scattering length for atom j which can be found in different data bases and O_j is the fractional occupancy of j^{th} atom in the unit cell. **Q** = [2πH/a, 2πK/b, 2πL/c], which a, b, c as the lattice parameters, H, K, L refer to the position of the peak in reciprocal lattice unit. $\mathbf{d_j}$=[ax_j, by_j,cz_j] is the vector connecting the j^{th} atom to the origin of the unit cell and x_j,y_j, z_j are the fractional coordinates of the j^{th} atom. During an experiment a radial scan is performed across multiple nuclear peaks and hence the integrated intensity $I_N(Q)$ is obtained. The scale factor S can be obtained by fitting equation (B1). If there are not enough nuclear peaks to fit Equation (B1) then the best way is to do the radial scan across a single nuclear peak that is very close to magnetic peak in Q. In this case the scale factor S can be approximately defined using B=0 in Equation (B1). This approximation works best if the extinction effect is small which was in fact the case throughout the work described in this thesis.

C. Calculation of Magnetic Structure Factor and Ordered Moment

Now for the magnetic scattering, the magnetic structure factor is given by

$$F_{mag}(\mathbf{Q}) = 2.695\times10^{-15}\sum_j o_j \mu_j f_j(Q)(\boldsymbol{\mu}_\mathbf{j}\times\mathbf{Q}\times\boldsymbol{\mu}_\mathbf{j})\exp(\mathbf{Q}\bullet \qquad \text{(C1)}$$

Where o_j is the fractional occupancy of magnetic atom in the unit cell, μ_j is the ordered moment of j^th^ atom, $\boldsymbol{\mu}_\mathrm{j}$ is the unit vector along $\boldsymbol{\mu}_\mathrm{j}$, $\mathbf{Q}$ is the unit vector along **Q,** $f_j(Q)$ is the magnetic form factor for j^th^ atom. The sum is taken over all the magnetic atoms in the unit cell. Now the integrated area of the observed magnetic peak is given by

$$I_{mag}(\mathbf{Q}) = S\frac{|F_{mag}(Q)|^2}{\sin(2\theta)} \qquad \text{(C2)}$$

Using equations B1, B2, C1 and C2, the ordered magnetic moment μ_j of j^th^ atom can be calculated. In our study for $Sr_3Ir_2O_7$ and Sr_2IrO_4 there is only one kind of magnetic atom Iridium (Ir^{4+}) whereas the magnetic atom in $BaFe_2As_2$ is iron (Fe^{2+}).The form factor for iridium was obtained by using Jo and J_2 as described in paper by Koyabashi et al [2] and for the iron the form factor was obtained by using coefficients given in ref [3]. As an illustration here is a list of all the magnetic atoms in magnetic unit cell (orthorhombic structure) along with their fractional occupancies in $Sr_3Ir_2O_7$. a ≈ b ≈ 5.5Å,c≈20.89Å.

Fractional coordinates of Ir atom in magnetic unit cell

Ir_1 =[0, 0, .09743];

Ir_2 =[0, 0, (1-.09743)];

Ir_3 =[1, 0, .09743];

Ir_4 =[1, 0, (1-.09743)];

Ir_5 =[0, 1, .09743];

Ir_6 =[0, 1, (1-.09743)];

Ir_7 =[1, 1, .09743];

Ir_8 =[1, 1, (1-.09743)];

Ir_9 =[0.5, 0.5, .09743];

Ir_{10} =[0.5, 0.5, (1-.09743)];

Ir_{11} =[0.5, 0.0, (0.5+.09743)];

Ir_{12} =[0.5, 0.0, (0.5-.09743)];

Ir_{13} =[1, 0.5, (0.5+.09743)];

Ir_{14} =[1, 0.5, (0.5-.09743)];

Ir_{15} =[0.5, 1, (0.5+.09743)];

Ir_{16} =[0.5, 1, (0.5-.09743)];

Ir_{17} =[0.0, 0.5, (0.5+.09743)];

Ir_{18} =[0.0, 0.5, (0.5-.09743)];

Unit vector along direction of moment (moment along c is +1 and moment along –c is -1)

m_1=[0 0 1];

m_2=[0 0 -1];

m_3=[0 0 1];

m_4=[0 0 -1];

m_5=[0 0 1];

m_6=[0 0 -1];

m_7=[0 0 1];

m_8=[0 0 -1];

m_9=[0 0 -1];

m_{10}=[0 0 1];

m_{11}=[0 0 -1];

m_{12}=[0 0 1];

m_{13}=[0 0 1];

m_{14}=[0 0 -1];

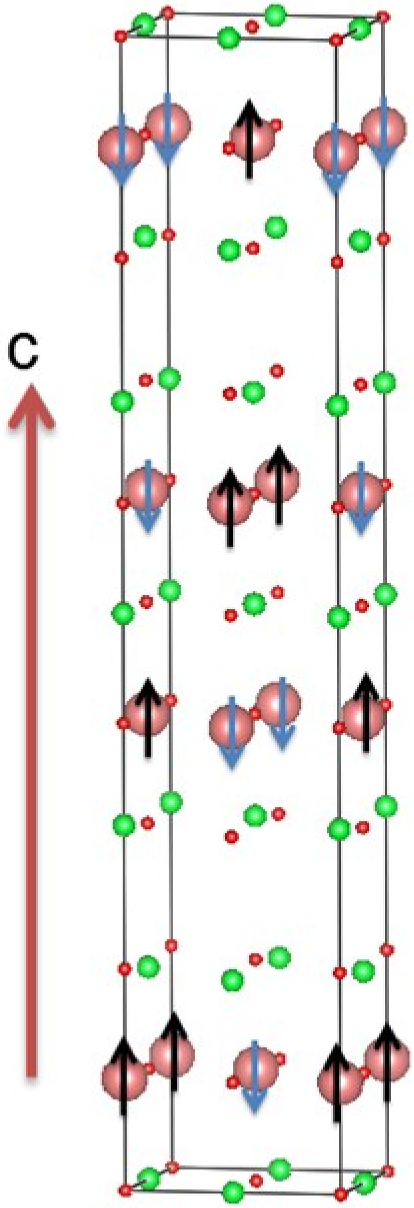

Magnetic unit cell for $Sr_3Ir_2O_7$

m_{15}=[0 0 -1];

m_{16}=[0 0 1];

m_{17}=[0 0 1];

m_{18}=[0 0 -1];

Fractional occupancies

O_1=0.25;

O_2=0.25;

O_3=0.25;

O_4=0.25;

O_5=0.25;

O_6=0.25;

O_7=0.25;

O_8=0.25;

O_9=1;

O_{10}=1;

O_{11}=0.5;

O_{12}=0.5;

O_{13}=0.5;

O_{14}=0.5;

O_{15}=0.5;

O_{16}=0.5;

O_{17}=0.5;

O_{18}=0.5;

Appendix References

[1] Z. Yamani, Z. Tun, and D. Ryan, Can. J. Phys. **88**, 771 (2010).

[2] K. Kobayashi, T. Nagao, and M. Ito, Acta Crystallographica Section A: Foundations of Crystallography **67**, 473 (2011).

[3] https://www.ill.eu/sites/ccsl/ffacts/ffachtml.html

Publications List

[1] **C. Dhital**, D. L. Abernathy, G. Zhu, Z. Ren, D. Broido, and S. D. Wilson, Physical Review B **86**, 214303 (2012).

[2] **C. Dhital**, C. de La Cruz, C. Opeil, A. Treat, K. Wang, J. Liu, Z. Ren, and S. D. Wilson, Physical Review B **84**, 144401 (2011).

[3] **C. Dhital**, T. Hogan, Z. Yamani, C. de la Cruz, X. Chen, S. Khadka, Z. Ren, and S. D. Wilson, Physical Review B **87**, 144405 (2013).

[4] **C. Dhital**, T. Hogan, W. Zhou, X. Chen, Z. Ren, M. Pokharel, Y. Okada, M. Heine, W. Tian, and Z. Yamani, Nature communications **5** (2014).

[5] **C. Dhital**, S. Khadka, Z. Yamani, C. de la Cruz, T. Hogan, S. Disseler, M. Pokharel, K. Lukas, W. Tian, and C. Opeil, Physical Review B **86**, 100401 (2012).

[6] **C. Dhital**, Z. Yamani, W. Tian, J. Zeretsky, A. Sefat, Z. Wang, R. Birgeneau, and S. D. Wilson, Phys. Rev. Lett. **108**, 087001 (2012).

[7] S. Disseler, **C. Dhital**, A. Amato, S. Giblin, C. de la Cruz, S. D. Wilson, and M. Graf, Physical Review B **86**, 014428 (2012).

[8] S. Disseler, **C. Dhital**, T. Hogan, A. Amato, S. Giblin, C. de la Cruz, A. Daoud-Aladine, S. D. Wilson, and M. Graf, Physical Review B **85**, 174441 (2012).

[9] S. Disseler, S. Giblin, **C. Dhital**, K. Lukas, S. D. Wilson, and M. Graf, Physical Review B **87**, 060403 (2013).

[10] Y. Okada, **C. Dhital**, W. Zhou, E. D. Huemiller, H. Lin, S. Basak, A. Bansil, Y. Huang, H. Ding, and Z. Wang, Phys. Rev. Lett. **106**, 206805 (2011).

[11] Y. Okada, D. Walkup, H. Lin, **C. Dhital**, T. Chang, S. Khadka, W. Zhou, H. Jeng, M. Paranjape, and A. Bansil, Nature materials **12**, 707 (2013).

[12] Y. Okada, W. Zhou, **C. Dhital**, D. Walkup, Y. Ran, Z. Wang, S. D. Wilson, and V. Madhavan, Phys. Rev. Lett. **109**, 166407 (2012).

[13] Y. Okada, W. Zhou, D. Walkup, **C. Dhital**, S. D. Wilson, and V. Madhavan, Nature communications **3**, 1158 (2012).

[14] Y. Okada, M. Serbyn, H. Lin, *et al*, Science **341**, 1496 (2013).

[15] S. D. Wilson, Z. Yamani, **C. Dhital**, B. Freelon, P. Freeman, J. Fernandez-Baca, K. Yamada, S. Wakimoto, W. Buyers, and R. Birgeneau, Physical Review B **85**, 014507 (2012).

[16] D. DeMeo, C. Shemelya, C. Downs, A. Licht, E. S. Magden, T. Rotter, **C. Dhital**, S. Wilson, G. Balakrishnan, and T. E. Vandervelde, J Electron Mater, 1 (2014).

VITA

Chetan Was born in Bahundangi Nepal in September 1978. After passing SLC (School leaving certificate) from Bhanu secondary school in his hometown, he joined Tribhuvan university where he earned his intermediate and Bachelor in physical sciences and finally Master in physics in 2005. He then taught physics to undergraduate students in Damak Multiple Campus Jhapa for 3 years. He joined Boston college in 2008 and received his PhD in Physics in May 2014.